

## ODS steels for nuclear applications: thermal stability of the microstructure and evolution of defects

Marques Pereira, V.

**DOI**

[10.4233/uuid:3eab33fd-f9fc-420f-b574-749d22db5f1c](https://doi.org/10.4233/uuid:3eab33fd-f9fc-420f-b574-749d22db5f1c)

**Publication date**

2022

**Document Version**

Final published version

**Citation (APA)**

Marques Pereira, V. (2022). *ODS steels for nuclear applications: thermal stability of the microstructure and evolution of defects*. [Dissertation (TU Delft), Delft University of Technology].  
<https://doi.org/10.4233/uuid:3eab33fd-f9fc-420f-b574-749d22db5f1c>

**Important note**

To cite this publication, please use the final published version (if applicable).  
Please check the document version above.

**Copyright**

Other than for strictly personal use, it is not permitted to download, forward or distribute the text or part of it, without the consent of the author(s) and/or copyright holder(s), unless the work is under an open content license such as Creative Commons.

**Takedown policy**

Please contact us and provide details if you believe this document breaches copyrights.  
We will remove access to the work immediately and investigate your claim.

# **ODS steels for nuclear applications: thermal stability of the microstructure and evolution of defects**

Viviam Marques Pereira

# **ODS steels for nuclear applications: thermal stability of the microstructure and evolution of defects**

## **Dissertation**

for the purpose of obtaining the degree of doctor  
at Delft University of Technology  
by the authority of the Rector Magnificus, prof.dr.ir. T.H.J.J. van der Hagen,  
chair of the Board of Doctorates,  
to be defended publicly on  
Friday 6 May 2022 at 10:00 o'clock  
by

Viviam MARQUES PEREIRA  
Mestra em Ciências, Universidade de São Paulo, Brazil  
Born in São Paulo, Brazil

This dissertation has been approved by the promotor.

Composition of the doctoral committee:

Rector Magnificus,	chairperson
Prof. dr. ir. J. Sietsma	Delft University of Technology, <i>promotor</i>
Dr. H. Schut	Delft University of Technology, <i>copromotor</i>

Independent members:

Prof.dr. C. Pappas	Delft University of Technology
Dr. M. F. Barthe	Centre National de la Recherche Scientifique (CNRS) , France
Prof. dr. M. R. de Baar	Eindhoven University of Technology
Ir. T.O.S. van Staveren	NRG, The Netherlands
Prof. dr. ir. R.H. Petrov	Ghent University, Belgium
Prof. dr. ir. L.A.I. Kestens	Delft University of Technology, reserve member



REACTOR  
INSTITUTE  
DELFT



**DIFFER**  
Dutch Institute for  
Fundamental Energy Research

This research was carried out under project number T16010e in the framework of the Partnership Program of the Materials Innovation Institute M2i ([www.m2i.nl](http://www.m2i.nl)) and the Netherlands Organization for Scientific Research NWO ([www.nwo.nl](http://www.nwo.nl)).

*Keywords:* ODS steels, microstructural characterization, phase transformations, positron annihilation Doppler Broadening, microscopy

*Artwork of cover and back by:* Beatriz Ramos

*Printed by:* Proefschriftmaken ([www.proefschriftmaken.nl](http://www.proefschriftmaken.nl))

Copyright © 2022 by Viviam MARQUES PEREIRA

ISBN: 978-94-6384-332-4

An electronic copy of this dissertation is available at TU Delft repository.

Ao meu avô Nicola Serra,  
Aos meus pais Isabel e Xerxes

# Table of Contents

1.	Introduction.....	3
1.1.	Advantages, challenges and current status of nuclear power .....	3
1.2.	Nuclear fission vs nuclear fusion.....	7
1.3.	Advanced nuclear technologies and materials challenges.....	9
1.4.	Objectives and thesis outline .....	11
2.	Background.....	13
2.1.	Basics of radiation damage in metallic materials .....	13
2.2.	Oxide Dispersion Strengthened steels .....	16
3.	Microstructural stability of the 0.3% Y <sub>2</sub> O <sub>3</sub> ODS Eurofer steel .....	20
	Abstract.....	20
3.1.	Introduction.....	21
3.2.	Experimental.....	23
3.3.	Results.....	26
3.4.	Discussion.....	36
3.5.	Conclusions.....	37
4.	Characterization of oxide nanoparticles present in the ODS Eurofer steel .....	39
	Abstract.....	39
4.1.	Introduction.....	40
4.2.	Experimental.....	41
4.3.	Results.....	43
4.4.	Discussion.....	54
4.5.	Conclusions .....	56
5.	Thermal stability of the microstructure and characterization of oxide nanoparticles in the ODS 12 Cr steel.....	58
	Abstract.....	58
5.1.	Introduction.....	59
5.2.	Experimental.....	60
5.3.	Results and Discussion .....	62
5.4.	Conclusions.....	76
6.	Thermal evolution of defects in ODS steels studied with Positron Annihilation Doppler Broadening.....	78
	Abstract.....	78
6.1.	Introduction.....	79
6.2.	Experimental.....	84
6.3.	Results.....	87
6.4.	Discussion.....	96

6.5. Conclusions.....	101
7. Deuterium behaviour in the ferritic ODS 12 Cr steel .....	103
Abstract.....	103
7.1. Introduction.....	104
7.2. Experimental.....	105
7.3. Analysis and Modelling of Thermal Desorption Spectroscopy Data .....	106
7.4. Results and Discussion .....	108
7.5. Conclusions .....	117
8. General conclusions and recommendations.....	118
8.1. General conclusions .....	118
8.2. Recommendations for future research .....	120
References.....	122
Summary.....	137
Samenvatting.....	139
Acknowledgements.....	141
Curriculum Vitae .....	144
List of Publications .....	145

## **1. Introduction**

In view of the current climate and energy crisis, the transition to a carbon-free, efficient, energy matrix is urgent. The global demand for energy does not stop to increase, even during the Covid-19 pandemic: in the year of 2020 the most dramatic decrease of energy consumption since World War II was observed, but projections for 2021 suggest that the global energy use will be 0.5% higher than in 2019, as Covid-related restrictions are partly lifted [1]. Changing the carbon-based energy matrix is not an easy and short-term task: sectors like transportation and manufacturing, the two sectors with highest consumption of end-use energy and highest CO<sub>2</sub> emissions [2], are still strongly dependent on fossil-fuels [3] and, to change this dependence, the complete re-structuration of these sectors is needed, accompanied by an increase in efficiency of cleaner energy matrices [2]. On a positive side, the space for renewable resources (mainly wind and solar) is increasing, as it is expected that renewables will provide more than 50% of the world-wide electricity demand in 2021 [1]. However, renewable resources alone are not enough to meet the goals in reduction of greenhouse gas emissions established in the Paris agreement of 2015: their combined use with hydropower and, in particular, nuclear power is essential to stop the developing climate catastrophe [4].

### **1.1. Advantages, challenges and current status of nuclear power**

There are several requirements that low-carbon energy resources must meet in order to minimize impacts on the environment [5]. The energy resources have to 1) use minimum amounts of land and fresh water for production or mining; (2) minimize pollution (greenhouse gases emissions, production of heavy metals, toxic chemicals and other waste); (3) restrict habitat fragmentation, (4) present a low risk of accidents that could cause large impacts to the environment and humanity; (5) be cost-effective; (6) be reliable and (7) be accessible [5]. In Table 1.1. the advantages and challenges associated with nuclear power (fission and fusion) and renewable resources are listed.



**Table 1. 1.** Advantages and challenges of nuclear power and other renewable resources.

Resource	Advantages	Challenges
<b>Nuclear fission</b>	<p>Low emission of greenhouse gases [6];</p> <p>Does not produce toxic heavy metals, black carbon, sulphates, aerosols [5];</p> <p>Costs are more stable, in comparison with fossil fuels [7];</p> <p>Energy production does not depend on climate factors, like Sun incidence and wind velocity [5];</p> <p>It is able to supply global high energy demands (large scale energy generation) [7];</p> <p>Long lifespan (40 years, with possibility of extension to 60-80 years) [5];</p> <p>Requires the least land area displacement for energy production, in comparison to other resources [5].</p>	<p>Risk of nuclear weapons development and proliferation [5], [7];</p> <p>Accident could lead to large damage to the environment and humanity [5], [7];</p> <p>Production of radiotoxic waste [5], [7], [8];</p> <p>Causes anxiety among large part of the population.</p>
<b>Nuclear fusion [9]</b>	<p>Does not produce toxic heavy metals, black carbon, sulphates, aerosols;</p> <p>Low emission of greenhouse gases;</p> <p>Lower amount of radioactive waste than from nuclear fission;</p> <p>Delivery of large amount of energy from small amount of fuel.</p>	<p>Complexity of technology, which requires intense research efforts;</p> <p>Current stage of development is still far from possibility of commercialization.</p>
<b>Hydropower</b>	<p>Low greenhouse gases emissions [5], [6], [10], [11];</p> <p>Does not produce toxic by-products [10];</p> <p>Besides providing electricity, hydropower plants can aid in flood control, irrigation and be used as potable water reservoirs [10], [12];</p> <p>Cost-effective electricity source: high efficiency for electricity generation with low operation and maintenance costs, compensating relatively high investments for plant construction [10], [11].</p>	<p>Negative environmental impacts as a consequence of inundation of large areas [5], [12], [13]</p> <p>Decay of the flooded biomass, which results in the gradual emission of greenhouse gases [13];</p> <p>Geographical dependency on the distribution of waterways [5];</p> <p>Restriction of navigation and modifications of local land use [12].</p>

**Table 1. 2. (Continuation)** Advantages and challenges of nuclear power and other renewable resources.

Resource	Advantages	Challenges
<b>Wind (onshore and offshore)</b>	<p>Low greenhouse gases emissions (even lower than nuclear energy) [6];</p> <p>Strong support of society [5];</p> <p>Utilizes free primary energy and the technology involved is not overly complex [14];</p> <p>Generators can be located offshore or onshore [14];</p> <p>Cost competitive alternative for coal, also competes well with nuclear energy [5], [14].</p>	<p>Wind turbines use large amounts of concrete, steel and land use per unit of electricity delivered [5];</p> <p>Onshore plants depend on availability of wind (location and period of the year) [15];</p> <p>Large turbines are not easily accepted by local population.</p>
<b>Solar (photovoltaic)</b>	<p>Photovoltaic systems are highly modular and easy to install [16], [17];</p> <p>Photovoltaic installations can generate power even when the sky is not completely clear (use of diffuse component of sunlight) [17];</p> <p>Strong support of society [16].</p>	<p>Efficiency is low and costs are relatively high [16]–[18];</p> <p>Manufacture process of solar cells use toxic chemicals that do not degrade over time [5], [18];</p> <p>Relatively large land use [5], [16]–[18].</p>
<b>Biofuels (from dedicated biomass and from waste)</b>	<p>Wide variety of systems and technologies available for biofuels production [14];</p> <p>Dedicated biomass is considered a carbon-neutral resource, once the amount of CO<sub>2</sub> released during combustion of the biomass is equal to the amount captured by the plant during its cultivation [14], [19];</p> <p>Reduction of existing residues and waste (when the biofuel is produced from them) [14], [19];</p> <p>Decrease in methane emissions from landfills (anaerobic decomposition of biomass in landfills) [14], [19];</p> <p>Economic improvement of rural areas (creation of jobs and income) [19].</p>	<p>Dedicated biomass requires large land area displacement for energy production, thus, may lead to deforestation, loss of biodiversity and increase in CO<sub>2</sub> emissions (from land cleaning) [5], [14], [19];</p> <p>Currently, there is no global monitoring, neither sustainable criteria, for the responsible cultivation of dedicated biomass [19];</p> <p>Use of extra amounts of water, fertilizers and pesticides for dedicated biomass cultivation [19];</p> <p>When utilizing waste for biofuels production, the removal of the biowaste from land can reduce carbon storage, carbon pools (soil, dead wood, litter) and decrease the soil nutrients content [14].</p>

Table 1.1. shows that there is no type of energy resource exempt of challenges or disadvantages, hence, an interesting strategy to improve efficiency, minimize environmental impact and meet the high global energy demand is to combine the use of different resources, considering their availability, effect on local environment and socioeconomic impact [5]. Among the low-carbon energy resources, nuclear fission has a strong potential to aid in the climate and energy crisis. In nuclear power plants, energy can be produced at any time of the year, without any dependence on environmental conditions. If nuclear reactors had never been developed and deployed, CO<sub>2</sub> emissions from electricity generation would have been 20%

higher during the past 50 years [4]. However, its use is in risk of decline due to two main factors: (1) retirement of reactors that are reaching their end of service life and (2) policies to reduce the nuclear fleet in some European countries, due to unpopularity of nuclear energy [4]. Despite its several advantages, the fear of nuclear accidents, weapon proliferation and radioactive waste disposal are disadvantages of great concern, which prejudice the reputation of nuclear power among the community in general [7]. To overcome these issues, improvements in fission reactor design, safety governance, nuclear waste treatment and disposal are being made – many of these led by the Chernobyl and Fukushima accidents [20].

The fission reactors commercially in use today are of Generation II, built in the 1960's and 1970's, and part of them are going through lifetime extension, from 30 or 40 years to 60 or 80 years [5], [21], [22], [23]. New Generation III and III+ fission reactors, with more advanced design, are starting to be deployed. Extensive research efforts are currently being made to develop the so-called Generation IV nuclear reactors [24], [25]. The Generation IV reactors are designed to present, in relation to the older generation ones, improved safety, reliability, sustainability, longer life times (minimum of 60 years), proliferation resistance and profitability [24]. There are six main Generation IV reactors systems in development: gas-cooled fast reactor (GFR), lead-cooled fast reactor (LFR), molten salt reactor (MSR), sodium-cooled fast reactor (SFR), very high temperature reactor (VHTR) and super-critical water-cooled reactor (SCWR) [24]. In addition, the use of thorium-based fuel cycles in Generation IV reactors has gained renewed interest. China is currently building an experimental molten salt reactor that will use thorium as fuel and the project is currently in the testing phase [25]. India also invests in the development of thorium reactors, due to its vast thorium reserves [26]. This regained interest in thorium-based reactors comes from its natural availability, which is three to four times greater than uranium's, increased resistance to the proliferation of weapons, production of lower levels of nuclear waste and suitability for use in several types of reactor designs, like light water reactors (LWR), heavy water reactors (HWR), MSR, high temperature gas cooled reactors (HTGR) and accelerator driven system reactors (ADSR) [26], [27].

Besides the developments in nuclear fission, intense research at a global level is being conducted to make nuclear fusion a concrete technology: currently, the European Union, USA, Russia, Japan, China, Brazil, Canada, Australia and Korea are part of fusion research programs [9]. In theory, nuclear fusion would be able to supply almost infinite amounts of clean energy, in a safer way than nuclear fission technologies, but the complexity in building fusion systems and the challenges towards meeting the materials requirements are far greater. Currently, experimental facilities are being built in order to verify the feasibility of nuclear fusion to

produce energy at large scale. The most well-known and largest experiment is ITER (International Thermonuclear Experimental Reactor), under construction in France. A next step after the successful construction of ITER and verification of feasibility of nuclear fusion would be the development of the first prototype of nuclear fusion reactor, DEMO (DEMONstration power plant). This project is a joint effort of Europe and Japan [9], [28].

## 1.2. Nuclear fission vs nuclear fusion

Essentially, nuclear fission consists of the splitting of a nucleus into smaller parts (lighter nuclei), accompanied by the release of neutrons and large amounts of energy. The energy released in nuclear fission reactions is about 10 million times larger than in chemical reactions (like coal burning) and the amount of fuel necessary is very small: for example, fission of 1 g of  $^{235}\text{U}$  can generate 78.4 GJ of power, for which  $2.5 \times 10^6$  g (~2.7 tons) of coal would be necessary [29].

Fission can occur either naturally or artificially, although the probability of spontaneous fission is very low because of the strong nuclear forces acting in the nuclei of atoms. Artificial fission is achieved by the bombardment of a heavy, fissile nucleus with neutrons. The most known fuel used in nuclear fission is  $^{235}\text{U}$ , which corresponds to only 0.7% of the natural uranium available on Earth; the other 99.3% is constituted of  $^{238}\text{U}$ .  $^{235}\text{U}$  is the most suitable option for thermal reactors, due to its large cross-section for fission by thermal neutrons [6]. The abundant  $^{238}\text{U}$  has a small thermal neutron cross-section, but can be used to breed  $^{239}\text{Pu}$ , which is fissile, or can be used as fuel in the so-called fast reactors, which operate with a spectrum of fast neutrons (energies higher than 5 MeV) [6], [29]. The main types of waste produced by nuclear fission systems are tailings (by-product of uranium mining), spent fuel, fission products and irradiated structural components [11].

In a nuclear fusion system, the opposite of fission occurs: light nuclei fuse together in order to form a heavier nucleus, accompanied by large amounts of energy and, depending on the reaction type, neutrons. Fusion reactions occur naturally in the core of the Sun, where temperatures are of the order of  $1.5 \times 10^7$  °C and gravitational forces are intense ( $g \sim 274 \text{ m}\cdot\text{s}^{-2}$ ). A common fusion reaction in the core of the Sun involves the conversion of 4 protons into a  $^4\text{He}$  atom [9]. On Earth, where the gravitational force is much weaker, the reproduction of this particular reaction is unfeasible, but alternative processes are possible, albeit still challenging. The alternatives involve using hydrogen (H) and its isotopes deuterium (D) and tritium (T) in the plasma state to produce  $^4\text{He}$  atoms and large amounts of energy. The “easiest”

possible plasma reaction is the one in which D and T are combined to form  ${}^4\text{He}$  and neutrons, with energies equal to 3.5 MeV and 14.1 MeV, respectively. For the rate of this reaction to be high enough, the core of the D-T plasma needs to be at temperatures of the order of  $10^8$  °C [9]. The extremely high-temperature plasma, which cannot be contained by any existent material, can be confined by the use of magnetic fields, produced by toroidal devices. There are two main types of toroidal devices in advanced stages of design: the tokamak and the stellarator (Figure 1.1.). The plasma particles, which are ionised (and thus electrically charged), are forced to follow a restricted, helical path around the magnetic field lines, which allow the plasma containment [9], [26].

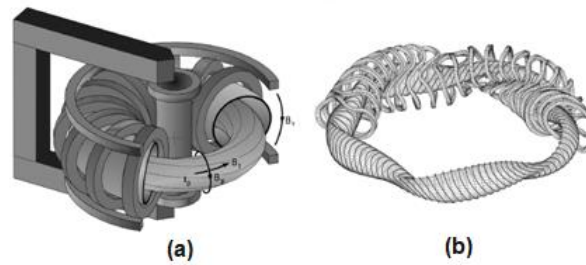


**Figure 1. 1.** Schematic representations of (a) a tokamak and (b) a stellarator. Extracted from [9].

Theoretically, nuclear fusion can deliver larger amounts of energy than fission and produces less radioactive waste, which would consist mainly of the structural materials of the reactor activated by the neutrons produced during the fusion reaction. Although D is largely available in nature, T, the radioactive isotope of hydrogen, is not. Breeding of T can be made in the blanket, with the use of lithium-containing solutions, according to the reaction:  $n + \text{Li} \rightarrow \text{He} + \text{T} + 2 \text{ MeV}$ . Examples of Li-containing solutions are: FLiBe and Pb-Li. There are several challenges related to fusion, starting with the integrity of structural materials, submitted to extreme operation conditions. The breeding of T is another challenging aspect in fusion. For the process to be self-sufficient, the blanket needs to cover 85% of the reactor wall, making the access for heating and diagnostics more difficult. It also imposes harsh conditions for the materials used in the blanket, since operation will take place in a corrosive environment, containing neutrons and hydrogen, and at high temperatures. In addition, it is possible to breed any type of element in the blanket and this consists of an under-looked risk for proliferation of weapons.

### 1.3. Advanced nuclear technologies and materials challenges

Among the six designs of Generation IV nuclear reactors, three will operate with fast neutrons (GFR, LFR, SFR) and other two have the potential to use either thermal or fast neutrons (MSR and SCWR). The core temperature for all designs will be considerably higher than in Generation II and III reactors (maximum temperature of around 600 K), ranging between 783 and 1273 K [31]. The types of coolants used will vary with reactor type: molten fluoride salts in MSR, liquid Na in SFR, liquid Pb in LFR, He gas in VHTR and GFR, and water in SCWR [31]. These modifications in design will bring a series of benefits for the safety and efficiency of nuclear reactors, but also impose harsher service conditions for the structural materials. The higher operation temperatures lead to increased thermal efficiency of the reactors and, for some designs, the possibility of production of hydrogen [31]. The utilization of fast-neutrons spectra allows the more efficient use of the uranium resources, employing the abundant  $^{238}\text{U}$  to breed  $^{239}\text{Pu}$ , which has a high fission cross-section for fast neutrons [32]. Fast-neutron reactors can also use  $^{235}\text{U}$  as fuel or burn the long-lived actinides recovered from fuel used in conventional reactors [32]. In this way, the production of nuclear waste can be significantly decreased [31], [32].

Structural materials to be used in Generation IV reactors will have to present, besides excellent mechanical properties, high corrosion resistance and compatibility to the different types of coolants, high thermal stability, which guarantee that mechanical properties will be maintained at the elevated operation temperatures, resistance to radiation damage under high neutron doses and resistance to He embrittlement [24]. Figure 1.2 schematizes the operating temperatures and levels of displacement damage that Generation IV and fusion systems will have to withstand, in comparison to Generation II systems [33]. Candidate materials for the various reactor components are ferritic-martensitic steels, austenitic stainless steels, oxide dispersion strengthened (ODS) steels, Ni-based alloys, graphite, refractory alloys and ceramics. Intense efforts are currently ongoing in order to qualify these materials for the nuclear applications [24].

In principle, nuclear fusion has even more attractive qualities than fission: (1) the fuel stays available only for a few seconds, while in fission it is stored in the reactor core for longer periods of time; (2) instead of neutrons multiplication and chain reactions, which pose a risk of going out of control, fusion reactions depends on high temperatures to occur, so, with any malfunction or incorrect handling the reactions will stop; (3) the fusion reactivity has an optimum with temperature and, therefore, run-away reactions are physically impossible and

(4) if any operation problem takes place and the plasma is shutdown, the energy remaining in the reactor will be too low to cause melting or damage of the core structure and (5) despite the risks associated to the breeding capabilities of the blanket, fusion systems can be considered to have improved resistance to proliferation, since only substantial alterations in the reactor's operations would allow its misuse and would be easily discovered [9]. Enormous scientific efforts have been made towards fusion in the past decades and they are leading to promising results, although the technology is not commercially available yet. ITER, the largest fusion experiment, is currently able to study various blanket concepts and to provide over 100 diagnostic systems.

The challenges imposed on structural materials by nuclear fusion systems are also many and, in some aspects, are greater than the ones associated to the Generation IV fission systems. In fusion systems, service temperatures will vary from 1273 K or higher (plasma-facing components) to cryogenic (superconducting magnets) [34]. The neutrons originated from D-T fusion reactions are highly energetic (14.1 MeV), leading to higher neutron doses and, thus, higher damage, than in most Generation IV systems (Figure 1.2) [33]. In-vessel components will also need to resist to high concentrations of He, H, D and T [9], [34], [33]. Blanket material candidates, as discussed earlier, need also to resist to corrosive environment.

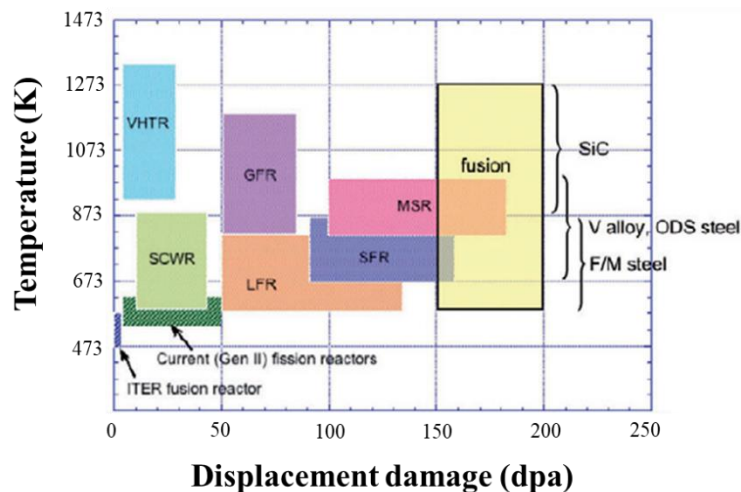


**Figure 1. 2.** Operation temperatures and displacement damage of structural materials used in different nuclear technologies: current Generation II fission reactors, the six designs of Generation IV fission reactors, ITER and the expected for commercial fusion systems. It is also shown in the picture the some classes of materials that can withstand the temperature ranges expected for commercial fusion reactors. Modified from [33].

So far, tungsten and tungsten alloys are the most promising candidates to be used in first wall, plasma-facing components. For other in-vessel constituents, suitable candidates are

ferritic/martensitic steels, vanadium alloys, ODS steels and SiC/SiC ceramic composites (which is however the least developed option) [34], [33].

Finally, an important requirement for both fission and fusion technologies is that their structural components exhibit reduced-activation. This means using alloying elements that, once activated, are able to lose radioactivity in hundreds of years or less, instead of thousands of years, as it is the case of the alloys deployed in conventional reactors. This requirement aids in minimizing nuclear waste and would allow the proper handling and recycling of the components at the end of lifetime of the future reactors. Examples of reduced-activation elements are: Fe, C, Cr, Ti, V, W, Si, Ta [9], [34], [33], [35].

#### **1.4. Objectives and thesis outline**

It is clear that a challenging aspect for the realisation of Generation IV and fusion technologies is to select and develop materials able to withstand the imposed extreme service conditions. Oxide Dispersion Strengthened (ODS) steels are potential candidates to be used as structural components in both Generation IV fission reactors and fusion reactors. ODS steels are high-Cr, reduced-activation steels, containing nanosized oxide particles dispersed in the matrix. This class of materials present attractive properties, like high tensile strength, excellent resistance to creep and fatigue, high thermal stability (up to temperatures of 1273 K), and increased resistance to radiation-induced defects. [35], [36]–[38].

In the present thesis, two ODS steels containing 0.3 weight % of  $Y_2O_3$  were studied: the 0.3%  $Y_2O_3$  ODS Eurofer and the ODS 12 Cr steel. The main objectives of the work developed in this project are:

- (1) Evaluate the thermal stability of the microstructure and of the oxide nanoparticles present in the steels;
- (2) Investigate the effect of oxide nanoparticles on the kinetics of phase transformations and other microstructural processes such as recovery, recrystallization;
- (3) Investigate the interaction of oxide nanoparticles with defects intrinsic to the microstructure;
- (4) Develop fundamental understanding of the thermal behaviour of the steels.



In Chapter 2, relevant background information for the understanding of the work is given, consisting of the basics of radiation damage in metallic alloys and general aspects of ODS steels.

The remaining Chapters are divided into two parts:

- Part I – Thermal stability of the microstructure and of oxide nanoparticles in ODS steels. Part I contains Chapters 3, 4 and 5;
- Part II – Analysis defects in ODS steels: thermal evolution and oxide nanoparticle interaction. Part II includes Chapters 6 and 7.

In Chapter 3, the microstructure of the 0.3%  $Y_2O_3$  ODS Eurofer steel is characterized and its thermal stability is evaluated. After annealing treatments at temperatures ranging from 600 K to 1600 K, the material was evaluated using Scanning Electron Microscopy (*SEM*), Electron Backscatter Diffraction (*EBS**D*) and Vickers hardness. The steel has a ferritic/martensitic matrix and first observations of the effect of oxide nanoparticles on the kinetics of phase transformations are made.

In Chapter 4, the 0.3%  $Y_2O_3$  ODS Eurofer steel in its reference condition and after annealing at 1400 K is analysed in more detail, using Transmission Electron Microscopy (*TEM*) and Atom Probe Tomography (*APT*). The oxide nanoparticles present in the material are characterized, their chemical composition and high-temperature behaviour are determined. The results discussed in Chapter 4 give further information on the role of oxide nanoparticles for the overall thermal stability of the steel and their effect on the microstructural processes occurring at high temperatures.

Chapter 5 presents the characterization of the microstructure, including the oxide nanoparticles, of the ODS 12 Cr steel, after annealing at temperatures between 573 K and 1573 K. The material was analysed with *SEM*, *EBS**D*, Vickers hardness and *TEM*. The ODS 12 Cr steel is ferritic and contains 0.3 weight % Ti. The addition of Ti has strong impact on the size and thermal stability of the oxide nanoparticles. The highly stable and fine oxide nanoparticles are responsible for maintaining the overall microstructure and mechanical properties of the steel constant up to 1473 K.

In Chapter 6, Positron Annihilation Doppler Broadening (*PADB*) is used to investigate the thermal evolution of defects present in different ODS steels and their interaction with oxide nanoparticles. An important hypothesis is proposed in this chapter: during annealing at high

temperatures (1400 K and above), equilibrium thermal vacancies are trapped at the interfaces of oxide nanoparticles. Upon cooling to room temperature, these vacancies are retained in the structure.

In order to further investigate the hypothesis proposed in Chapter 6, in Chapter 7 the ODS 12 Cr steel in its as-received condition and annealed at 1573 K is exposed to low-energy deuterium plasma. Thermal Desorption Spectroscopy (*TDS*) is used to measure the deuterium absorbed by the ODS 12 Cr steel. Interestingly, the deuterium intake is higher in the annealed condition than in the as-received condition. This result is discussed in relation to the ability of oxide nanoparticles to trap defects of different nature.

## 2. Background

### 2.1. Basics of radiation damage in metallic materials

Neutrons released during fusion and fission reactions, when impinging structural materials, normally present kinetic energies high enough to displace atoms from their lattice positions, by means of collisions with the nuclei [34], [39]. The threshold energy that a striking neutron must have in order to displace lattice atoms has to be higher than the so-called displacement energy,  $E_{dis}$ , of the lattice atom. If the kinetic energy of the neutron is lower than  $E_{dis}$ , the collision will only make the lattice atom vibrate around its position; if the kinetic energy of the neutron is equal to or higher than  $E_{dis}$ , the lattice atom will be displaced by the collision and a primary knock-on atom, *PKA*, will be created [40]. The energy transferred during the collision being sufficiently high, the displaced *PKA* atom will further collide with its neighbours, creating a cascade of defects. The  $E_{dis}$  for formation of *PKA* atoms depends on factors like temperature, direction of collision and existence of strains in the lattice. Beeler et al. [41] determined  $E_{dis}$  ranging from 23 to 88 eV, between 300 K and 500 K, for body centered cubic iron. In tungsten, the  $E_{dis}$  has been calculated to be 90 eV by [42] and 55 eV by [43] and [44]. These energies are several orders of magnitude lower than the energies of neutrons produced in nuclear reactors (2 MeV-14.1 MeV [34]) and, hence, creation of *PKAs* and cascade of defects will take place in the structural components of reactors.

In this process, the basic types of defects that directly form are vacancies and self-interstitial atoms, *SIA*s [34], [39], [40]. These can recombine, but can also form various types of defects (Figure 1.3): Frenkel pairs (vacancy and adjacent *SIA*), clusters of displaced atoms, dislocations loops, microvoids, voids and crowdions (defect composed of a displaced atom

sharing a lattice position with another atom) [34], [39], [40]. Alloying elements in solid solution can form precipitates in these processes. In addition, neutrons can react with the nuclei of atoms composing the impinged structure and activate them. Depending on the type of element, different reaction products can be formed: gamma radiation ( $\gamma$ ), He, transmuted atoms, etc [34], [39], [40]. The degree of damage caused by radiation is measured in displacements per atom, *dpa*.

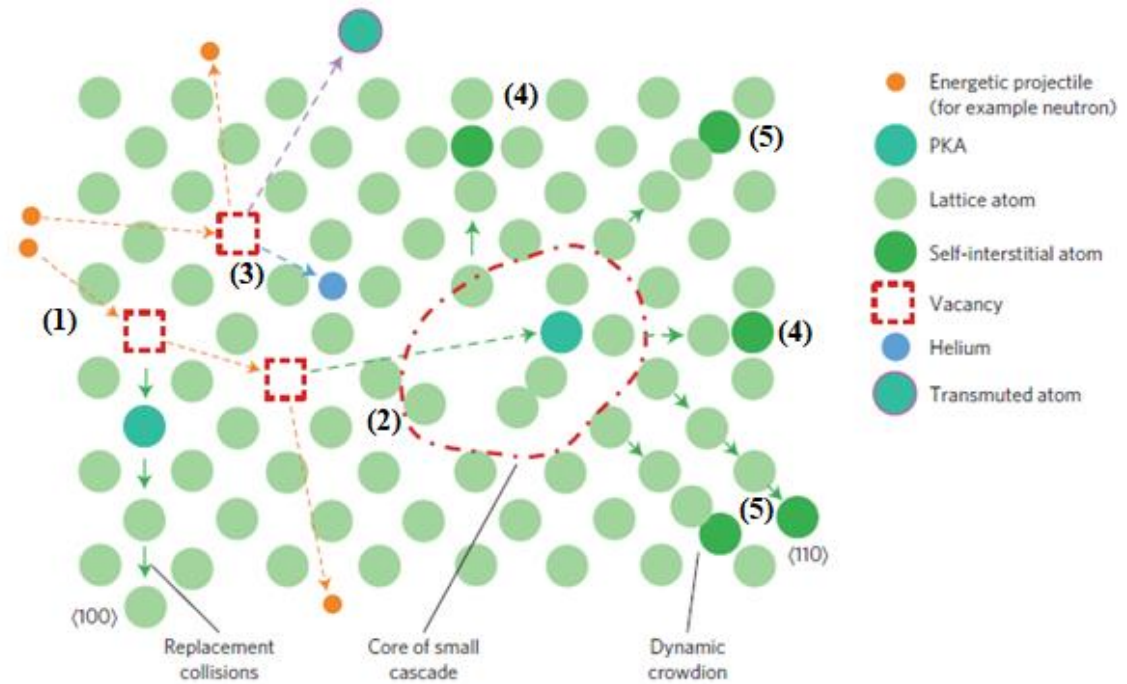


**Figure 1. 3.** Schematic illustrating some types of defects formed in metals due to interactions with energetic particles, like neutrons. In (1) is represented the creation of a primary knock-on atom (PKA), after collision with a neutron. A vacancy is left in the original lattice position of the PKA; still in (1), the PKA occupies another lattice position (annihilation with a pre-existent vacancy). In (2), the PKA has enough kinetic energy to displace other lattice atoms and thus to generate a cascade of defects. In (3) is represented the case when the neutron reacts with the nucleus of a lattice atom, resulting in a transmuted atom and Helium. In (4) the formation of a self-interstitial atom (SIA) is depicted and in (5) is shown the formation of a crowdion, i.e. displaced atom sharing a lattice site with another atom. Extracted from [34].

Radiation-induced defects introduced in the microstructure will have several effects on the properties and performance of materials. According to Zinkle and Busby [33], there are five main effects occurring in materials due to the interaction with radiation: (1) radiation hardening and embrittlement, (2) phase instabilities from radiation-induced precipitation, (3) irradiation creep, (4) volumetric swelling and (5) high-temperature helium embrittlement [33].

Effect (1), radiation hardening and embrittlement, is common at relatively low temperatures, typically below  $0.4T_M$  ( $T_M$  is the melting temperature) and under radiation doses higher than 0.1 dpa. In this case, the defects formed act as obstacles to dislocations movement,

thereby hardening the material and, consequently, reducing its ductility and fracture toughness [33].

Effect (2), phase instabilities from radiation-induced precipitation, is more likely to occur at intermediate temperatures, ranging from  $0.3$  to  $0.6T_M$ , and for doses of 1 dpa to 10 dpa. At these temperatures, the mobility of displaced atoms is relatively high, and they will tend to migrate and bind to sites that will reduce their potential energy, like grain boundaries, surfaces, dislocations and other types of microstructural defects. If atoms of a specific alloying element have a preferential association with the defect flux, segregation will occur [45]. Segregation interferes strongly on phase transformations, and may lead to the localized formation of specific microconstituents, like precipitates or brittle phases, which can become stress raisers (crack nucleation sites). In addition, segregation can be the cause of localized corrosion [33], by the formation of microgalvanic cells between the alloying element-rich region and the depleted one, and other forms of corrosion, like intergranular stress-corrosion cracking, which is an issue for steels containing Cr [45].

Effects (3) and (4) occur under the same conditions of temperature and radiation dose as effect (2). Irradiation creep depends also on the application of external stresses [46]. Creep can be defined as the deformation of a material with time, under a constant load and at intermediate-to-high temperatures. In cases in which radiation is not involved, high temperatures are needed for creep, since the principle behind this phenomenon is the motion of vacancies and dislocations. However, if the material is irradiated, creep will occur more easily, at lower temperatures, due to the increase in density of radiation-induced defects (vacancies and dislocation loops, mainly) [40].

As mentioned earlier, another possible consequence of the neutron bombardment of a material is the transmutation of alloying elements accompanied by helium (He) production [47]. In fusion reactors, He is the main product of the fusion reaction and can enter into the structural components. Once inside the metallic structure, He atoms will diffuse and become trapped at defects, like grain boundaries, dislocations, vacancies. Prolonged exposure eventually will form He bubbles, among other products, which are detrimental for mechanical properties. The same can occur with H, D and T, particularly relevant for nuclear fusion systems. During neutron irradiation, He forms practically at the same time as the other types of defects (vacancies, *SIA*s, dislocations loops, etc). When operating at temperatures above  $0.5T_M$ , the recombination of vacancies and *SIA*s also takes place, leading to the decrease in their concentration in the material, and thus, the nucleation of He bubbles becomes the

dominant event [47]. In this situation, effect (5) takes place even for low He concentrations and when accumulating at grain boundaries can cause intergranular fracture [40], [47].

## **2.2. Oxide Dispersion Strengthened steels**

Research and development (R&D) of ODS steels is not new. It started in Europe during the 1960's, as part of a research programme between Germany, Belgium and the Netherlands, to design, build and operate sodium-cooled fast breeders [48]. Germany and Belgium shared the responsibility for developing technologies related to the fuel (the fuel itself, cladding, fuel assembly, absorber element, etc), and, in this context, R&D on ODS materials for fuel cladding had begun [48]. More specifically, it was at the SCK-CEN studies centre, in Mol, Belgium, under the leadership of Jean-Jacques Huet, that the first trials of obtaining ODS materials were made, using Fe-Cr stainless ferritic alloys and different oxides, like  $\text{Al}_2\text{O}_3$ , MgO,  $\text{ZrO}_2$ ,  $\text{TiO}_2$  and  $\text{ZrSiO}_4$  [48].

At that time, a ferritic matrix was a better choice than an austenitic one because of certain properties: (1) ferrite has higher thermal conductivity, (2) ferrite has lower thermal expansion and (3) ferrite has a lower susceptibility to He embrittlement [48]. The matrices were stainless ferritic alloys, not steels, because no carbon was present in the chemical composition. The reason for this was that steels were considered to be sensitive to decarburization in the presence of dynamic sodium [48].

Another important aspect to comment upon (perhaps the most important) is why oxide particles, among the known strengthening methods, were chosen. Firstly, an alloy has its strength increased when the movement of dislocations, which can be considered as carriers of plastic deformation, is made more difficult. Addition of solute atoms (solid solution strengthening), increase of the dislocation density in the material (work hardening), increase of grain boundary area (grain refinement) and the presence of precipitates/intermetallic compounds (precipitation hardening) are methods to make alloys more resistant, as they provide obstacles to the movement of dislocations. However, all these methods are sensitive to high temperatures: solute atoms may diffuse and segregate, possibly leading to precipitation, stresses are relieved (stress fields in the lattice, introduced by solute atoms, interact with dislocations and compromise their mobility), dislocations will become more mobile and can annihilate, precipitates/intermetallic compounds may grow or be dissolved in the matrix. Hence, the strengthening effect can be lost at high temperatures, decreasing the performance of the material and reducing its service life-time. A solution to this problem was to add oxide

particles to the alloys: the particles themselves constitute obstacles to dislocations (similar to precipitation hardening), they play a role in grain refinement by pinning grain boundaries [49], and are stable at temperatures even higher than the liquidus of many metals [48], [49].

R&D on ODS materials was not restricted to Europe. In Japan, the Japan Nuclear Cycle Development Institute (JNC) has programmes for developing ODS ferritic/martensitic steels since 1987, also for application as fuel cladding [50]. Martensitic (9 Cr) and ferritic (12 Cr) ODS steels have been successfully developed, both containing  $Y_2O_3$  nanoparticles, and the technologies involved in their manufacturing could be extended to ODS reduced activation steels for fusion systems [50].

Yttria ( $Y_2O_3$ ) is the type of oxide most used in ODS steels because of its stability at high temperature, because of the low solubility of Y and O in ferrite [50], and due to the good mechanical properties provided to the steel [37], [48]. The most suitable method for producing ODS alloys is mechanical alloying, which enables the direct mixing of metallic and oxide powders, allows optimum particle size distribution and ideal dispersion throughout the matrix [37], [48], [49]. Ingot liquid-based metallurgy methods are not appropriate for the fabrication of ODS steels mainly due to the density differences between oxide particles and the liquid metal, which leads to the oxide particles sinking or floating in the melt [43].

The conventional powder-metallurgy fabrication route consists of the following steps: (1) gas atomization of a pre-alloy, (2) mechanical alloying (milling), (3) consolidation of the alloy and (4) thermo-mechanical treatment [35]. Common consolidation methods are hot extrusion, hot isostatic pressing and, more recently, spark plasma sintering [35], [51], [52]. Powder metallurgy methods are more expensive than conventional ingot metallurgy ones and face some challenges, like limited reproducibility of the end product quality, difficulty to scale-up the process to industrial scales and the incomplete understanding of details of processing steps. Alternative methodologies that utilize processes of additive manufacturing and lead to shorter production routes are currently in development [37], [49].

One of the main objectives of the ODS approach is to improve creep properties of reduced-activation ferritic martensitic (RAFM) steels and increase their service temperature to 900 K-1273 K [24], [35], [39]. The oxide nanoparticles, in high number density and average diameter ranging from 3 to 20 nm, improve thermal and radiation-induced creep properties by pinning dislocations and grain boundaries and, thus, hindering dislocation climbing, gliding and grain boundary movement [40], [53], [54]. The thermal stability of the microstructure and, consequently, of the mechanical properties are also correlated to this ability of oxide nanoparticles. In [35], creep tests carried out between 873 K and 973 K, up to rupture times

of 10,000 h showed that ODS Eurofer steels exhibited higher creep strength than the non-ODS Eurofer and F82H steels, which are two classes of reduced activation ferritic-martensitic steels developed for nuclear applications [35]. The superior creep properties of ODS steels were also observed in [55], after creep testing between 723 K and 1023 K.

The oxide nanoparticles are also responsible for the increased resistance to radiation damage of ODS steels [50], [53], [56]. The particles provide preferential sites (traps) for radiation-induced defects, He, H, D, or T atoms; these defects then become inactive in the material, instead of moving through the structure until recombining and forming larger defects, like microvoids, voids or bubbles [48]. In [56] it is reported that two ODS steels, containing 9 and 12 weight % Cr, did not show any reduction in tensile elongation after irradiation at 573 K and 773 K, with doses of 5 and 15 dpa [56]. In [57], void swelling data collected for non-ODS ferritic/martensitic and ODS steels, measured after single ion irradiation at 723 K and 753 K, is compared. The results show that void swelling in ODS steels stays below 5% even for very high damage levels of 500 dpa, whereas for the non-ODS steels, void swelling reaches more than 15% volume increase, for damage levels between 150 and 500 dpa [57].

In the following Chapters more details about the high-temperature behaviour of ODS steels and the interaction of oxide nanoparticles with defects are discussed.

## **Part I**

# **Thermal stability of the microstructure and of oxide nanoparticles in ODS steels**



### 3. Microstructural stability of the 0.3% Y<sub>2</sub>O<sub>3</sub> ODS Eurofer steel

Chapter based on publication:

V. S. M. Pereira, H. Schut, and J. Sietsma, “A study of the microstructural stability and defect evolution in an ODS Eurofer steel by means of Electron Microscopy and Positron Annihilation Spectroscopy,” *J. Nucl. Mater.*, vol. 540, 2020, doi: 10.1016/j.jnucmat.2020.152398.

#### Abstract

An approach to improve the performance of steels for fusion reactors is to reinforce them with oxide nanoparticles. These can hinder dislocation and grain boundary movement and trap radiation-induced defects, thus increasing creep and radiation damage resistance. In this chapter, the thermal stability of the microstructure of a 0.3% Y<sub>2</sub>O<sub>3</sub> ODS Eurofer steel was analysed. Samples were annealed for 1 h under vacuum, from 600 K to 1600 K, followed by cooling inside the furnace. Electron Microscopy techniques and Vickers Hardness were used to characterize the microstructure and evaluate its thermal stability. Several types of events take place simultaneously in the material, due to its initial deformation caused by mechanical alloying, the presence of oxide particles and austenitic phase transformation. Annealing up to 1000 K shows that the Y-O based nanoparticles keep the microstructure refined. Upon cooling from 1200 K (above A<sub>c3</sub>), martensite forms with an equiaxed morphology, instead of the conventional lath form, due to the pinning of prior-austenite grain boundaries by the oxide nanoparticles. Annealing at 1400 K and 1600 K results in the formation of complex microstructures, composed of coarse recrystallized ferrite, nano-equiaxed martensite and coarse martensite laths, likely due to the progressive coarsening of Y-O based nanoparticles and their loss of ability to pin grain boundaries.

**Keywords:** Y-O based nanoparticles, martensitic ODS steel, mechanical alloying, deformation state, thermal-vacancy clusters

### 3.1. Introduction

Steels for nuclear applications must resist severe service conditions, like high temperatures (900 K to 1300 K) and high neutron radiation doses. Also, in order to make nuclear power a safer and more environmentally friendly resource, a current requirement is to use reduced-activation alloying elements in the steel composition [24], [35], [51], [58], [59]. With this approach, irradiated structures that could take hundreds of years to reduce induced radioactivity should take no more than tens of years to reach a safe, low radiation level and then be recycled [58]. Reduced-activation steels have already been developed, like the Eurofer97, however they present poor resistance to radiation-induced creep and the service temperature is limited to 900 K, due to thermal instability of the microstructure. A way to improve these properties is to reinforce the steel with oxide nanoparticles, which are able to hinder dislocation and grain boundary movement and to trap radiation-induced defects.

The fabrication method of ODS steels is based on mechanical alloying, which enables the direct mixing of metallic and oxide powders, allowing a homogeneous distribution of oxide particles in the matrix. The standard manufacturing powder-metallurgy route consists of the following steps: (1) gas atomization of a pre-alloy, (2) mechanical alloying of the metallic and oxide powders, (3) consolidation of the ODS alloy by extrusion, hot isostatic pressing or plasma-assisted sintering and (4) thermo-mechanical treatments like hot rolling, forging and cold rolling. [35], [43], [51], [52]

Pre-alloy powders of 9% Cr steels, like the Eurofer97 alloy, produced in step (1) have a microstructure formed by martensite laths. The oxide powders usually consist of crystallites with average diameters ranging from 20 to 100 nm [36], [60]. After step (2), the mechanically-alloyed powders (MA powders) will present a very fine microstructure with an average grain size of tens of nanometers [61]. At this point, the martensite laths from the pre-alloyed powders transform into a more equiaxed structure with high density of dislocations ( $\sim 10^{16} \text{ m}^{-2}$ ) [60], [62]. Also, when milling ODS steel powders, the degree of refinement of the resultant microstructure will depend on the density of added oxide particles and on their chemical nature [36]. Cayron et al. [36] have observed the influence of both parameters on the microstructure of as-MA ODS Eurofer powders. In comparison with  $\text{MgAl}_2\text{O}_4$ , addition of  $\text{Y}_2\text{O}_3$  leads to a finer microstructure. A higher content of  $\text{Y}_2\text{O}_3$  causes a smaller grain size [36]. Additionally, Cayron et al. [36] conclude that  $\text{MgAl}_2\text{O}_4$  does not dissolve in the steel matrix during mechanical alloying, while  $\text{Y}_2\text{O}_3$  does [36]. Other authors [38], [51], [60], [62], [63] have also

found that  $Y_2O_3$  dissolves progressively in the matrix during mechanical alloying and re-precipitates as nanosized clusters in the other processing steps.

The chemical composition of the oxide clusters and their size distribution depend on the alloying elements added to the steel [51], [54], [61], [62], [63]. Kimura et al. [63] detected precipitation of  $Y_2O_3$  and  $YCrO_3$  in a 24% Cr ODS ferritic steel during annealing at 1200 K. A similar temperature was determined for a 13% Cr-3% Ti- $Y_2O_3$  steel and the re-precipitated clusters were identified as  $Y_2TiO_5$  and  $Y_2Ti_2O_7$  [62]. Brocq et al. [64] proposed a new process for producing  $Y_2O_3$  ODS steels called reactive-inspired ball-milling. In this new process,  $YFe_3$  and  $Fe_2O_3$  oxide powders were milled with a Fe-14Cr-W-1Ti pre-alloy, and the authors have observed re-precipitation of oxide nanoclusters after milling and their growth during annealing at 1000 K for 1 h [38].

Commonly, during consolidation, the MA-powders are exposed to temperatures between 1100 K and 1400 K and, therefore, precipitation of Y-based oxide nanoclusters is likely to occur in this stage. It has been reported by different authors [36], [37], [60], [62], [65], [66] that consolidated  $Y_2O_3$ -ODS steels present a microstructure composed of micrometric grains (3-15  $\mu m$ ) surrounded by smaller ones, with average diameter of hundreds of nanometers. The main reasons for this bimodal microstructure are the high deformation energy stored in the material, due to mechanical alloying, and the presence of oxide nanoparticles [60], [62], [65]. Briefly, the MA-powders have a high dislocation density and a large grain boundary area caused by the nano-sized grains. Therefore, they have a strong potential to go through microstructural alterations like recovery and recrystallization [61], [67]. At the same time, the Y-based oxide nanoclusters exert a pinning force on dislocations and grain boundaries that hinder their movement (Zener pinning force). In this unstable state, regions of the material that have a low density of oxide nanoclusters might experience abnormal grain growth, which can be further assisted by an uneven temperature distribution during hot-processing steps [60], [65].

In 9% Cr ODS steels there is an extra factor to consider when describing the consolidated and thermo-mechanically treated microstructures: the  $\alpha \rightarrow \gamma$  phase transition and the  $\gamma$  decomposition upon cooling. Yamamoto et al. [66] observed with *in situ* X-Ray Diffraction, dilatometry and thermodynamic analyses that, irrespective of temperature, the transformation of ferrite into austenite is not complete in 9% Cr  $Y_2O_3$ -ODS steels. The Y-O based nanoclusters would favour ferrite retention by pinning  $\alpha/\gamma$  interfaces [66]. It has also been reported that martensite laths do not form in 9% Cr  $Y_2O_3$ -ODS steels [36], [66], [68] even upon water quench. Again, a possible explanation is based on the Y-O nanoclusters, which would hinder the growth of austenite grains. In this way, austenitic grains would keep a

nanometric average grain size and would not provide space for the growth of martensite laths during subsequent quenching [36], [68].

The mechanisms involved in the microstructure evolution of ODS steels are complex, mainly because of the presence of Y-O based nanoclusters and the highly deformed structure obtained during mechanical alloying. Particularly for 9% Cr  $Y_2O_3$ -ODS steels, the nature of the consolidated microstructure is not clear, i.e., whether it is formed by ferrite, martensite or a combination of both or is affected by recrystallization and ferrite retention at high temperatures. Therefore, in the present paper we assess the microstructural stability, possible phase transformations and defect evolution in a 0.3%  $Y_2O_3$  ODS Eurofer, after a series of annealing treatments. The aim is to characterize the microstructure after each annealing step and to identify processes like recovery, recrystallization and retention of ferrite.

## **3.2. Experimental**

### **3.2.1. Material and heat treatments**

The route used for fabrication of the 0.3%  $Y_2O_3$  ODS Eurofer steel consisted of mechanical alloying, hot isostatic pressing, hot rolling, further thermal treatments at austenitizing temperatures, in order to form martensite upon cooling to room temperature, and further tempering stages [69]. Table 3.1 presents the chemical composition of the steel, determined with X-Ray Fluorescence (heavy metallic elements) and Combustion Analysis (C and S). The samples used for the X-Ray Fluorescence (XRF) analysis were already annealed (description in the following paragraphs) and the ones used for C and S determination were in the as-received condition. Due to a limitation in the amount of material for the study, we could not perform Combustion Analysis for determination of the N and O contents. Finally, it should be noted that the Ta content is not displayed in Table 3.1. Ta is an alloying element commonly added to ODS and non-ODS Eurofer steels, in a typical content of 0.1 weight% [35]. It improves strength and the ductile-brittle transition temperature, due to the formation of TaC that contribute to microstructure refinement, especially in non-ODS Eurofer [35]. The Ta content measured by XRF in our material was below the detection limit (~0.01 weight%), therefore lower than the usual content for Eurofer.

**Table 3. 1.** Chemical composition of the steel, in weight%. The chemical composition of the present steel is slightly different from other ODS Eurofer steels, due to a lower Ta content.

	<b>Fe</b>	<b>C</b>	<b>Cr</b>	<b>W</b>	<b>V</b>	<b>Mn</b>	<b>Ta</b>	<b>Y</b>	<b>O*</b>	<b>Si</b>	<b>S</b>
Content in weight %	Bal.	0.11	9.18	1.01	0.19	0.39	Below detection limit (~0.01)	0.18	0.05	0.04	0.005

\*Estimated value, assuming that all O added to the steel is in Y<sub>2</sub>O<sub>3</sub> form.

The austenitization and tempering conditions used by the producer are unknown, therefore, in order to create a reference state, the material was initially austenitized at 1253 K for 0.5 h and, after cooling to room temperature, tempered at 1033 K for 1.5 h. All samples had dimensions of 12 x 12 x 0.3 mm<sup>3</sup>, prior to the creation of the reference state, and were cut from the top surface of the original plate, at aleatory positions along the thickness of the plate. The treatments described were done in a resistance heating furnace built at the Reactor Institute Delft, under a low pressure of 10<sup>-7</sup> mbar. After each heating step described in this chapter, the cooling was always made inside the furnace, at the same pressure of 10<sup>-7</sup> mbar, by switching off its power supply. The cooling rate in this condition is not constant and depends on the temperature difference between the sample and the environment.

Next, the samples were further heat treated in the same furnace and vacuum condition for 1 h, at different temperatures: 600 K, 800 K, 1000 K, 1200 K, 1400 K and 1600 K. Again, the cooling took place inside the furnace. Figure 3.1 shows the temperature profile for the sample treated at 1600 K, in order to illustrate the non-constant cooling behaviour. The data displayed in Figure 3.1 was measured during the process and we can see a cooling time of 10 min between 1050 K and 750 K, which is a temperature range critical for phase transformations, leading to an average cooling rate of 0.5 K.s<sup>-1</sup> at this range.

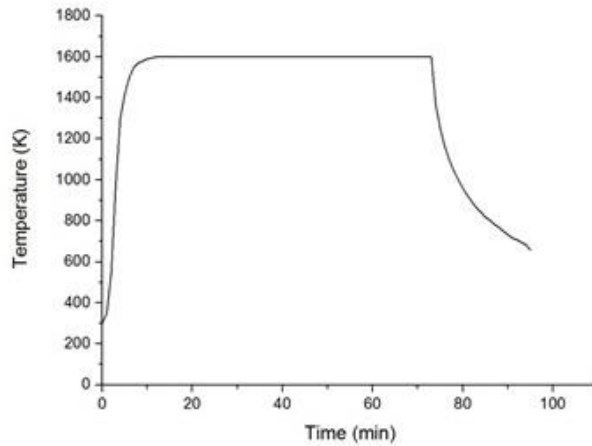


**Figure 3. 1.** Thermal cycle of sample annealed at 1600 K, to show the cooling rate induced by switching-off the furnace.

In order to have a reference for the phase transformations that can occur in the material, the Fe-Cr equilibrium diagram for the non-ODS Eurofer steel was calculated using ThermoCalc version 2018a. The alloy composition considered and database selected were, respectively, Fe-0.1C-9.18Cr-1.070W-0.196V and TCFE9: Steels/Fe-alloys v9.0.

The transformation temperatures of the ODS Eurofer steel were determined experimentally using a Bähr DIL805A/D dilatometer. A sample in the reference state was heated up to 1573 K, at a heating rate of  $1 \text{ K}\cdot\text{s}^{-1}$ , maintained at this temperature for 5 min and finally cooled down by switching off the heating power of the dilatometer, inducing an approximate cooling rate of  $6 \text{ K}\cdot\text{s}^{-1}$  between 1050 K and 750 K.

### 3.2.2. Methods

Scanning Electron Microscopy (SEM), Energy Dispersive X-Ray Spectroscopy (EDS) and Electron Backscattered Diffraction (EBSD) were used to characterize the microstructure of the 0.3%  $\text{Y}_2\text{O}_3$  ODS Eurofer steel in the reference state and after annealing treatments. For SEM and EDS, the samples were polished with diamond suspension up to  $1 \mu\text{m}$  and then etched with Kalling's 1. Preparation for EBSD included an additional polishing step with a neutral alumina suspension of particle size  $0.04 \mu\text{m}$ . The Scanning Electron Microscope used was a JEOL 6500FD equipped with a Thermo Fisher NSS EDS system. EBSD measurements were done with a step size of  $0.1 \mu\text{m}$  in a FEI Quanta-450 Field Emission Scanning Electron Microscope with a Hiraki-Pro EBSD detector. The software used for data analysis was EDAX-TSL OIM Data Collection 7. The volume fraction of sub-micrometric and micrometric

precipitates was determined according to the ASTM E1245-03 standard [70], using six different secondary electron images per sample and the image analysis software *ImageJ*.

Vickers hardness measurements were made in order to track this mechanical property with the different heat treatments; the load used was 0.3 kgf and nine indentations per sample were made throughout the surface. Because of the load used, the hardness measured was a result of the contribution of several grains per indentation.

### 3.3. Results

Figure 3.2 shows isopleths of the equilibrium diagram calculated with Thermo-Calc for our steel, without the addition of ODS particles. Figure 3.2(a) displays a general identification of the microconstituents, including the phases formed in the miscibility gap, while Figure 3.2(b) presents all phases that can be formed at a Cr content of 9 weight %, indicated by the vertical line in the diagram. Besides the well-known  $\gamma$  (FCC) and  $\alpha$  (BCC),  $\delta$  is the paramagnetic high-temperature ferrite,  $M_{23}C_6$  is a Cr-rich carbide, Laves Phase is a complex intermetallic phase rich in W,  $\sigma$  is an Fe-Cr intermetallic and  $\alpha'$  is the BCC Cr-rich phase product of spinodal decomposition. Figure 3.3 presents the equilibrium molar fractions of the phases identified in Figure 3.2(b) as a function of temperature, where  $\delta$ -ferrite is considered as  $\alpha$ .

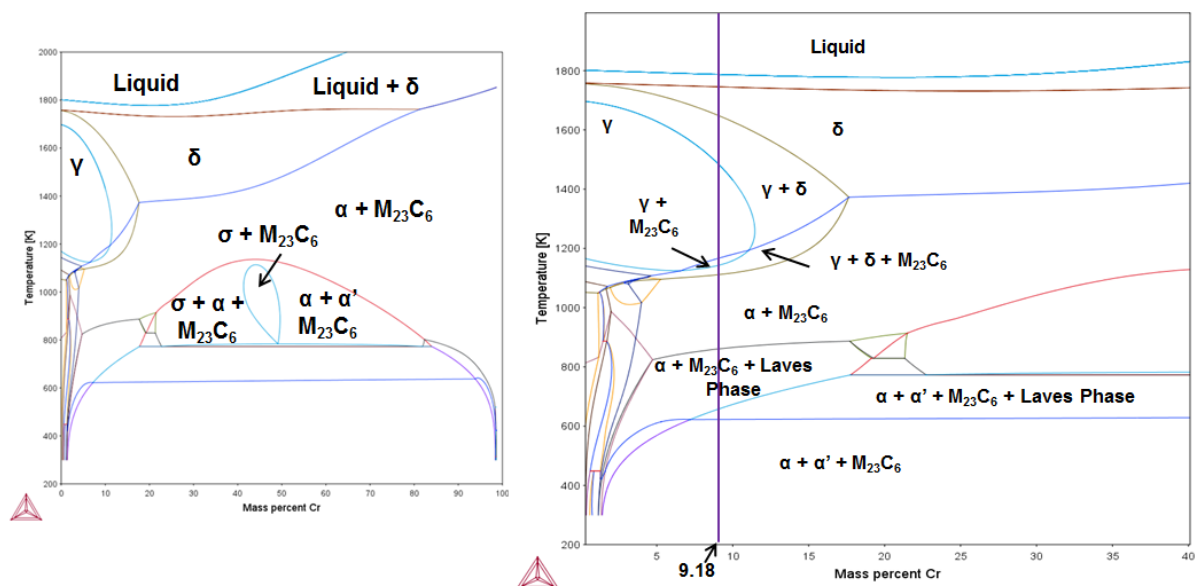


**Figure 3. 2.** Isopleths of the equilibrium diagram calculated with Thermo-Calc for the steel without the addition of ODS particles. In (a) the complete equilibrium diagram and in (b) a more detailed view showing the microconstituents formed with a Cr content of 9.18%. Composition used in Thermo-Calc: Fe-0.1C-9.18Cr-1.07W-0.196V; database selected TCFE9: Steels/Fe-alloys v9.0 .

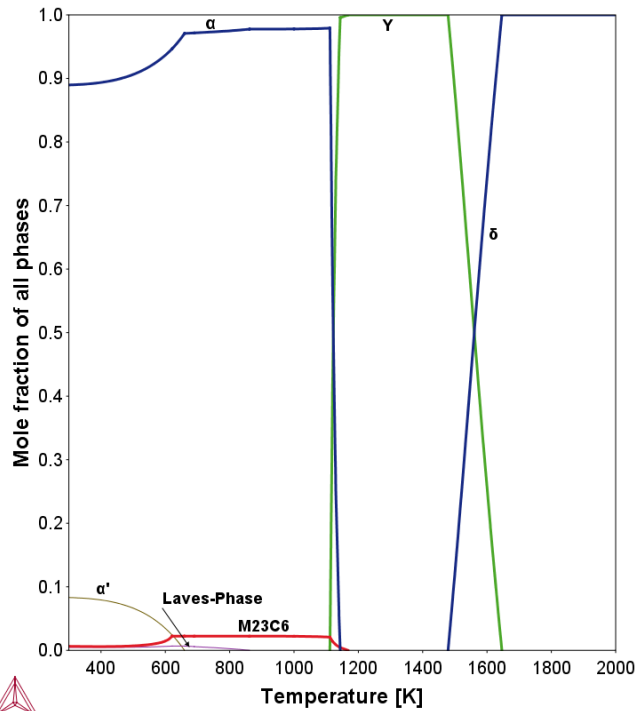


**Figure 3. 3.** Molar fraction of phases formed in equilibrium, calculated with Thermo-Calc for the ODS Eurofer steel. Composition used in Thermo-Calc: Fe-0.1C-9.18Cr-1.07W-0.196V.

Despite their appearance in the equilibrium diagrams, we do not expect to find  $\alpha'$  and Laves Phase in the microstructure of the ODS Eurofer steel. The Laves Phase in 9-12% Cr steels is a microconstituent with hexagonal structure and a general composition of  $(\text{Fe, Cr})_2(\text{W, Mo})$  [71], however, its precipitation is very slow. The Laves Phase appears only after long time exposure to temperatures up to 650 °C (around 900 K) playing, then, a detrimental role in the creep resistance of steels [71], [72], [73]. The spinodal decomposition that produces nanoclusters of  $\alpha$  and  $\alpha'$  is a very slow process in 9-12% Cr steels and typically takes hundreds of hours of exposure to intermediate temperatures to occur [74].

The microstructure of the steel in the different annealing conditions was characterized by SEM, EDS and EBSD. Shape and chemical composition of carbides were obtained with SEM and EDS, while analysis of the matrix was obtained with EBSD. Observation of Y-O based nanoclusters was not possible with any of the mentioned techniques due to their nanometric dimensions (diameter in the range of 4 to 20 nm). The observation of ferrite/martensite grain boundaries was not clear with SEM, while with EBSD it was not possible to obtain information about the precipitates ( $\text{M}_{23}\text{C}_6$  carbides, according to ThermoCalc).



Figure 3.4 shows a secondary electron micrograph of the sample annealed at 600 K, in which it is possible to see the carbide precipitates distributed in the matrix. The precipitates correspond to the brighter particles with an approximately spherical shape and diameter varying from 40 nm to 500 nm; some of them are indicated by red arrows. The micrograph shows that the grain boundaries in the matrix cannot be well distinguished with the SEM after etching.

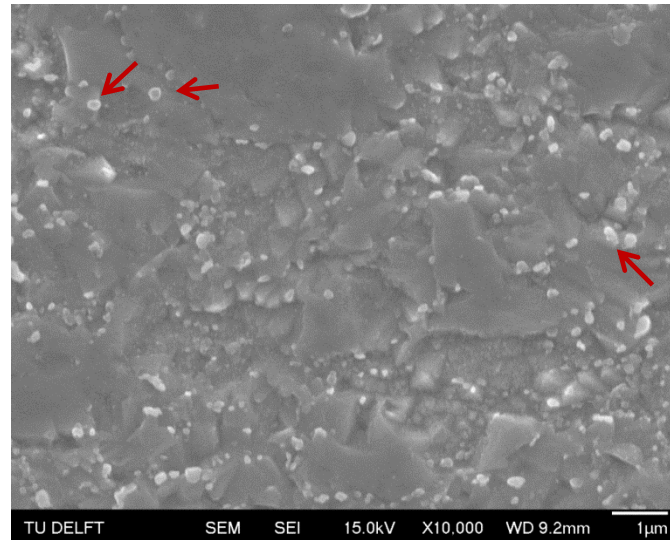


**Figure 3. 4.** Secondary electron micrograph of ODS Eurofer after annealing at 600 K. Etchant: Kallings 1.

The microstructures of samples in the reference state and annealed at 600 K, 800 K and 1000 K are very similar. In these samples, the precipitates have the same morphology, same dispersion in the matrix and, qualitatively, similar diameters, as seen in Figure 3.4. The volume fraction of precipitates under these conditions is given in Table 3.2. After annealing at 1200 K, 1400 K and 1600 K the carbides are dissolved.

**Table 3. 2.** Volume fraction of precipitates calculated for the reference state sample and the samples annealed at 600 K, 800 K and 1000 K.

<b>Sample</b>	<b>Precipitate volume fraction (%) <math>\pm</math> standard deviation</b>
Reference	$3.2 \pm 0.6$
600 K	$4.5 \pm 0.8$
800 K	$3.2 \pm 0.2$
1000 K	$3.7 \pm 1.0$

The experimentally determined volume fractions of precipitates (approximately 4%, Table 3.2) are in agreement with the molar fraction of  $M_{23}C_6$  carbides predicted by Thermo-

Calc (Figure 3.3). The volume fraction of precipitates is low, which agrees with the 0.1 weight % C content in the steel (Table 3.1), and is approximately constant up to 1000 K.

According to the Thermo-Calc estimations, the precipitates seen in the microstructure are  $M_{23}C_6$ . To confirm this, EDS analysis was performed on several precipitates of the ODS Eurofer steel and two distinct composition trends were found: one in which the precipitates have Cr contents higher than 20%, named as P1, and another with Cr content between 10% and 20%, named P2. Table 3.3 presents the average composition of the precipitates (main metallic elements only) and the Thermo-Calc estimation for the composition of the  $M_{23}C_6$  carbide.

**Table 3. 3.** Average chemical composition of precipitates present in the ODS Eurofer steel in the reference state and after annealing at 600 K, 800 K and 1000 K, measured with EDS. For comparison with experimental data, Thermo-Calc estimated composition of the  $M_{23}C_6$  carbide.

Type of precipitate	Average weight% $\pm$ standard deviation of main elements			
	Cr	Fe	W	V
$M_{23}C_6$ – ThermoCalc composition	55	21	16	3
P1	$28 \pm 6$	$64 \pm 9$	$4 \pm 2$	Detected
P2	$15 \pm 3$	$79 \pm 6$	$2 \pm 1$	Detected

The first information we can obtain from Table 3.3 is that the composition measured with EDS is quite different from the Thermo-Calc estimations. The second information relates to the presence of V in the precipitates P1 and P2: V was indeed detected in some of them, but the error associated with the average value  $\pm$  was high. The morphology and contrast of precipitates P1 and P2 are the same. The observations indicate that P1 and P2 precipitates are  $M_{23}C_6$ , but the size of the precipitates in relation to the interaction volume of the electron beam influences the values measured. All EDS measurements were made with an acceleration voltage of 10 keV, which results in an interaction depth of 500 nm (Kanaya-Okayama range) [75]. This interaction depth is larger than the diameter of most carbides observed in the steel, which results in a simultaneous signal from the matrix, leading to the higher Fe contents and higher Cr/W ratio displayed in Table 3.3. Precipitates containing Ta were not encountered in any of the SEM/EDS analysis, reflecting the low Ta content added to the steel (Table 3.1).

Figure 3.5 shows the dilatometry results for the 0.3%  $Y_2O_3$ -ODS Eurofer steel studied. The  $A_{c1}$  and  $A_{c3}$  temperatures correspond to the points of deviation from linear thermal expansion, and are, respectively, 1152 K and 1187 K. The values are in good agreement with the literature [36], [66], [68].

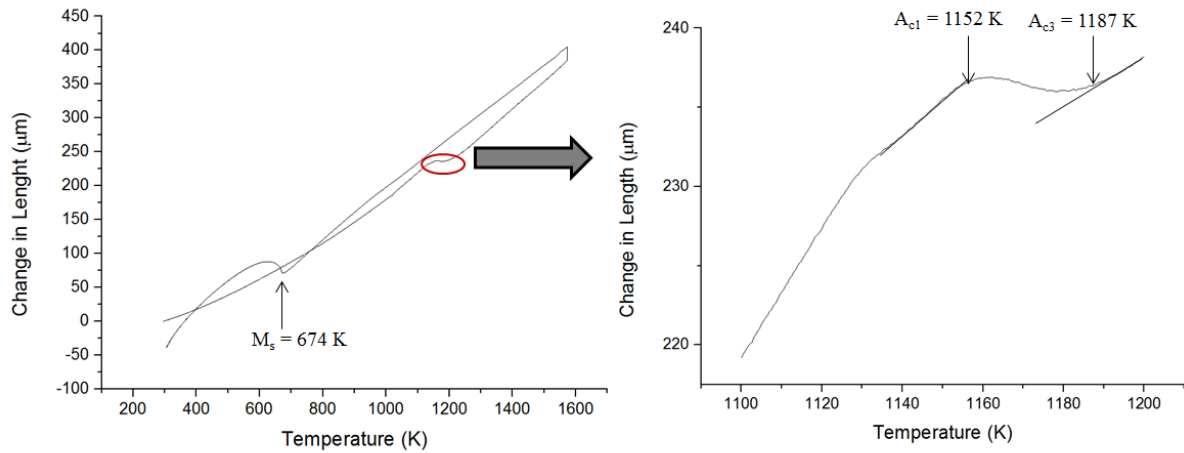


**Figure 3. 5.** Dilatometry curve obtained for the ODS Eurofer steel with a heating rate of  $1 \text{ K}\cdot\text{s}^{-1}$ , until  $1573 \text{ K}$ . After holding for  $5 \text{ min}$  at the maximum temperature, the sample was cooled, at an average rate of  $0.8 \text{ K}\cdot\text{s}^{-1}$ , by switching-off the HF power system of the dilatometer.

Upon heating,  $A_{c1}$  corresponds to the temperature at which the  $\alpha \rightarrow \gamma$  transformation starts. At  $A_{c3}$  the transformation finishes, and this leads to a fully austenitic microstructure in a non-ODS ferritic/martensitic steel. However, there is experimental evidence that in ODS steels the ferrite does not transform completely into austenite, due to the pinning of  $\alpha/\gamma$  interfaces by Y-O based nanoparticles [66]. Upon cooling, we can see a deviation from linearity at  $674 \text{ K}$  (indicated as  $M_s$  in Figure 3.5) that marks the transformation of austenite into martensite. By switching off the power of the dilatometer, between  $1573$  and  $674 \text{ K}$ , the average cooling rate obtained was  $4.6 \text{ K}\cdot\text{s}^{-1}$ , high enough to form martensite in ODS  $9 \text{ Cr}$  steels [76]. According to Ukai et al. [76], ODS  $9 \text{ Cr}$  steels require critical cooling rates in the order of hundreds of  $\text{K}\cdot\text{h}^{-1}$  ( $100 \text{ K}\cdot\text{h}^{-1} = 0.03 \text{ K}\cdot\text{s}^{-1}$ ) to form martensite, while non-ODS  $9 \text{ Cr}$  steels need cooling rates of approximately  $20 \text{ K}\cdot\text{h}^{-1}$ . They attributed the loss in hardenability of ODS  $9 \text{ Cr}$  steels to the presence of oxide nanoparticles [76]. During austenitization, the oxide particles pin the austenite grain boundaries and hinder austenite grain growth. During cooling, laths of martensite do not have space to grow within nanosized prior-austenite grains [76]. The dilatometer curves show that martensite has formed in the  $0.3\% \text{ Y}_2\text{O}_3$ -ODS Eurofer steel, but the morphology is found to be different from laths.

Figure 3.6 shows the orientation image maps of the samples, as obtained by EBSD, which allow the observation of the matrix microstructure of the ODS Eurofer steel. The colour coded map presented is the Inverse Pole Figure (IPF) for ferrite obtained along the normal direction.

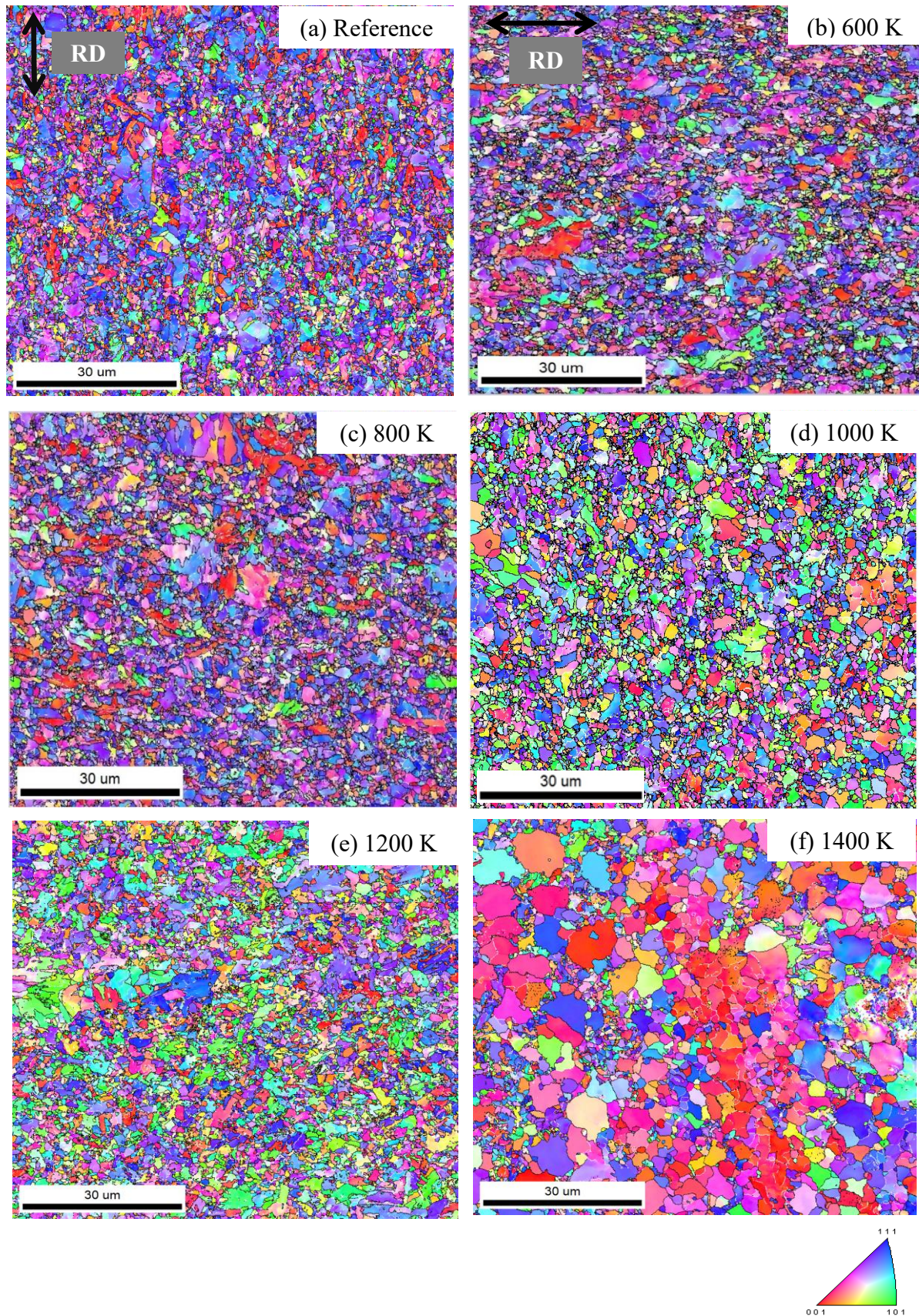
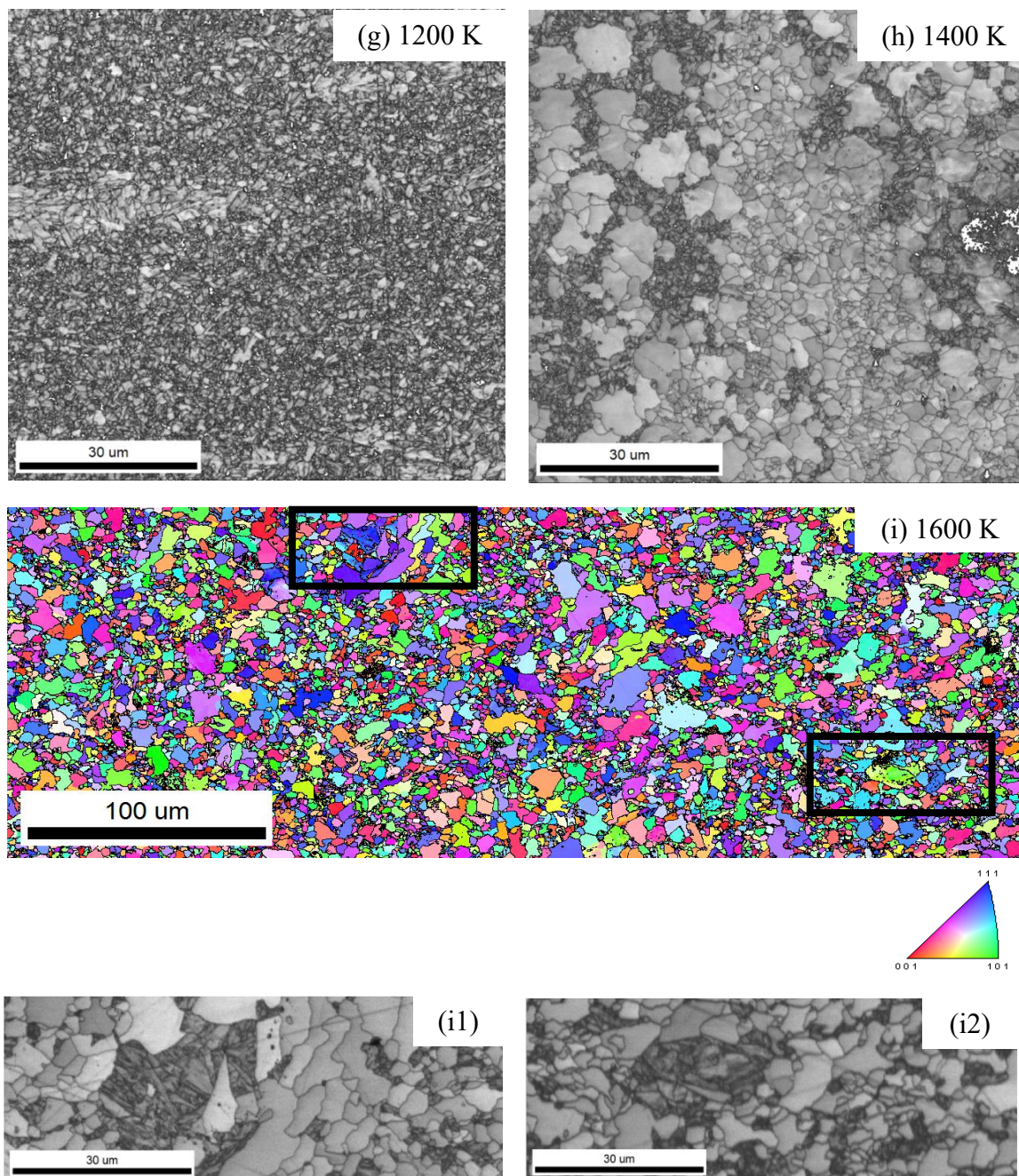


**Figure 3. 6** Orientation image maps obtained for ODS Eurofer steel after annealing at the temperatures indicated for 1h. Colour coded map: inverse pole figure for ferrite obtained along normal direction, Grayscale maps: image quality of samples annealed at (g) 1200 K, (h) 1400 K and (i1, i2) of regions of the sample annealed at 1600 K, containing martensite (darker grains).



**(Continuation) Figure 3.6.** Orientation image maps obtained for ODS Eurofer steel after annealing at the temperatures indicated for 1h. Colour coded map: inverse pole figure for ferrite obtained along normal direction, Grayscale maps: image quality of samples annealed at (g) 1200 K, (h) 1400 K and (i1, i2) of regions of the sample annealed at 1600 K, containing martensite (darker grains).

The microstructures in the reference state and after annealing at 600 K, 800 K and 1000 K are similar. The matrix is formed by micrometric grains (average size varying from a few  $\mu\text{m}$  to tens of  $\mu\text{m}$ ), surrounded by smaller grains, with average size in the order of hundreds of nanometres. This heterogeneous microstructure is characteristic of ODS steels produced by mechanical alloying [36], [37], [60], [62], [65], [66]. The large grains are likely retained ferrite that has undergone grain growth while the smaller grains correspond to tempered martensite.

As a reminder, these samples also contain  $M_{23}C_6$  carbides that were not indexed in the EBSD analysis, but were observed with SEM. The reference state corresponds to a tempered state (austenitization at 1253 K, cooling to room temperature and further tempering at 1033 K for 1.5 h), and annealing at temperatures below the transition to austenite is an extra tempering stage. Within the large grains, an orientation gradient can be noticed, which indicates that the material has not recovered completely from the severe deformation caused by mechanical alloying. The samples in the reference state and annealed at 600 K still retained the grain elongation caused by hot rolling, which is more evident in the micrometric grains. The arrows in Figures 3.6(a) and (b) indicate the working direction and appear different from each other due to positioning inside the microscope, both were cut from the top surface of the original plate. The grain elongation is not visible after annealing above 800 K.

According to Figures 3.3 and 3.5, at 1200 K the material is going through austenitization and, upon cooling, fresh non-lath martensite should form. The approximate cooling rate obtained by switching-off the furnace after this treatment was of  $0.5 \text{ K}\cdot\text{s}^{-1}$ , higher than the critical cooling rate for martensite formation of  $0.03 \text{ K}\cdot\text{s}^{-1}$  determined by Ukai et al. [76]. Therefore, the observed nanometric grains are fresh non-lath martensite and the micrometric grains correspond to retained ferrite. The  $M_{23}C_6$  carbides dissolve during annealing at 1200 K and do not re-precipitate upon cooling, further indicating that, indeed, the final microstructure contains fresh martensite enriched in C. The microstructure of the steel after annealing at 1200 K keeps the degree of refinement seen in the previous conditions, confirming the role of the Y-O based nanoparticles in hindering grain boundary movement.

According to the equilibrium phase diagram (Figure 3.2), at 1400 K the material is in the austenitic field and a microstructure similar to Figure 3.6(e) was expected. Surprisingly, Figure 3.6(f) shows a smaller volume fraction of nanometric non-lath martensite and a higher volume fraction of micrometric grains. Also, it is observed that some of the micrometric grains no longer contain orientation gradients, which indicates the loss of their intrinsic deformation, likely due to recrystallization. The observed grain coarsening suggests that in some regions of the material the oxide nanoparticles did not fully prevent grain growth. This odd aspect is discussed in Section 3.4.

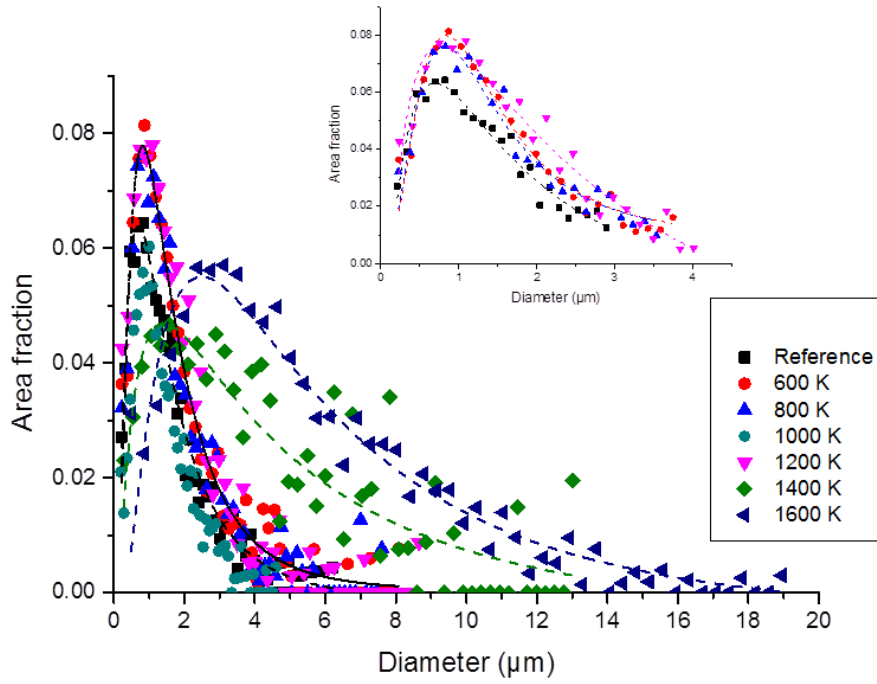
After annealing at 1600 K a coarser, deformation-free microstructure is formed (Figure 3.6(i)), indicating the continuation of the processes started at 1400 K. Also, at 1600 K the material is in the  $\gamma+\delta$  field (Figure 2) and the Image Quality maps in Figures 3.6(i1-i2), obtained at different areas of the same sample, show islands of martensite among the recrystallized  $\delta$ -ferrite, which are not clear in the IPF maps. By highlighting the grains with Grain Average

Image Quality higher than 50000, it was possible to estimate a volume fraction of  $\delta$ -ferrite of 58% and, consequently, of 42% of martensite. Laths of martensite can be seen in regions of the sample where prior austenite grains had grown (Figure 3.6(i1)).

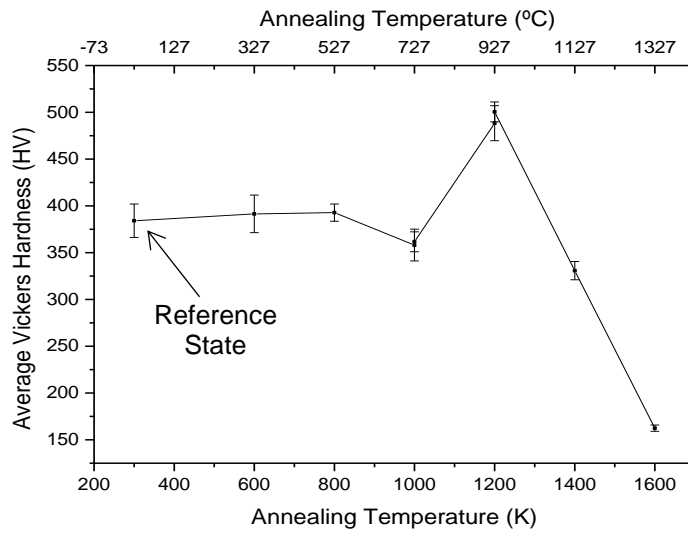
The Inverse Pole Figure maps presented in Figure 3.6 show an effect of the annealing treatments performed on the crystallographic orientation of the samples (qualitatively). Samples in the reference state and annealed at 600 K and 800 K preserved the orientation induced by hot rolling of the material. On the other hand, annealing at 1000 K was enough to alter this crystallographic orientation, resulting in the absence of a preferred grain orientation. The same is observed in samples annealed at 1200 K and 1600 K, due to phase transformations that occurred at these temperatures. However, the origin of the crystallographic orientation seen at 1400 K (Figure 3.6(f)) is unclear.

Figure 3.7 shows the grain size distributions obtained with EBSD for each sample and Figure 3.8 the Vickers hardness results. The grain size distributions follow a lognormal behaviour. In the reference state and after annealing between 600 and 1000 K, the grain size distributions are statistically very similar and this is reflected in the constant Vickers hardness. Nevertheless, the insert in Figure 3.7 containing the zoomed-in of these distributions shows a slight shift towards larger grain sizes for the annealed samples in relation to the reference state, suggesting that sub-grain growth occurs to some extent. In terms of grain size, the sample treated at 1200 K has a behaviour similar to the previous ones, however its Vickers hardness is the highest. This peak in Vickers hardness can be attributed to the formation of fresh equiaxed-martensite and to grain refinement strengthening. The C and other metallic alloying elements that were previously forming  $M_{23}C_6$  carbides are redistributed in the matrix in the form of solid solution or segregated at dislocations and grain boundaries, present in high densities in ODS steels due to mechanical alloying. Therefore, strengthening by solid solution or segregation of alloying elements are contributors for the hardness peak measured.

After annealing at 1400 K, the Vickers hardness has a value similar to that of the reference state and the samples annealed at 600-1000 K. Although its grain size distribution is the most heterogeneous, we can still see a considerable fraction of fine grains with diameter between 1.5 and 4  $\mu\text{m}$  that contribute to the strengthening of the steel (Figure 3.6(h)). We can understand this hardness value by the combination of four factors: presence of martensite, solid solution strengthening, dispersion of Y-O based nanoparticles and a fine grain structure. Finally, we observe a drastic decrease in hardness after annealing at 1600 K, which agrees with the overall coarsening of the microstructure.



**Figure 3. 7.** Grain size distribution obtained for samples in the reference state and after annealing at 600 K, 800 K, 1200 K, 1400 K and 1600 K. Inset: detailed view of encircled peaks of the reference state, 600 K, 800 K and 1200 K samples.



**Figure 3. 8.** Vickers hardness values measured for ODS Eurofer in the reference state and after annealing for 1 h at different temperatures.



### 3.4. Discussion

The microstructural observations made with SEM and EBSD in Section 3.1 show that annealing at 600 K, 800 K or 1000 K does not alter the reference state microstructure significantly, except for the grain size distribution shifting towards higher grain sizes (Figures 3.6(a-d) and Figure 3.7) and a change in the preferential crystallographic orientation, which becomes more aleatory after annealing at 1000 K. Additionally, these annealing treatments do not have an effect on the average Vickers hardness of the material (Figure 3.8). Based on these observations, it is possible to conclude that the only microstructural process occurring with annealing between 600-1000 K is the recovery of the deformed state of the material, introduced during mechanical alloying. After annealing at 1200 K, the Vickers hardness reaches a maximum value, indicating that, upon cooling, the martensitic transformation occurs.

After annealing at 1400 K and 1600 K, the results obtained with SEM, EBSD and Vickers hardness indicate that the Y-O based nanoparticles lose their function of maintaining the microstructure thermally and mechanically stable. However, these techniques cannot give information about the mechanism behind this loss of functionality, whether if it is due to dissolution of the nanoparticles or due to their coarsening. Other authors [36], [77] observed, with Transmission Electron Microscopy, the coarsening of Y-O based nanoparticles, after annealing at 1300-1350 °C (1573-1623 K), in different ODS steels.

Finally, a curious aspect to be discussed is the odd microstructure obtained after annealing at 1400 K. The coexistence of regions with nanometric and micrometric grains (Figure 3.6(f)) indicates that coarsening of oxide nanoparticles has taken place, but not throughout the whole volume of the sample. Hence, in some parts of the sample the main boundary pinning force becomes weaker, allowing grains to grow. At 1400 K the material is in the austenitic field and it is expected that austenite grains subjected to a lower pinning force are able to grow and, upon cooling, form martensite, in lath or block form. Nevertheless, the micrograins seen in Figure 3.6(f) correspond to recrystallized ferrite. The formation mechanism of this microstructure is not clear yet and more experimental investigations, using *in-situ* X-Ray Diffraction, TEM and APT are necessary to understand it. So far, a possible explanation is that recrystallization and growth of retained ferrite is kinetically favoured over austenitization at 1400 K. A first aspect to consider is that the coarsening of oxide nanoparticles, most likely via Ostwald ripening [77], is not an instantaneous process. Hence, during the first minutes of annealing at 1400 K, we can assume that (1) the oxide particles still have their original refined size, (2) incomplete austenitization occurs [66] and (3) the material

is formed by austenite and a certain volume fraction of retained ferrite. According to Sandim et al. [77], Y and O diffuse more easily in ferrite than in austenite, at temperatures as high as 1350 °C (1623 K). Again, in our material the oxide nanoparticles lose thermal stability at a lower temperature. Still, it is possible to assume that coarsening of oxide nanoparticles, at 1400 K, occurs preferentially in the regions containing retained ferrite. With the evolution of annealing time, the retained ferrite, subjected to a weaker pinning force and with a high stored deformation energy, goes through continuous recrystallization [60] and the austenite grain boundaries are pinned by the smaller oxide particles. Metals that are severely deformed, like ODS steels, have a high mean grain boundary misorientation, which leads to the occurrence of continuous recrystallization, i.e., growth of deformed grains, without nucleation of new deformation-free ones [67].

### 3.5. Conclusions

The characterization of the microstructure of the 0.3%  $Y_2O_3$  ODS Eurofer steel, after annealing at different temperatures, lead to the following conclusions:

- i) The Y-O based nanoparticles strongly influence the microstructure and the kinetics of phase transformations of the material.
- ii) The Y-O based nanoparticles are responsible for maintaining the microstructure and the Vickers hardness of the steel stable up to 1000 K.
- iii) After annealing at 1200 K, the Vickers hardness of the material markedly increases, due to the formation of martensite. Nevertheless, the microstructure presents the same degree of refinement as in the previous conditions, due to the pinning effect of Y-O based nanoparticles. At 1200 K, the particles prevent the growth of austenitic grains and, upon cooling, nanometric martensite forms.
- iv) Annealing at 1400 K leads to the formation of an unexpected dual-phase microstructure, composed of recrystallized ferrite and nanometric martensite. This is a first indication that Y-O nanoparticles are going through coarsening in certain regions of the material. During annealing at 1600 K, coarsening of oxide

particles is enhanced and, hence, overall grain growth of  $\delta$ -ferrite and austenite occurs.

## 4. Characterization of oxide nanoparticles present in the ODS Eurofer steel

Chapter based on publication:

V.S.M. Pereira, T. P. Davis, M. H. Mayoral, A. Kumar, H. Schut, J. Sietsma. “Investigation of coarsening of oxide nanoparticles at 1400 K and its effect on the microstructure formation of an ODS Eurofer steel”. *Materials Characterization*, v. 185, 2022, doi: 10.1016/j.matchar.2022.111723

### Abstract

Oxide Dispersion Strengthened (ODS) steels are potential candidate materials for application as structural components of fission and fusion reactors, known for their high thermal stability, high resistance to creep and to radiation-induced damage. These attractive properties result from the presence of the fine and highly thermally stable yttrium-oxygen (Y-O) based nanoparticles, which exert a strong Zener pinning force to hinder the grain boundary movement, and are able to pin dislocations and trap radiation induced defects. In the present work, the effect of annealing at 1400 K on the microstructure and oxide nanoparticles in a 0.3% Y<sub>2</sub>O<sub>3</sub> ODS Eurofer steel was assessed. The material was characterized with Scanning Electron Microscopy, Transmission Electron Microscopy and Atom Probe Tomography in a reference condition and after annealing at 1400 K, followed by cooling at different rates. The results showed that the average diameter of the oxide nanoparticles increases from  $3.70 \pm 0.01$  nm to  $5.30 \pm 0.04$  nm, after annealing at 1400 K for 1 h. The particles present a well-known core/shell structure, with a core rich in Y, O and V and a shell rich in Cr. The effect of the increase in oxide nanoparticle size on the microstructure is discussed in terms of the Zener pinning force.

**Keywords:** Atom Probe Tomography, Transmission Electron Microscopy,  $\alpha/\gamma$  phase transformation, interface velocity, core/shell structure of particles

## 4.1. Introduction

Oxide Dispersion Strengthened (ODS) steels have been developed and extensively researched in the past decades due to their potential for application as structural components in nuclear fission and fusion reactors [57], [78]. The oxide nanoparticles dispersed in the matrix, with typical particle size varying from 3 nm to 20 nm [53], are able to pin dislocations and hinder grain boundary movement; the particles can also act as efficient trapping sites for radiation-induced damage. The matrix of ODS steels is commonly ferritic (Cr content higher than 12 weight%), or composed of mixture of tempered martensite and ferrite (9-10 weight % Cr). Therefore, ODS steels present high tensile strength, good ductility and, most importantly, high thermal stability of the microstructure, high resistance to creep and improved resistance to radiation-induced embrittlement. [79], [76]

Yttrium oxide ( $Y_2O_3$ ) is the type of oxide that is most commonly used in ODS steels because of its high thermal stability and, consequently, for providing superior mechanical properties, in comparison to other types of oxides [80], [36]. The  $Y_2O_3$  particles are incorporated by mechanical alloying with the metallic powders of the alloying elements to constitute the steel. During this process, the  $Y_2O_3$  particles initially in powder form dissolve in the matrix and, only during the subsequent fabrication steps, they re-precipitate in the form of Y-O based nanoparticles. The chemical composition and crystal structure of the precipitated nanoparticles depend on the alloying elements present in the material and on the processing parameters. Y-O based nanoparticles have been reported by several authors to be highly thermally stable. Zilnyk et al. [80] did not observe any significant alteration in Y-O based particles dispersed in an ODS Eurofer steel after annealing at 1073 K for 6 months. The coarsening of Y-O based particles in ODS Eurofer has been observed only after annealing at the range 1500-1600 K, which leads also to the overall coarsening of the microstructure [77], [81]. The high stability of fine Y-O based nanoparticles is attributed to a high coherency of the interface of the particle with the ferrite matrix, which results in a small driving force for coarsening, and the low solubility of Y and O in Fe [79], [80], [82].

Nevertheless, in Chapter 3 significant instability of the microstructure of the 0.3%  $Y_2O_3$  ODS Eurofer steel was observed after annealing at 1400 K for 1 h. Upon moderate cooling to room temperature, a high volume fraction of recrystallized ferrite was formed, accompanied by lath martensite and equiaxed martensite. The described microstructure contradicts Thermo-Calc predictions for the steel, which should be austenitic at 1400 K, and observations made by other authors [81], [68]. A possible explanation for the microstructure described above is that

a fraction of the Y-O based nanoparticles in the particular steel go through coarsening during annealing at 1400 K, reducing the Zener pinning force. In the present Chapter, we investigate the possible coarsening of Y-O nanoparticles present in the 0.3%  $Y_2O_3$  ODS Eurofer, after annealing at 1400 K. In addition, the oxide nanoparticles are characterized with Transmission Electron Microscopy and Atom Probe Tomography.

## **4.2. Experimental**

### **4.2.1. Material**

The material studied is the 0.3%  $Y_2O_3$  ODS Eurofer steel, produced by conventional powder metallurgy route (mechanical alloying, HIP and thermomechanical treatments) and previously characterized in Chapter 3. Its simplified chemical composition, in weight percent, is Fe-0.1C-9Cr-1W-0.2V-0.4Mn-0.3 $Y_2O_3$ . The material goes through austenitic transformation, with  $Ac_1 = 1152$  K,  $Ac_3 = 1187$  K and  $M_s = 674$  K, determined by dilatometry (Figure 3.5). According to ThermoCalc calculations, the steel should be fully austenitic between  $\sim 1170$  K and  $\sim 1500$  K; between 1500 and  $\sim 1650$  K, the material should be formed by austenite and delta ferrite.

In the present work, the 0.3%  $Y_2O_3$  ODS Eurofer steel is analysed in the reference state and annealed at 1400 K for 1 h. The reference state was created by austenitization at 1253 K for 0.5 h, cooling to room temperature and tempered at 1033 K for 1.5 h. The treatments were performed in a resistance heating furnace, under a pressure of  $10^{-7}$  mbar. The cooling after each step of the treatment was done inside the furnace, leading to an average cooling rate of  $0.5 \text{ K}\cdot\text{s}^{-1}$  between 1050 K and 750 K, a temperature range that is critical for phase transformations. Subsequently, further annealing at 1400 K for 1 h was performed in the same conditions and cooling. More details about the chemical composition of the steel, dilatometry and the heat treatments in the resistance heating furnace are described in Section 3.2.1. In order to evaluate the effect of the cooling rate on the microstructure, an extra condition was created. It consisted of 1 h annealing at 1400 K, in a tubular furnace, under  $N_2$  atmosphere, and cooling to room temperature by water quench. This sample is referred as 1400 K-WQ and the sample cooled inside the furnace is referred as 1400 K-FC.

#### 4.2.2. Methods

The overall microstructure of the 0.3% Y<sub>2</sub>O<sub>3</sub> ODS Eurofer steel in its reference state and after annealing at 1400 K (1400 K-FC and 1400 K-WQ) was evaluated using Scanning Electron Microscopy (SEM) and Vickers hardness. The microscope used for SEM analysis was a JEOL 6500FD microscope and the samples were etched with Kallings' 1. For the Vickers Hardness measurements, a load of 0.3 kgf in a Struers Durascan 70 device was used.

Transmission Electron Microscopy (TEM) and Atom Probe Tomography (APT) analyses were carried out to characterize the Y-O based nanoparticles in the reference state and 1400 K-FC. The samples for TEM examination were in the form of discs with 3 mm diameter, punched out from 0.3 mm thick plates. Mechanical polishing of the discs was performed to reach a final thickness of 0.1 mm. Finally, electropolishing in a Tenupol 5 machine with a mixture of 5% perchloric acid and methanol, at 213 K (-60 °C), was performed to reach electron transparency. TEM examination was carried out using standard imaging methods of Bright Field (BF) and Weak Beam Dark Field (WBDF) in a TEM JEOL JEM-2100, with LaB<sub>6</sub> filament and operating at 200 keV, available at the National Centre of Electron Microscopy (CNME), Madrid, Spain. Furthermore, STEM mode analysis was applied in both High-Angle Annular Dark Field (HAADF) and BF modes in the Talos Field Emission Gun TEM/STEM, available at the Institute of Madrid for Advanced Studies in Materials (IMDEA), Madrid, Spain. Compositional maps of areas observed with TEM were obtained using Energy Dispersive Spectroscopy (EDS).

Quantitative analyses of the TEM images were done using the software *ImageJ 1.53c*, in order to determine the size distribution and number density of the Y-O based nanoparticles. For the calculation of size distributions, the particles are approximated as spheres and, thus, the particle size is given as the diameter. A total of 1887 particles were measured for each analysed condition. The number density of particles corresponds to the number of particles counted in different TEM images per unit volume. A total of 6 images per condition were measured, and the thickness of the TEM samples was estimated to be 100 nm.

The APT specimens were first bulk-milled by Focused Ion Beam (FIB)-milling in a dual-beam Helios GE UXe SEM/FIB, located at the Department of Materials Science and Engineering, Delft University of Technology. Final cleaning of the specimens was performed using 2 kV Ga ions in a Zeiss Crossbeam 540 Analytical FIB-SEM at the Department of Materials, University of Oxford. The APT analyses were conducted with a CAMECA LEAP® 5000XR instrument, also at the Department of Materials from the University of Oxford. The

atom probe tips were cooled down and maintained at 55 K. The APT measurements were made in laser mode, under ultra-high vacuum, with a frequency tripled Nd:YAG laser, with 355 nm wave-length, operating at 40 pJ and 200 kHz. The average detection rate was of 1.0% and the detection efficiency of the LEAP 5000XR is 52% [83]. The 3D reconstructions of chemical atomic maps and overall data analysis were made with the software CAMECA IVAS® 3.8.4. Information about the oxide nanoparticles, like chemical composition, size distribution and number density were obtained using the tool “Cluster Analysis” of IVAS and following a maximum separation method, as conducted by Davis et al. [84]. The parameters used for the cluster analysis were refined for each data set, to maximise the accuracy of detection of the nanoparticles. Table 4.1 summarizes the range of parameters and types of ions used in the cluster analyses of oxide particles in the reference state and annealed at 1400 K.

**Table 4. 1.** Parameters used in the cluster analysis with IVAS, determined with the maximum separation method.

	Ions	$KNN$ (order of nearest neighbour distribution)	$N_{min}$ , atoms (minimum critical size of cluster)	$d_{max}$ , nm (maximum distance between atoms in a detected cluster)	$d_e$ , nm (erosion)	$L$ , nm (envelope)
Reference State	Y, O, V, $YO^{2+}$ , $VO^{2+}$	1 to 3	5 to 22	0.8 to 1.1	0.4 to 0.55	0.4 to 0.55
1400 K-FC	Y, $VO^{2+}$ , $YO^{2+}$	1 to 3	6 to 10	0.8 to 1.0	0.4 to 0.5	0.4 to 0.5

### 4.3. Results

#### 4.3.1. Characterization of oxide nanoparticles in the reference state and after annealing at 1400 K

Figures 4.1(a) and 4.1(b) contain secondary electrons micrographs of the samples 1400 K-FC and 1400 K-WQ, respectively; Figure 4.1(c) shows the microstructure in the reference state. The average Vickers hardness measured in each condition is also shown. Figures 4.1(d) and 4.1(d1) contain bright-field TEM micrographs of the sample 1400 K-FC, showing in more detail the microstructure composed of coarse recrystallized ferrite (light grey, deformation-free grains) and martensite (dark regions). In Figure 4.1(e), the microstructure in the reference state is shown for comparison.

In the reference state the material contains tempered martensite, retained ferrite and  $M_{23}C_6$  carbides (indicated by red arrows in Figure 4.1(c)). The retained ferrite corresponds to a fraction of ferrite that does not transform into austenite at temperatures above  $A_{c3}$ , due to the



pinning of the  $\alpha/\gamma$  interface by Y-O based nanoparticles [66], [85], [86]. According to ThermoCalc calculations shown in Figure 3.2 (Chapter 3), the equilibrium phase at 1400 K should be austenite and, considering the effect of oxide nanoparticles, the expected microstructure upon cooling to room temperature should be similar to the one described for the reference state, but without the  $M_{23}C_6$  carbides. However, it is seen in Figures 4.1(a) and 4.1(d) a mixture of coarse recrystallized ferrite, martensite laths and equiaxed nanosized martensite. The microstructure of sample 1400 K-WQ contains also grains of recrystallized ferrite, indicated in Figure 4.1(b), surrounded by areas of a rough aspect. It has been seen in the characterization of the matrix with EBSD (Figure 3.6) that these rough areas correspond to nanosized equiaxed martensite, which are completely corroded during etching. The Vickers hardness values measured after annealing at 1400 K are lower than in the reference state, in agreement with the coarser and partially recrystallized microstructure formed (grain size distributions are found in Figure 3.7). In addition, the Vickers hardness measured in the sample 1400 K-WQ is very heterogeneous, as indicated by its high standard deviation. Some regions of the samples present hardness of  $\sim 400$  HV and others have hardness of  $\sim 310$  HV.

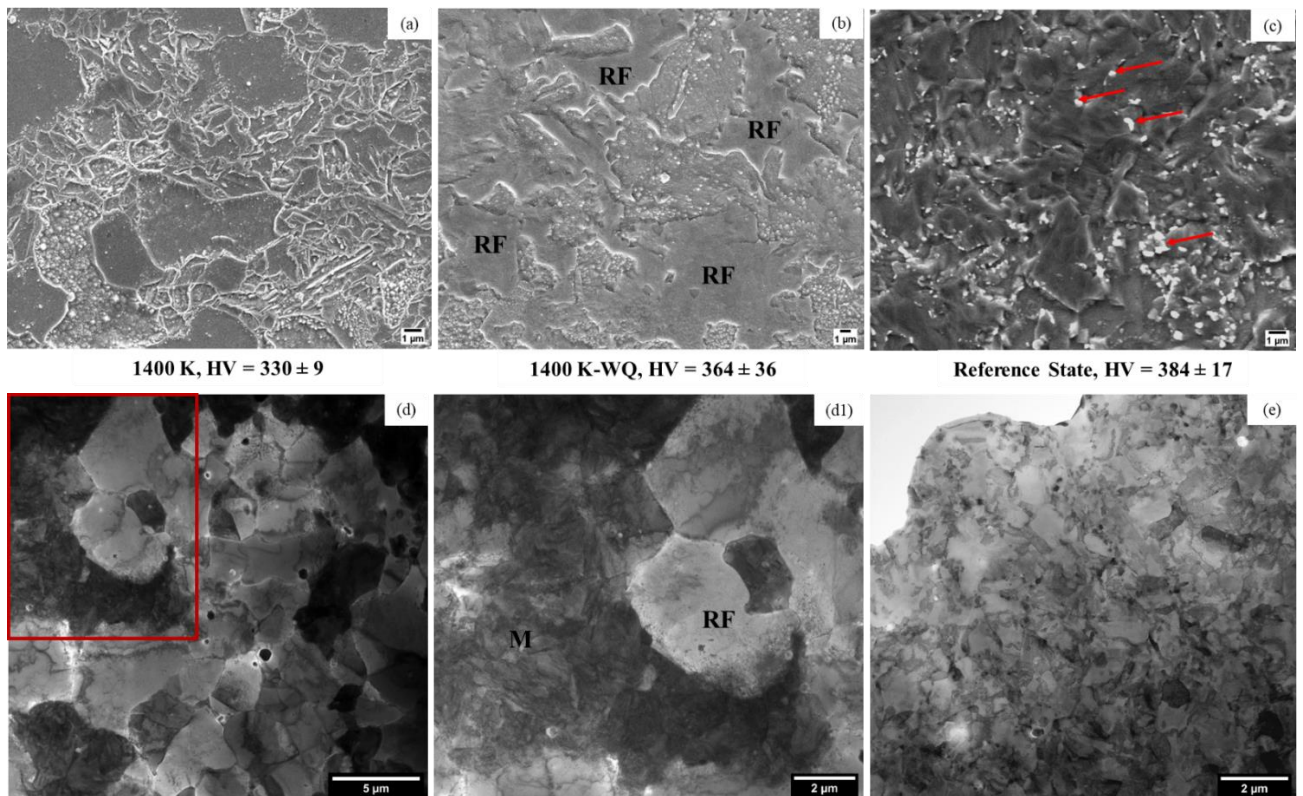


**Figure 4. 1.** Secondary electron micrographs of the 0.3%  $Y_2O_3$  ODS Eurofer steel and respective average Vickers hardness in the (a) condition of annealing at 1400 K, followed by furnace cooling (1400 K-FC), (b) annealed at 1400 K and water quenched (1400 K-WQ) and (c) reference state. (d) and (d1) Bright-field micrographs showing in more detail the martensite (M) and recrystallized ferrite (RF) in the sample 1400 K-FC and (e) reference state.

Figures 4.2(a) and 4.2(b) show the Y-O based nanoparticles in the reference state, Figures 4.2(c-e) show the particles in the material annealed at 1400 K-FC. It is possible to see in Figures 4.2(a-e) that the particle size is not homogeneous in any of the cases and examination of different regions of the samples indicate that the particles can be found either inside grains or adjacent to grain boundaries – no preferential disposition of oxide nanoparticles along microstructural features is observed. Figure 4.2(c) shows regions with low density of oxide nanoparticles and in Figure 4.2(d), a small band free of oxide nanoparticles can be seen (indicated by red rectangle).

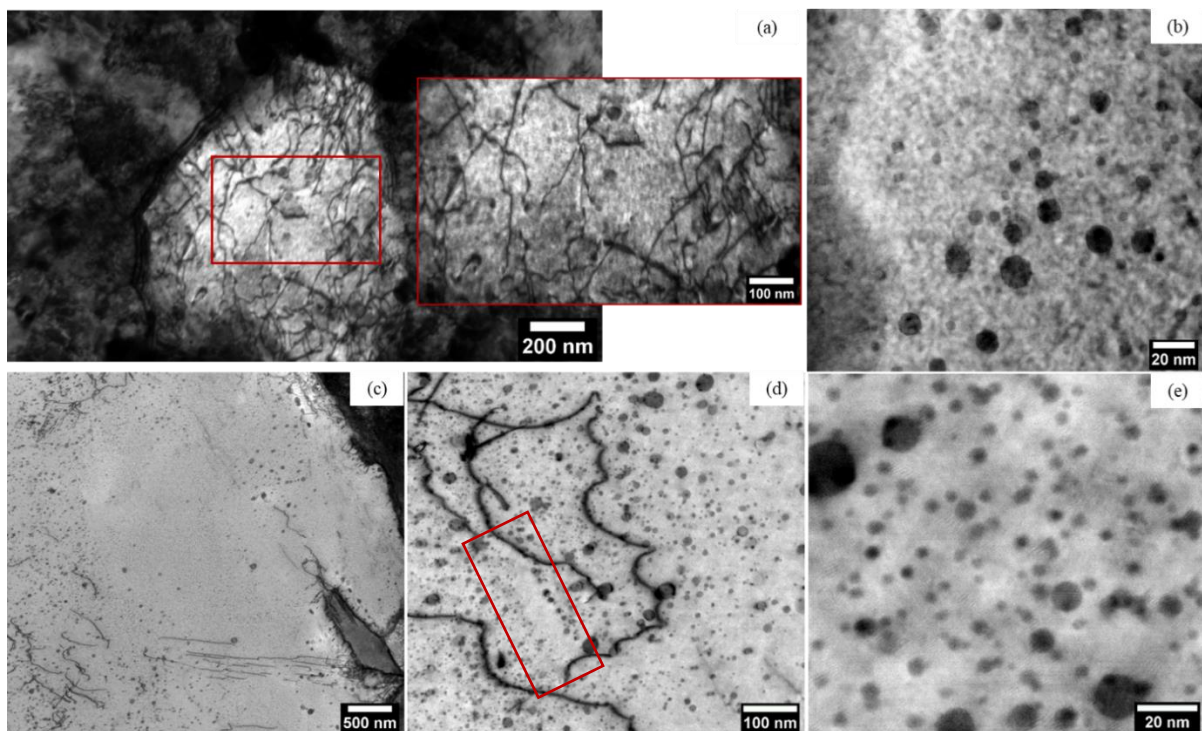


**Figure 4. 2.** Bright-field micrographs of the 0.3%  $Y_2O_3$  ODS Eurofer showing Y-O based nanoparticles and their distribution in the matrix. In (a) and (b) the material is in the reference state and in (c), (d) and (e) in the condition 1400 K-FC.

APT analyses were performed on multiple samples taken from different regions of the microstructure, some containing multiple nanosized grains, others taken from larger, micrometric grains. Figure 4.3 contains 3D reconstructions of representative tips in the reference state and annealed at 1400 K-FC. In order to visualize the distribution of atoms and ions throughout the tips, and have qualitative information about the composition of the tips, the reconstructions are given in the form of elemental maps. The reconstructions of Figure 4.3(a), of a tip in the reference state, presents two ferrite grains, part of an  $M_{23}C_6$  carbide (bottom of the tip) and oxide nanoparticles evenly distributed. The  $M_{23}C_6$  carbide is rich in Cr, W and V, in agreement with EDS analysis presented in Table 3.3; Si and Mn are also observed in the

carbide. The oxide nanoparticles are rich in Y, V and O, which were also detected in the form of the complex ions  $\text{VO}^{2+}$  and  $\text{YO}^{2+}$ ,  $\text{CrO}^{2+}$  and  $\text{VN}^{2+}$  ions are also present in the oxide nanoparticles, however, due to their significantly lower contents, maps with these ions are not shown. In Figure 4.3(b), the reconstruction of the tip taken from the annealed sample shows oxide nanoparticles of various sizes, one of them with  $\sim 50$  nm length. Qualitatively, the surrounding matrix is enriched with Cr, W, V, likely due to the dissolution of  $\text{M}_{23}\text{C}_6$  carbides during the annealing treatment. In comparison to the reference state, the contents of Y and O, in particular around the coarser particles, are also higher in the matrix. In addition, the coarser oxide particles appear enriched with Si. X-ray Fluorescence analysis of the 0.3%  $\text{Y}_2\text{O}_3$  ODS Eurofer steel, described in Table 3.1., showed that Ta was found in trace amounts within the steel's composition. Ta was not found in any of the APT tips measured, thus, confirming the X-Ray Fluorescence chemical analysis.

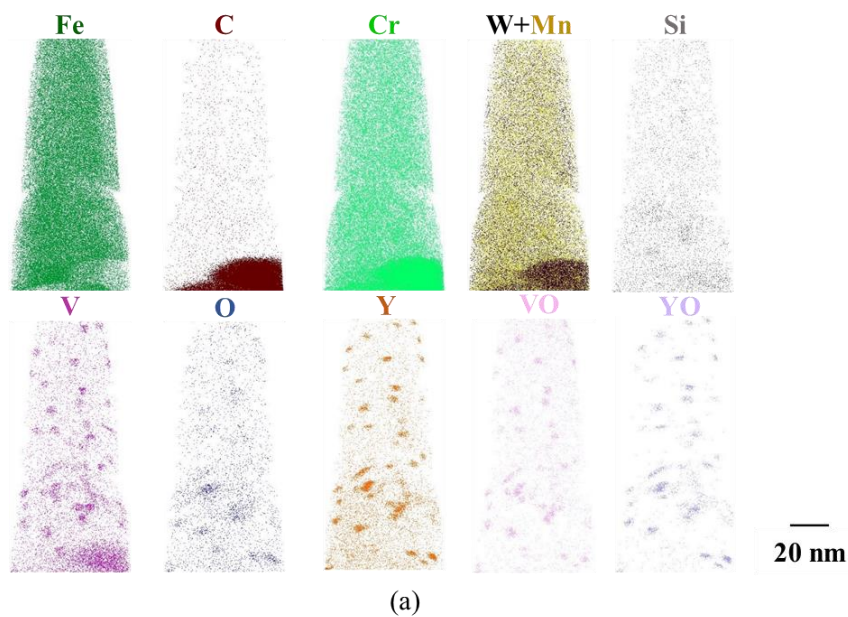
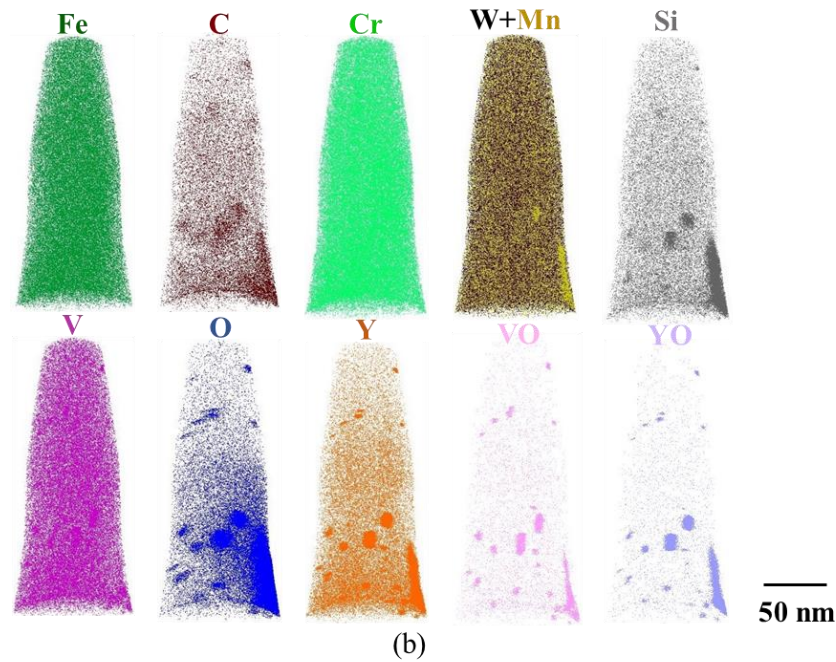


**Figure 4. 3.** Compositional maps of representative reconstructions of 0.3%  $\text{Y}_2\text{O}_3$  ODS Eurofer samples (a) in the reference state and (b) annealed at 1400 K-FC.



(Continuation) **Figure 4.3.** Compositional maps of representative reconstructions of 0.3%  $\text{Y}_2\text{O}_3$  ODS Eurofer samples (a) in the reference state and (b) annealed at 1400 K-FC.

Quantitative information about the chemical composition of the oxide nanoparticles, size distribution and number density were obtained after performing the cluster analysis, as described in section 4.2.2. The size distribution and the number density of particles were also calculated using TEM micrographs. These two techniques have certain limitations, but their combined use is able to give complementary information about the material. TEM can be considered a more appropriate tool for determination of particle size distribution and for general observation of oxide dispersion throughout the matrix, since much larger areas are analysed in comparison to APT. On the other hand, the measurement of the number density of oxide particles with TEM can be more challenging, because of the difficulty in determining the thickness of the samples and, thus, the analysed volume [87]. In the present work, the thickness of TEM samples was estimated to be of 100 nm.

Figure 4.4(a) presents the particle size distributions measured with TEM and APT. In the reference condition, both techniques show that  $\sim 96\%$  of the oxide nanoparticles have a diameter smaller than 8 nm, the remaining 4% have sizes up to 22 nm. For the annealed condition, the size distribution obtained with TEM is broader and shows coarsening of oxide nanoparticles, in which 78% of the particles with diameter smaller than 8 nm and 22% with sizes from 8 nm to 50 nm. The peak of the distribution calculated with TEM shifts from  $3.7 \pm 0.01$  nm to  $5.3 \pm 0.04$  nm with annealing at 1400 K. The same trend is observed with APT,

with the peak of the distribution changing from  $5.0 \pm 0.1$  nm in the reference state to  $6.0 \pm 0.1$  nm in the annealed condition.

In Figure 4.4(b) the number density of oxide particles determined with APT is shown, and corresponds to  $2.0 \times 10^{23}$  particles.m<sup>-3</sup> in the reference state and  $1.1 \times 10^{23}$  particles.m<sup>-3</sup> in the annealed condition. The decrease in number density is consistent with the particle coarsening discussed in Figure 4.4(a). The number densities derived from TEM micrographs are one order of magnitude lower than the obtained with APT, and no difference between reference state and annealed condition could be seen. The reason for this discrepancy is related to the limitations associated with TEM, discussed previously. In particular for the reference state, the number density of particles calculated with TEM images is underestimated: the material was in a state of high deformation that strongly affected the contrast between the matrix and oxide nanoparticles (Figure 4.2(b)).

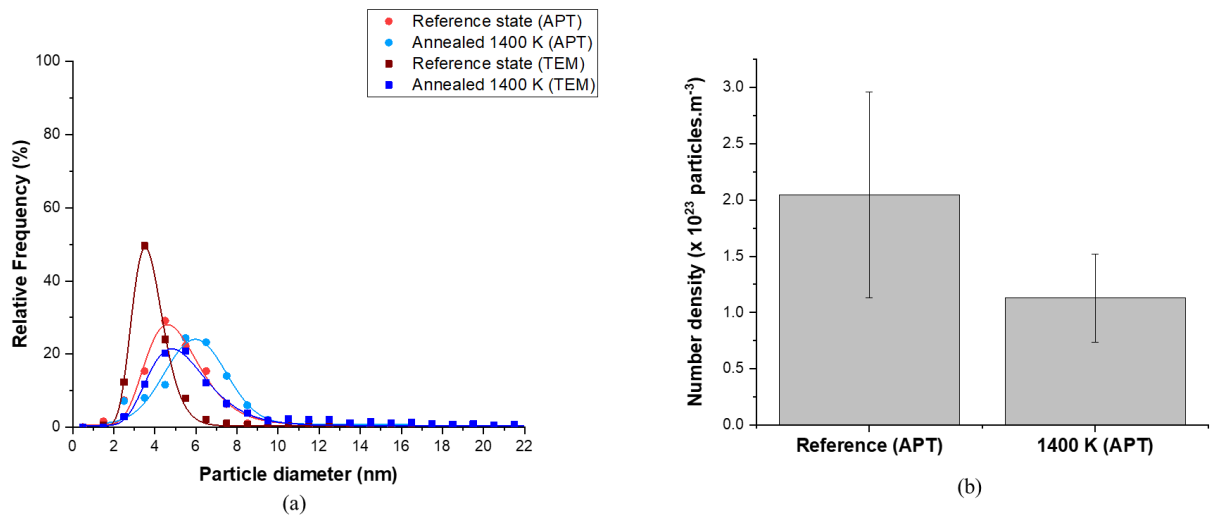


**Figure 4. 4.** (a) Particle size distributions and (b) number density of oxide nanoparticles calculated for the 0.3% Y<sub>2</sub>O<sub>3</sub> ODS Eurofer steel in the reference state and annealed at 1400 K-FC, using TEM and APT.

The average chemical composition of all nanoparticles detected in the cluster analysis is given in Table 4.2. The main elements contained in the particles are Y, O, Cr and V. Overall, the average composition of the nanoparticles was not largely affected by the annealing treatment at 1400 K, except for a slight decrease in the V content. A possible relation between particle size and chemical composition was taken into account in our analysis, but no consistent correlation was encountered. In Figure 4.5, elemental maps of the sample annealed at 1400 K, obtained with EDS-TEM, show the absence of Fe atoms inside the oxide nanoparticles, especially on the larger ones. Hirata et al. [79] also reported the absence of Fe in Y-O based

nanoparticles using STEM-EELS maps. The high Fe concentration measured with APT is related to ion trajectory aberrations during the APT measurements, discussed in [88], [89], [90].

**Table 4. 2.** Average chemical composition of the oxide nanoparticles, in atomic percentage, determined by cluster analysis of APT data.

	C	Si	O	Cr	V	Fe	Mn	Y	W
<b>Reference state</b>	$0.2 \pm 0.8$	$0.4 \pm 0.4$	$12.7 \pm 5$	$12.5 \pm 9$	$8.4 \pm 6$	$44.8 \pm 13$	$0.6 \pm 0.5$	$19.1 \pm 10$	$0.2 \pm 0.4$
<b>Without Fe</b>	$0.3 \pm 1.0$	$0.7 \pm 0.7$	$23.0 \pm 6$	$23.5 \pm 13$	$15.4 \pm 8$	-	$1.3 \pm 1.0$	$33.7 \pm 12$	$0.4 \pm 0.6$
<b>Annealed 1400 K</b>	$0.3 \pm 0.6$	$0.3 \pm 0.3$	$10.3 \pm 6$	$8.9 \pm 2$	$5.0 \pm 4$	$59.5 \pm 11$	$0.6 \pm 0.4$	$14.0 \pm 6$	$0.3 \pm 0.6$
<b>Without Fe</b>	$0.8 \pm 0.9$	$0.8 \pm 0.7$	$24.8 \pm 7$	$23.8 \pm 8$	$11.6 \pm 5$	-	$1.6 \pm 1.1$	$34.1 \pm 7$	$0.8 \pm 0.8$

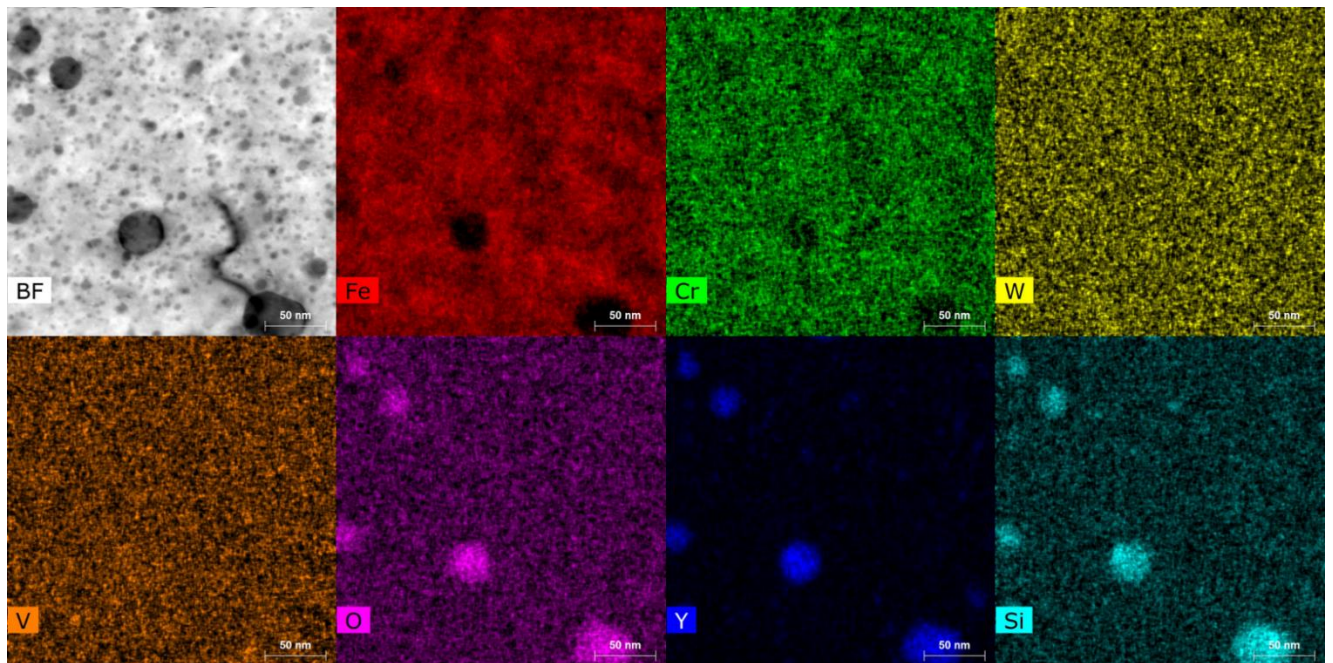


**Figure 4. 5.** Qualitative compositional maps of Y-O based nanoparticles of various sizes, present in the 0.3%  $Y_2O_3$  ODS Eurofer steel annealed at 1400 K-FC.

Figure 4.5 confirms the Si-enrichment of large Y-O based nanoparticles, illustrated in Figure 4.3, and suggests that some of these large particles are Cr-depleted in their cores. Multiple authors observed that Y-O based nanoparticles, present in different ODS steels, have a type of core-shell structure, with a Cr-rich shell and variable core composition [79], [80], [89], [91], [92], [93]. Hence, the structure of the particles in the reference state and annealed samples was assessed by applying an isosurface of 1 atomic % Y on the APT data and by calculating proxigrams and concentration profiles of the particles. The results are presented in Figure 4.6, which contains two significant examples of particles per analysed condition. The software IVAS calculates proxigrams and concentrations profiles considering the presence of

Fe, however, in order to better visualize the concentration curves of the other elements, Fe is removed from the plots. The proxigrams in Figure 4.6(a) and (b), correspondent to particles in the reference state, show the increase in Cr concentration once the interface of the particle is crossed; the Cr concentration seems to achieve a plateau or decrease in the core of the particle. The concentration profiles in Figure 4.6(a1) and (b1) show more clearly the decrease in Cr concentration inside the particle. This behaviour is considered to be indicative of a Cr-shell [80], [89], [91], [92]. Still analysing the particles present in the reference condition, Figures 4.6(a1) and (b1) show a core rich in Y, O, V and smaller concentrations of Si and Mn. The concentrations of W and C are extremely low in the particles and, therefore, are not considered to be part of the core. All analysed particles in the reference state exhibited a Cr-shell and the Cr concentration at the shell varied between ~10 atomic % to ~20 atomic %.

Figures 4.6(c) and (d) show proxigrams calculated for representative particles present in the annealed state. In Figure 4.6(c) the increase in Cr around the particle interface is clearly seen and its respective ROI concentration profile in Figure 4.6(c1) confirms the Cr-shell structure. However, not all particles present in the annealed state exhibited the marked Cr-shell. Figures 4.6(d) and (d1) show an example of particle in which the Cr concentration at the interface is not significantly higher than at the matrix, suggesting the formation of a thinner Cr-shell or its absence. The composition of particles cores in the annealed state is the same as in the reference condition, but some particles are Si and Mn-enriched (Figure 4.6(d1)), in agreement with Figures 4.3(b) and 4.5. Finally, the particle analysed in Figures 4.6(d) and (d1) was located at the end of the APT tip and, for this reason, the average concentration at 10 nm is biased (low ion count number).

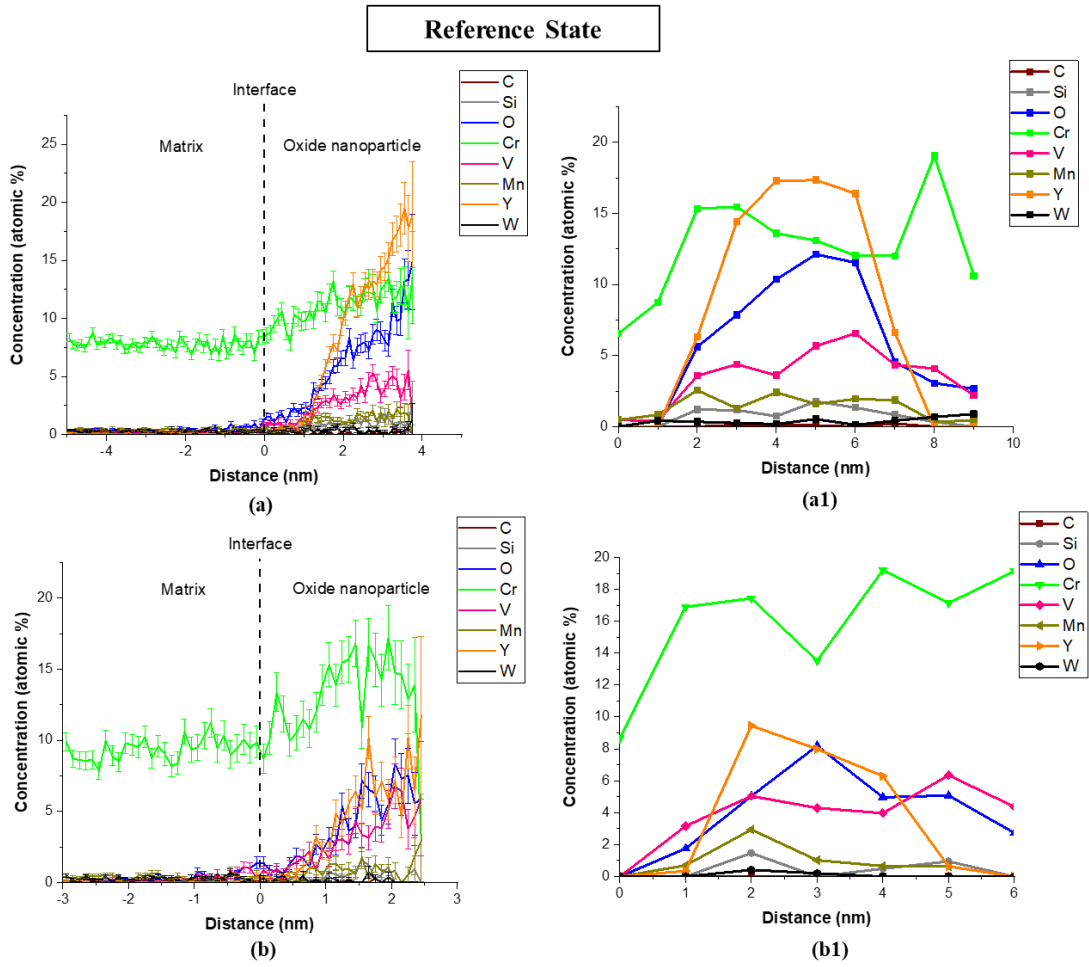
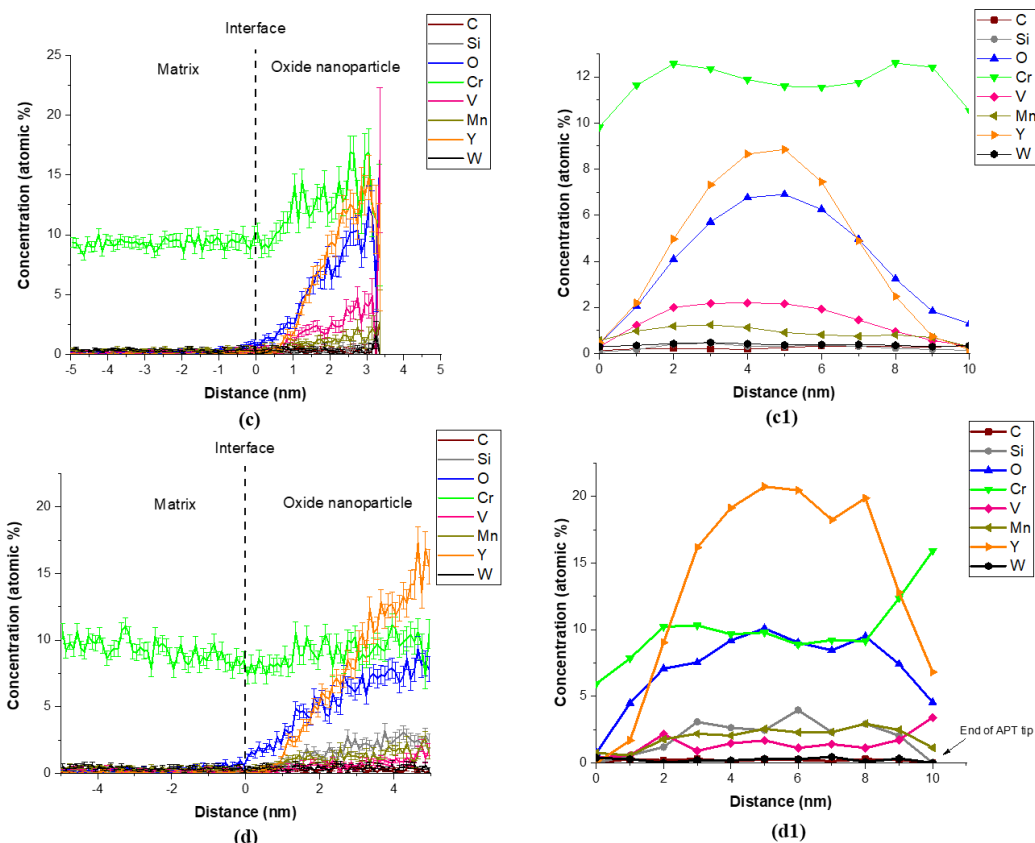


**Figure 4. 6.** (a),(a1) and (b), (b1) Proxigram along 1% Y isosurface and respective concentration profile along ROI of two representative oxide nanoparticles present in the reference state sample. (c),(c1) and (d),(d1) Proxigrams and concentration profiles along ROIs of two particles present in the sample annealed at 1400 K-FC.



### Annealed 1400 K



**(Continuation) Figure 4.6.** (a),(a1) and (b), (b1) Proxigram along 1% Y isosurface and respective concentration profile along ROI of two representative oxide nanoparticles present in the reference state sample. (c),(c1) and (d),(d1) Proxigrams and concentration profiles along ROIs of two particles present in the sample annealed at 1400 K-FC.

In Figure 4.3(b) it can be seen a large oxide nanoparticle present at the bottom right of the reconstruction, with size of  $\sim 60$  nm and rich in O, Y and Si. To further investigate the structural composition of this large particle, isosurfaces of 1 atomic % O and 1 atomic % Y were applied. Figure 4.7 shows in more detail the reconstructed particle with the 1 atomic% O and Y isosurfaces and the proxigrams calculated for these interfaces. The particle clearly has an outer layer rich in O, which also contains a Cr concentration slightly higher than the matrix (Figure 4.7(b)). The core of the particle has high Y and O contents, a Cr content of  $\sim 8$  atomic % (less than the observed for smaller particles), very low V concentration and higher levels of Si and Mn. These results agree with the qualitative composition of large particles ( $> 20$  nm) obtained with the EDS-TEM elemental maps of Figure 4.5.

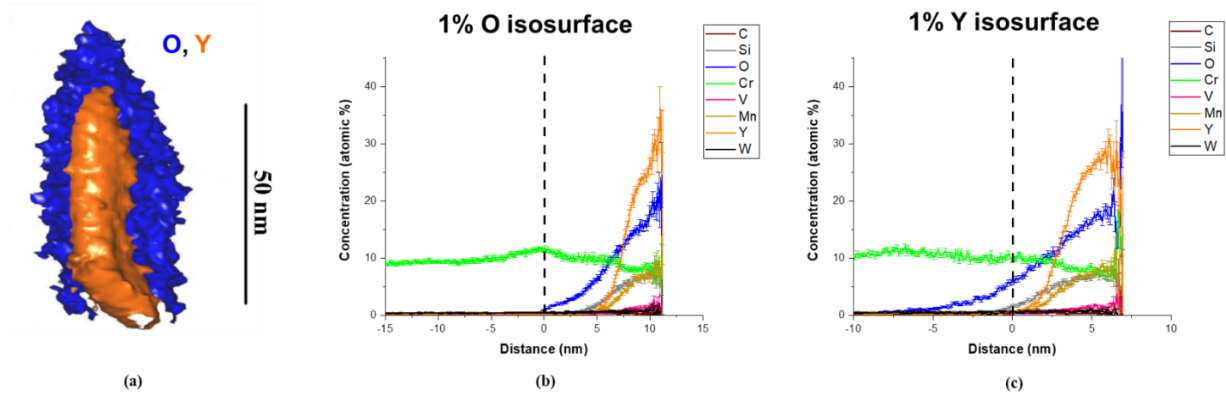


**Figure 4. 7.** (a) Detail of large Y-O nanoparticle present in the sample annealed at 1400 K-FC (shown previously in Figure 3(b), at the bottom right of the reconstruction), with isosurfaces of 1% O and 1% Y applied. (b) and (c) are the correspondent proxigrams.

### 4.3.2. Determination of Zener pinning force

The Zener pinning force originated by the Y-O based nanoparticles was determined for the reference state and annealed condition, using a modified Zener equation [94] that has been applied in the analysis of ODS steels [66], [85]

$$F_Z = \frac{3}{8} \frac{\sigma f^{2/3}}{r} \quad (4.1)$$

where  $F_Z$  is the Zener pinning force,  $\sigma$  is the interfacial energy of grains present in the matrix,  $f$  is the volume fraction of oxide nanoparticles in the material and  $r$  is the radius of the oxide nanoparticles. The volume fraction of oxide nanoparticles in the reference state and after annealing at 1400 K was calculated using the data obtained with APT cluster analysis, by dividing the total volume of oxide particles detected in a sample by the volume of the APT tip. The oxide nanoparticle radius was taken as the weighted average of each size distribution measured with TEM. For pinning of  $\alpha/\gamma$  interface,  $\sigma_{\alpha/\gamma} = 0.56 \text{ J.m}^{-2}$  [68]; for pinning of  $\alpha/\alpha$  boundaries,  $\sigma_{\alpha/\alpha} = 0.32 \text{ J.m}^{-2}$  [95]. The parameters used and the resulting  $F_Z$  are summarized in Table 4.3.

**Table 4. 3.** Parameters used in the modified Zener equation [94] and Zener forces exerted on the  $\alpha/\gamma$  and  $\alpha/\alpha$  interfaces.

	$f$	$r$ (nm)	$\sigma_{\alpha/\gamma} = 0.56 \text{ J.m}^{-2}$	$\sigma_{\alpha/\alpha} = 0.32 \text{ J.m}^{-2}$
			$F_{Z, \alpha/\gamma} (\text{J.m}^{-3})$	$F_{Z, \alpha/\alpha} (\text{J.m}^{-3})$
<b>Reference State</b>	0.02	2.3	$6.9 \times 10^6$	$3.9 \times 10^6$
<b>Annealed at 1400 K</b>	0.02	4.2	$3.4 \times 10^6$	$2.0 \times 10^6$

The results show the decrease of  $F_z$  with the increase of oxide nanoparticle size during annealing at 1400 K, and can be correlated to the overall coarser microstructure obtained after annealing at 1400 K (Figure 4.1).

## 4.4. Discussion

### 4.4.1. Formation of the microstructure during annealing at 1400 K

The hypothesis raised in Chapter 3 to explain the microstructure of the 0.3%  $Y_2O_3$  ODS Eurofer steel, obtained after annealing at 1400 K, was based on the coarsening of oxide nanoparticles during the treatment. The hypothesis was that with coarsening, the Zener pinning force exerted by the particles become weaker, allowing a higher degree of grain growth. In the present work we examined the Y-O based nanoparticles in the reference condition and after annealing at 1400 K, using TEM and APT and found that, indeed, the particles undergo coarsening during the annealing treatment, which leads to the decrease of the Zener pinning force,  $F_z$ .

During annealing at 1400 K different processes have the potential to take place:

- (1) the (incomplete) transformation of ferrite into austenite,
- (2) coarsening of the Y-O based nanoparticles, and
- (3) recrystallization of untransformed ferrite, due to its prior high deformation energy in the reference state.

Multiple studies [66], [85], [86] have shown with dilatometry and *in-situ* X-Ray Diffraction that ODS steels with ferritic/martensitic matrix do not undergo complete austenitization: a fraction of ferrite remains untransformed even at temperatures above  $A_{c3}$  and, upon cooling to room temperature, the retained ferrite grains can be seen dispersed in the martensitic matrix. The suggested reason is that the oxide nanoparticles dispersed in the matrix pin the  $\alpha/\gamma$  interface, decreasing its velocity, and not allowing the complete consumption of the ferrite-parent phase [66], [85]. The driving force for the austenitic transformation,  $\Delta G_{\alpha/\gamma}$ , in the 0.3%  $Y_2O_3$  ODS Eurofer as a function of temperature has been estimated using ThermoCalc 2018a, in order to qualitatively analyse its competition with  $F_{Z,\alpha/\gamma}$ , calculated in Section 4.3.2.  $\Delta G_{\alpha/\gamma}$  was estimated by the difference between the formation energies of austenite and ferrite. This comparison of  $F_{Z,\alpha/\gamma}$  to  $\Delta G_{\alpha/\gamma}$  is considered qualitative because  $F_{Z,\alpha/\gamma}$  will vary

locally within the material, due to the heterogeneity in oxide nanoparticle size, and because the  $\alpha/\gamma$  phase transformation involves other processes like nucleation and partitioning of solute elements. The estimated  $\Delta G_{\alpha/\gamma}$  values are one order of magnitude higher than the  $F_{Z,\alpha/\gamma}$  values presented in Table 4.3, with a maximum at 1300 K of approximately  $1.6 \times 10^7 \text{ J.m}^{-3}$ , confirming that the oxide nanoparticles affect the kinetics of the transformation by an overall decrease in interface velocity, especially when they present a size distribution in the reference state. Another effect that might contribute to the hindering of the  $\alpha/\gamma$  interface is the solute drag. Davis et al. [84] observed the segregation of W at grain boundaries of a 14YWT ODS steel, in its as-produced condition. In the 0.3%  $\text{Y}_2\text{O}_3$  ODS Eurofer, with the dissolution of  $\text{M}_{23}\text{C}_6$  precipitates, located preferentially at grain boundaries (Figure 3.4, Chapter 3) the contents of C, Cr, V and W in the matrix are increased (Figure 4.3). These elements could segregate or form clusters around the grain boundaries/interfaces and exert the so-called drag force,  $F_D$ . When the grain boundary or interface moves, it causes an increase on the energy state of the segregated/clustered solute, which, in turn, will exert a force to pull the grain boundary back [96].

Since coarsening of the oxide nanoparticles likely involves the dissolution of smaller particles and diffusion of its elemental components towards larger ones, the process is not considered to occur instantaneously as the material reaches the annealing temperature of 1400 K. Thus, it is likely that in the beginning of the treatment, the average Zener pinning force exerted in the microstructure is higher than at its later stages. The average Vickers hardness measured for the sample annealed at 1400 K and water quenched is lower than in the reference state (Figure 4.1). The coarse ferrite grains identified in this sample, indicated in Figure 4.1(b), do not present the roughness seen in the reference state (Figure 4.1(c)), and this is an indication of recrystallization. Because of the high cooling rate associated to the process of water quench, it is likely that partial recrystallization occurs at the later stages of the 1400 K annealing treatment, when  $F_z$  is decreased. During cooling inside the furnace, at a lower cooling rate, a higher fraction of recrystallized ferrite formed, as seen in Figure 4.1(a).

#### **4.4.2. Core/shell structure and chemical composition of oxide nanoparticles**

With the APT analysis it was possible to determine the chemical composition of the oxide nanoparticles present in the 0.3%  $\text{Y}_2\text{O}_3$  ODS Eurofer steel. Overall, the particles are formed by a Cr-rich shell and a core enriched in Y, O and V. The presence of a Cr-rich shell

has been reported by several authors, either in ferritic and martensitic ODS steels [79], [80], [89], [91], [92], [93]. Hirata et al. [79] suggested that the Cr-shell is responsible for the high coherency of the oxide nanoparticles with the ferritic matrix, possibly due to the similar BCC Cr and ferrite crystal structure. The high coherency with the matrix is one of the attributes that lower the driving force for particle coarsening, and, thus, is responsible for keeping the particles refined for long periods of time and at high temperatures. However, in martensitic steels, the high temperature phase transition of ferrite into austenite has been suggested to affect this coherency relation of the particle with the matrix [85]. This can partially explain the coarsening observed after annealing at 1400 K. It is interesting to point out that particles with diameter larger than 20 nm seem to be depleted in Cr (Figure 4.5) and to have a thinner or absent Cr-shell (Figure 4.7).

Other ODS Eurofer steel has shown higher thermal stability than the one here studied: oxide particle coarsening to an average size of 25 nm has been reported at temperatures above 1500 K [77]. In other ODS Eurofer steels [80], [89], [92], Ta has been detected in the core of the oxide nanoparticles. Fu et al. [92] reported the formation of finer oxide nanoparticles in ODS Eurofer containing higher Ta and V contents. The same authors [92] have also observed that, when the Ta content is increased, the V once present in the core of oxide nanoparticles is expelled to the Cr-shell and they attribute this behaviour to the higher affinity of Ta with O, in comparison to Cr and V [92]. The absence of Ta in the 0.3%  $Y_2O_3$  ODS Eurofer steel could be related to the lower thermal stability of the oxide nanoparticles, but more investigations are necessary to verify this possible relation.

#### **4.5. Conclusions**

In the present work, the effect of annealing at 1400 K on the microstructure and oxide nanoparticles in a 0.3%  $Y_2O_3$  ODS Eurofer steel was evaluated, using TEM and APT. The results obtained showed that:

- (i) The oxide nanoparticles go through coarsening during the annealing treatment and have their average particle diameter increased from  $3.70 \pm 0.01$  nm (reference state) to  $5.30 \pm 0.04$  nm;
- (ii) With coarsening, the Zener pinning force exerted by the oxide nanoparticles was decreased, leading to the formation of a coarser microstructure, in comparison to the one in the reference state, composed of recrystallized ferrite and martensite;

- (iii) The analysis of the microstructure and Vickers hardness of the material in the reference state, annealed at 1400 K followed by furnace cooling and annealed at 1400 K and water quenched indicates that ferrite retained above  $A_{c3}$  recrystallizes at 1400 K, due to the decrease of the overall Zener pinning force. When the material is cooled inside the furnace, part of the ferrite recrystallizes during cooling;
- (iv) The oxide nanoparticles have a well-known core-shell structure, in which the core is rich in Y, O and V and the shell is enriched in Cr. The average composition of the particles does not change significantly after annealing at 1400 K, except for a slight decrease in the Cr and V contents.

## 5. Thermal stability of the microstructure and characterization of oxide nanoparticles in the ODS 12 Cr steel

Chapter based on publication:

V.S.M. Pereira, S. Wang, T. Morgan, H. Schut, J. Sietsma. “Microstructural evolution and behaviour of deuterium in a ferritic ODS 12 Cr steel annealed at different temperatures”. *Metallurgical and Materials Transactions A*, v. 53, p. 874-892, 2022, doi: 10.1007/s11661-021-06559-0.

### Abstract

In the present work, an ODS 12 Cr steel was characterized using Electron Microscopy techniques, in an as-received condition and after annealing treatments between 773 K and 1573 K. Results show a complex microstructure, with the presence of fine Y-Ti-O nanoparticles dispersed in the matrix. After annealing at 1573 K, the average diameter of Y-Ti-O nanoparticles increases from ~4 nm to ~7 nm and partial recrystallization occurs.

**Keywords:** processing of ODS steels, Y-Ti-O based nanoparticles, Transmission Electron Microscopy

## 5.1. Introduction

ODS ferritic steels have been extensively studied in the past decades due to their potential application as fuel cladding tubes in nuclear fast breeder reactors and on fusion reactor blankets. The Cr contents of 12 weight% or higher promote resistance to corrosion, while the ODS nanoparticles are responsible for the good mechanical performance of the steels at high temperatures and for their resistance to radiation damage. [82], [97]–[105]

Conventional fabrication routes of ODS ferritic steels involve mechanical alloying, consolidation by extrusion or hot isostatic pressing and further thermo-mechanical processing (cycles of cold rolling and annealing, hot rolling, hot forging) [97]–[99], [102]. The microstructure of ODS ferritic steels consolidated via extrusion is composed of large, elongated grains and nanosized grains. In addition, the material has a strong  $\langle 110 \rangle$   $\alpha$ -fibre texture, formed during the extrusion process. The anisotropy in grain morphology and the  $\langle 110 \rangle$   $\alpha$ -fibre texture lead to poor mechanical properties in the transverse direction [98], [104], [65]. In conventional steels, grain morphology and texture can be altered during the phase transformation of ferrite to austenite or during recrystallization. However, Cr-rich ODS ferritic steels cannot be austenitised and the  $\langle 110 \rangle$   $\alpha$ -fibre texture is difficult to be removed, due to its inherent low driving force for recrystallization [106]. Recently, other fabrication routes which do not involve extrusion or hot isostatic pressing have been developed and promising results were reported [82], [104]. Moghadasi et al. [82] produced an ODS ferritic alloy with nanometric  $\text{Y}_2\text{TiO}_5$  particles dispersed in the matrix via a vacuum casting route and Kumar et al. [104] obtained an ODS 18 Cr steel using powder forging as consolidation method. In [104], the final forged product exhibited isotropic morphology and crystallography and, consequently, isotropic mechanical properties.

Regardless of the fabrication route used, an important aspect of alloy design, common to ODS ferritic steels, is the addition of titanium. During processing, the presence of Ti dissolved in the pre-alloy ferritic powder or added to the powder mixture as  $\text{TiO}_2$ , leads to complex Y-Ti-O particles with average particle size ranging from 3 to 10 nm. Depending on the processing parameters, the oxide nanoparticles can form with different stoichiometric compositions and crystal structures, like cubic  $\text{Y}_2\text{Ti}_2\text{O}_7$ , orthorhombic or hexagonal  $\text{Y}_2\text{TiO}_5$ , orthorhombic  $\text{YTiO}_3$  [97], [100], [102], [82], [107]. Additionally, it has been reported by different authors that Y-Ti-O nanoparticles are coherent or semi-coherent with the ferritic matrix [100], [82], [108]. This type of coherency relation with the matrix has been correlated to the slow coarsening rate of the Y-Ti-O particles at high temperatures: the interfacial energy



of a coherent or semi-coherent particle is low, resulting in a low driving force for coarsening [82], [108]. The slow diffusion of Y in ferrite also contributes to the low coarsening rate. Hence, the Y-Ti-O particles remain refined at temperatures as high as 1473-1573 K and, consequently, the microstructural stability of the material is maintained.

In this chapter, the microstructure and oxide nanoparticles present in a ferritic ODS 12 Cr steel are characterized, after 1 h annealing treatments at different temperatures. The results are compared to the ODS Eurofer steel studied in Chapters 3 and 4.

## 5.2. Experimental

### 5.2.1. Material

The material was fabricated according to a traditional route used for ODS 12 Cr ferritic steels, which consisted of mechanical alloying, hot extrusion and thermo-mechanical post-consolidation treatments [109]. Table 5.1 presents the chemical composition of the steel, determined with X-Ray Fluorescence (heavy elements) and Combustion Analysis (C and S).

**Table 5. 1.** Chemical composition of the 0.3 %  $Y_2O_3$  ODS 12 Cr steel, in weight percentage. The O content was not determined experimentally, instead, it was calculated assuming that all O present in the steel was in  $Y_2O_3$ .

ODS 12 Cr	Fe	C	Cr	W	Ti	Zn	Y	O*	Si	S	Al
	85.08	0.03	12.29	1.72	0.30	0.04	0.14	0.05	0.17	0.04	0.13

The material was received in a bar form, with thickness of 6 mm. Samples with dimensions of 15 x 15 x 1 mm<sup>3</sup> were taken from arbitrary positions along the thickness of the bar and isothermally treated in a vacuum furnace at 773, 1273, 1373, 1473 and 1573 K for 1 h. *A priori* examination of the steel bar using Optical Microscopy showed an overall homogeneous microstructure along the thickness. All samples were cooled inside the furnace, by switching off the power supply, under exponential cooling with an average cooling rate of 0.5 K.s<sup>-1</sup>.

Although it is well known that steels containing Cr contents of 12% or higher are ferritic, dilatometry tests were carried out in a Bahr DIL805A/D to confirm that the material does not go through the  $\alpha/\gamma$  phase transformation during heating. The samples were heated to 1273 K, at a heating rate of 10 K.s<sup>-1</sup>, with a holding time of 3 min, and cooled down to room temperature at different cooling rates, varying from 0.25 K.s<sup>-1</sup> to 60 K.s<sup>-1</sup>. Figure 5.1 contains a representative dilatometry curve, which does not present any inflection characteristic of phase transitions, confirming that the steel is fully ferritic throughout the heat treatments.

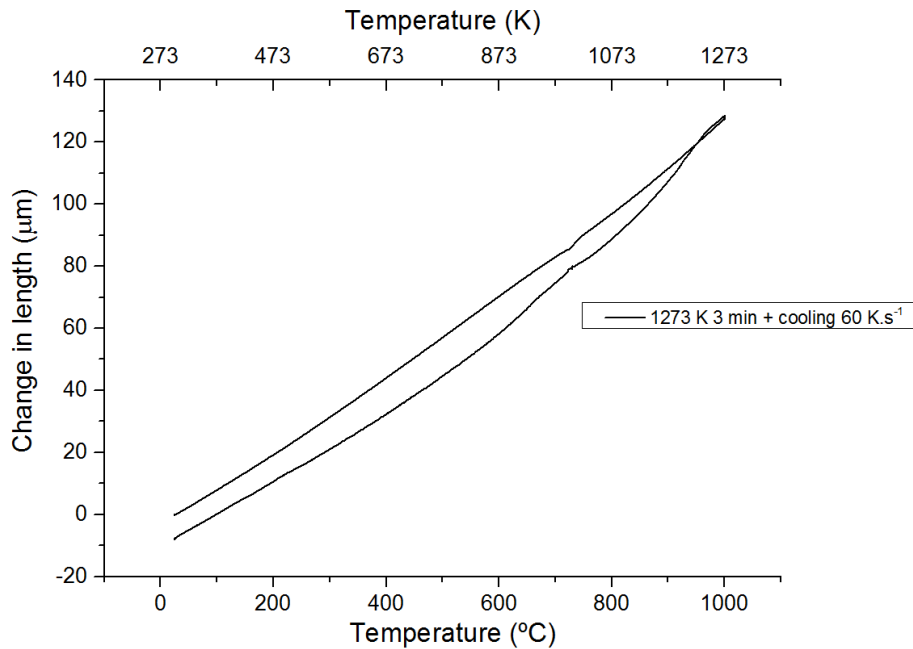


**Figure 5. 1.** Representative dilatometry curve obtained for the ODS 12 Cr after heating until 1273 K at a rate of  $10 \text{ K.s}^{-1}$ , holding time of 3 min and cooling to room temperature at  $60 \text{ K.s}^{-1}$ .

### 5.2.2. Methods

The microstructures of the as-received and annealed conditions were characterized with Scanning Electron Microscopy (*SEM*), Energy Dispersive X-Ray Spectroscopy (*EDS*) and Electron Backscatter Diffraction (*EBSD*). The basic sample preparation steps included grinding with SiC papers of different grits (320, 800, 1200 and 2000), polishing with diamond suspensions of  $3 \mu\text{m}$  (6 to 10 min) and  $1 \mu\text{m}$  (20 min) and final polishing with  $\text{SiO}_2$  suspension of  $0.04 \mu\text{m}$  (40 min). For SEM and EDS analyses, the samples were electrolytically etched in a 10 % aqueous solution of ammonium persulfate for 1.5 min and at 6 V potential. The used etchant highlights second-phase precipitates containing Ti, Cr and W. The Scanning Electron Microscope used was a JEOL 6500FD equipped with a Thermo Fisher NSS EDS and Nordlys II EBSD detectors. The EBSD measurements were performed using a step size of  $0.1 \mu\text{m}$ , with the Oxford *hkl* Channel 5 acquisition software. The data was post-processed with the software EDAX-TSL OIM Data Collections 7 and, prior to analysis, data clean-up was made according to the following steps: 1<sup>st</sup>) clean-up by Grain CI Standardization, with tolerance of 5.0, minimum size of 2 and multi-row 1 and 2<sup>nd</sup>) clean-up by Neighbour CI Correlation, with minimum CI equal to 0.10.

The ODS nanoparticles dispersed in the matrix of the steel in the as-received condition and annealed at 1573 K were characterized using a JEM-2200FS Transmission Electron

Microscope (TEM) in the Department of Metallurgy at Gent University, Belgium. Sample preparation involved the following steps: (1) mechanical grinding of plates with initial dimensions of 10 x 10 x 0.5 mm<sup>3</sup> until a thickness of 100 μm was reached; (2) cutting of disks with 3 mm in diameter and (3) electropolishing of the disks in solution of 4% perchloric acid and 96% ethanol, in order to further reduce the thickness of the disks and to make them transparent to the electron beam.

The volume fraction of second phase constituents was determined using micrographs obtained with the SEM and the image analysis software *ImageJ*, according to the procedure described in the ASTM E1245-03 standard [70]. The size distribution of oxide nanoparticles was also estimated using the software *ImageJ*, but in this case the measurements were not automatized, due to limited contrast between particles and the matrix in the electron micrographs. For the size estimation, the longest distance within a particle boundary observed in 2D was taken as the average length of the particle.

In order to have an indication of the effect of the heat treatments on mechanical properties, Vickers hardness measurements were made on the as-received and annealed samples. The applied load was 0.3 kgf using a Struers Durascan 70 microhardness device.

### 5.3. Results and Discussion

#### 5.3.1. Characterization of the microstructure after different annealing treatments

Figure 5.2 shows isopleths of the Fe-Cr equilibrium diagram for the ODS 12 Cr steel, calculated with Thermo-Calc v.2020a. For the Thermo-Calc calculations, the database used was TCFE10: “Steels/Fe alloys” and a simplified chemical composition of the ODS 12 Cr steel was inserted, in weight%: Fe-0.03C-12Cr-1.7W-0.3Ti-0.144Y-0.05O. The Laves phase is a complex intermetallic that can form in the material after long exposures, of the order of thousands of hours, at intermediate temperatures [110]. Therefore, Laves-Phase is not expected to be present in the as-received and annealed conditions of the ODS 12 Cr steel. TiO<sub>2</sub> is an oxide which could be present in the material, but in practice is only found in ODS steels containing a minimum Ti content of 0.5 weight % [101], [111]. The Y-O particle indicated in Figure 5.2 corresponds to Y<sub>2</sub>O<sub>3</sub>. Thermo-Calc assumes that the oxide particles keep their original chemical composition (Y<sub>2</sub>O<sub>3</sub>) at all temperature ranges. Y<sub>2</sub>O<sub>3</sub> can only be completely dissolved in steels during mechanical alloying and re-precipitates in the material during further heating stages, but with different chemical composition. The chemical composition of the re-

precipitated Y-O based nanoparticles depends on the alloying elements present in the steel. For the ODS 12 Cr steel, Ti is expected in the composition of its oxide nanoparticles.

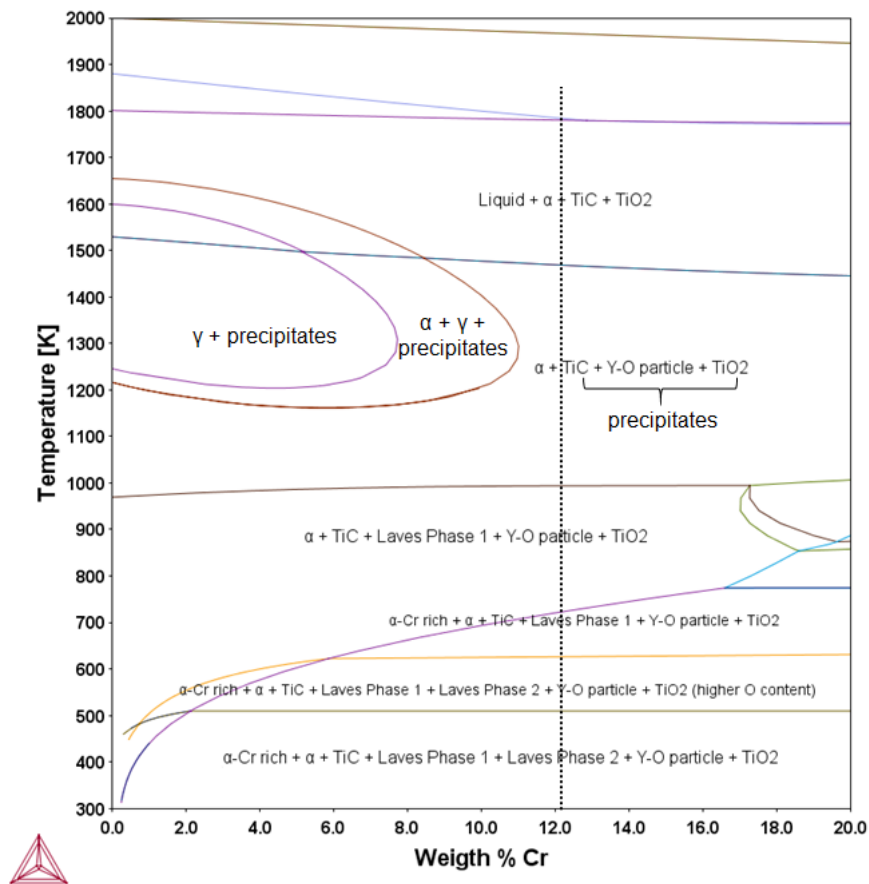


**Figure 5. 2.** Isopleths of Fe-Cr equilibrium diagram calculated with Thermo-Calc v. 2020a for the ODS 12 Cr steel.

Figures 5.3(a) and 5.3(b) present low-magnification, backscattered electrons (BSE) micrographs of non-etched samples in the as-received condition and after annealing at 1573 K. The material contains pores formed during the fabrication process. Qualitatively, no increase in porosity and pore average size was observed with the increase annealing temperature for the 1 h treatments. However, in [112] an increase in the amount of pores and pore average size was reported for a very similar ODS steel annealed at 1573 K and 1673 K for 12 h and 24 h. Figures 5.3(c) and 5.3(d) show higher magnification, secondary electrons (SE) micrographs of pores present in the ODS 12 Cr steel, annealed at 1573 K for 1 h. Particles of a few hundreds of nanometres in size and spherical/cuboidal shape are found at the internal surfaces and interfaces of the pores. Samples in the as-received condition and annealed at lower temperatures also exhibit particles with these characteristics in some of their pores. In Figure 5.3(c), red arrows

indicate groups of particles that likely have coalesced, with original particle boundaries still visible.

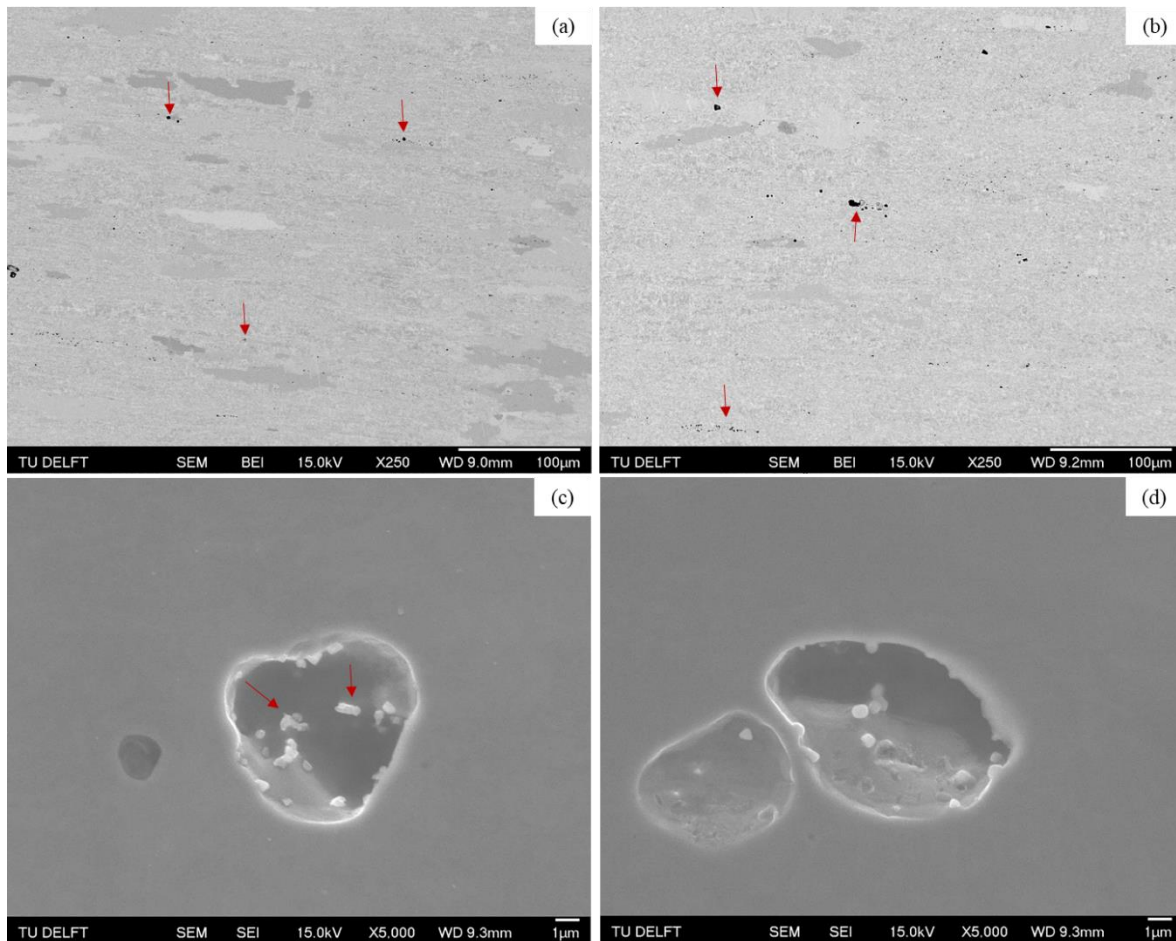


**Figure 5. 3.** Backscatter and Secondary Electrons micrographs of non-etched ODS 12 Cr steel in the (a) as-received condition, (b) annealed at 1573 K for 1 h, with red arrows indicating pores. In (c) and (d) a detailed view of pores, which contain particles (light-grey) at their internal surfaces. The red arrows in (c) indicate groups of coalescing particles.

The estimated average diameter of the light-grey particles seen in Figures 5.3(c) and 5.3(d) is  $0.5 \pm 0.1 \mu\text{m}$ , the groups of particles indicated by the red arrows were counted separately and their average length is  $1.0 \pm 0.1 \mu\text{m}$ . EDS analyses were made on 27 of these light-grey particles encountered in the samples annealed at 1473 K and 1573 K. All results qualitatively indicate the presence of Y, Ti and O in the particles. The EDS analyses of particles are considered qualitative due to (1) the size of the interaction volume of the electron beam with the material, which is larger than the analysed particles and (2) the fact that the particles are located inside pores. When the interaction volume of the electron beam with the material is larger than the particle size, the chemical composition of the matrix is also measured, influencing the resulting values. The curvature of the internal surfaces of pores on which the

particles are located can also have a significant impact on electron scattering and also on the X-Ray intensities measured, which can diverge considerably from their true chemical composition [113]. The emitted X-Rays need to travel a certain length to reach the EDS detector and, when originating from regions of complex topology, they can be re-absorbed by the material [113]. A more precise determination of their chemical composition was made with the EDS system coupled to the Transmission Electron Microscope and the results are given in Section 5.3.2.

Several authors [112], [114], [115], [116] discussed the incorporation of Ar in ODS steels during mechanical alloying as the starting point for pore formation. In our discussion, we consider the concepts and evidence published by these authors, in order to clarify how pores can be produced in ODS steels and to explain the presence of coarse Y-Ti-O particles at internal surfaces of pores in our ODS 12 Cr steel. In [116], micrometre-sized pores were observed in a 0.5% Y<sub>2</sub>O<sub>3</sub>-ODS 20 Cr alloy milled in hydrogen atmosphere, instead of Ar. The authors argue that pore formation is intrinsic to the mechanical alloying (MA) process, as they have found isolated pores in some of the MA-powder particles, and that inert gas uptake during MA increases porosity in ODS steels [116]. So, besides dissolution of Y<sub>2</sub>O<sub>3</sub> into Y and O, residual concentrations of Ar (or other gas) enter the metallic structure of the mechanically alloyed powders. Hence, at this stage all elements are in solid solution within the Fe matrix and some pores might be already present in MA-powder particles. When the MA-powders are consolidated at high temperature (1100 K and above), either by hot isostatic pressing or hot extrusion, the oxide nanoparticles re-precipitate and the Ar atoms can

- (i) diffuse through the lattice,
- (ii) recombine with other Ar atoms and form bubbles, which can be located at grain boundaries or interfaces of second-phase particles, like carbides [112], [115],
- (iii) stabilize vacancies either thermally formed [115] and/or induced by deformation, in the case of consolidation via hot extrusion and
- (iv) accommodate and agglomerate at interfaces of oxide nanoparticles [114].

Klimiankou et al. [114] have found nano-cavities filled with Ar at the interfaces of Y<sub>2</sub>Ti<sub>2</sub>O<sub>7</sub> nanoparticles in a 9 Cr ODS steel. In many cases, the authors observed multiple Ar nano-cavities trapped at the interface of a single oxide nanoparticle [114]. Ortega et al. [115] suggested that Ar atoms enable the nucleation of vacancy clusters in both non-ODS and ODS Eurofer steels. They provided evidence that Ar-vacancy clusters located in the matrix of steels

and trapped at interfaces of Y-O nanoparticles are able to withstand high annealing temperatures and grow, forming larger defects (Ar-filled voids). Now, going back to the mechanism of pore formation and keeping in mind the results of [114] and [115], we can infer that during thermomechanical treatment of the consolidated ODS 12 Cr steel, the initially small Ar bubbles and Ar-vacancy clusters, located either in the matrix or at interfaces of Y-Ti-O nanoparticles, are able to grow via Ostwald ripening and reach the micrometric dimensions observed in Figure 5.3. When pores are being formed at regions of the material with higher local density of oxide nanoparticles, the combination of (a) small inter-particle distance, (b) high temperature (1400 K and above) and (c) diffusion-assisted creation of surfaces inside newly-grown pores, results in the local coarsening or coalescence of Y-Ti-O nanoparticles.

Figure 5.4 presents SE and BSE micrographs of the sample annealed at 773 K, etched with ammonium persulfate, which reveals micrometric precipitates. The black regions in Figure 5.4(b) correspond to pores. The precipitates are not homogeneously distributed throughout the sample and are aligned along the extrusion direction. In all analysed samples, the precipitates have the same morphology and spatial distribution in the matrix. The chemical composition of the precipitates was determined with EDS and representative results are given Figures 5.4(c) and 5.4(d). For all annealing conditions, the precipitates show a high EDS-peak of Ti, and C is always detected. Peaks of Cr and Fe are also observed and, for precipitates smaller than 1  $\mu\text{m}$ , their contents are close to the matrix composition (effect of size of interaction volume of the electron beam). Small contents of W ( $\sim 2$  weight%) are detected in some of the particles. Hence, the precipitates correspond to TiC, in agreement with Thermo-Calc predictions. The equilibrium composition given by Thermo-Calc shows that the TiC should be formed by, in weight %, 53Ti-46C-2Cr-2Fe-2W.

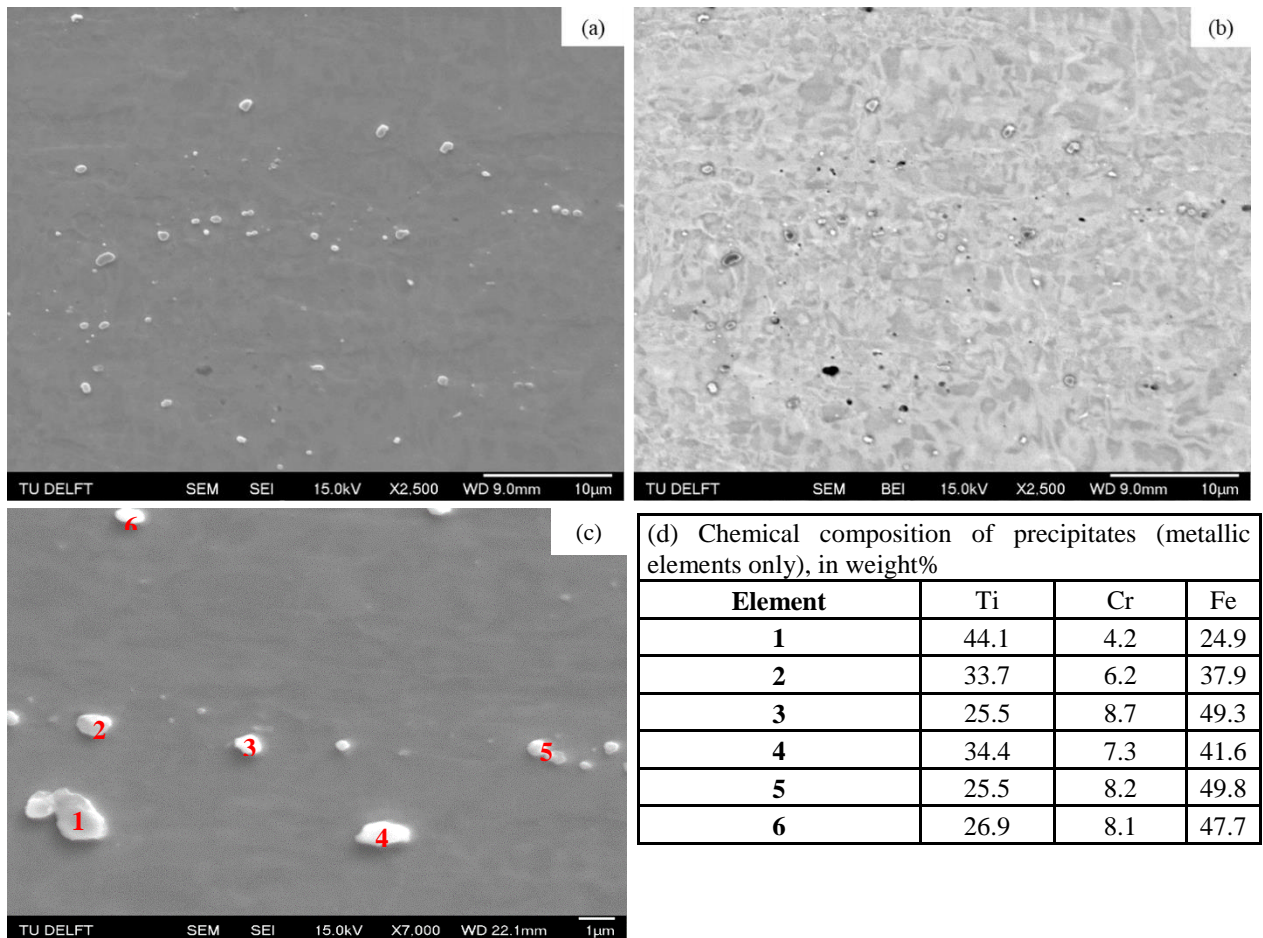


**Figure 5.4** (a) SE and (b) correspondent BSE micrographs of sample annealed at 773 K for 1 h, the red arrows indicate micrometric precipitates. (c) SE micrograph of precipitates present in the sample annealed at 1273 K and (d) contents of the main metallic elements present in the precipitates, determined with EDS.

The volume fraction of TiC vs annealing temperature, determined with the software *ImageJ*, can be seen in Figure 5.5, along with the equilibrium molar fraction of TiC predicted with Thermo-Calc. The standard deviations associated to the measured average volume fractions are high, reflecting the heterogeneity of the precipitate distribution in the material. The average diameter of precipitates varies from 0.3 to 3  $\mu\text{m}$ .



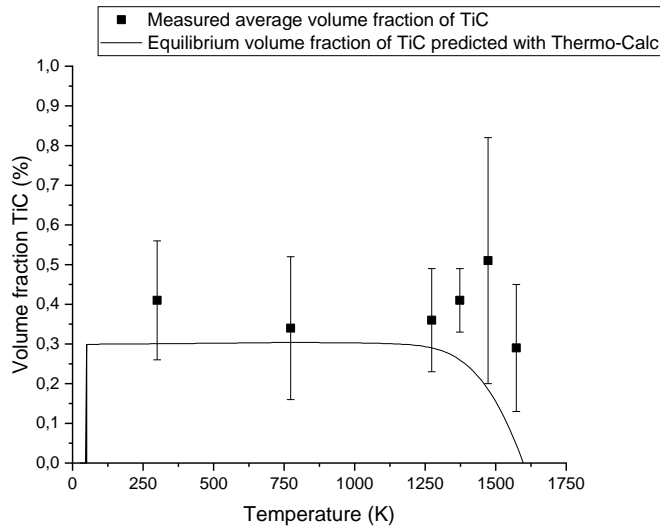


**Figure 5. 5.** Average volume fraction of TiC determined with *ImageJ* vs annealing temperature; the line corresponds to the equilibrium molar fraction of TiC predicted with Thermo-Calc v. 2020a, composition and database used: Fe-0.03C-12Cr-1.7W-0.3Ti-0.144Y-0.05O and TCFE10: Steels/Fe alloys.

In general, the matrices of ODS steels are composed of micrometric grains surrounded by nanometric ones and, when chemically etched for SEM inspection, the regions containing nanometric grains are completely corroded, preventing a clear observation of grain boundaries. Hence, the use of orientation image maps (OIM) is a suitable option for the analysis of nanometric grains, since it does not require etching of samples. To adequately observe the ferritic matrix of the ODS 12 Cr steel, samples in the as-received state and annealed at 773 K, 1273 K, 1373 K, 1473 K and 1573 K were analysed with EBSD. Representative OIM are displayed in Figure 5.6, in which the grey scale images correspond to Image Quality (IQ) maps and the coloured ones are Inverse Pole Figure (IPF) maps, obtained along the normal direction. The elongation direction of the grains corresponds to the extrusion direction (indicated in the Figure 5.6 as ED). Note that Figures 5.6(a-d) and Figures 5.6(e-h) have different sample orientations inside the electron microscope. Figure 5.7 shows the grain size distributions of each analysed sample, obtained by EBSD. The values of the  $x$ -axis correspond to the centre of the bins, the bin size is 1  $\mu\text{m}$  (TSL OIM software determines the lower boundary of the first size class as 0.15  $\mu\text{m}$ ).

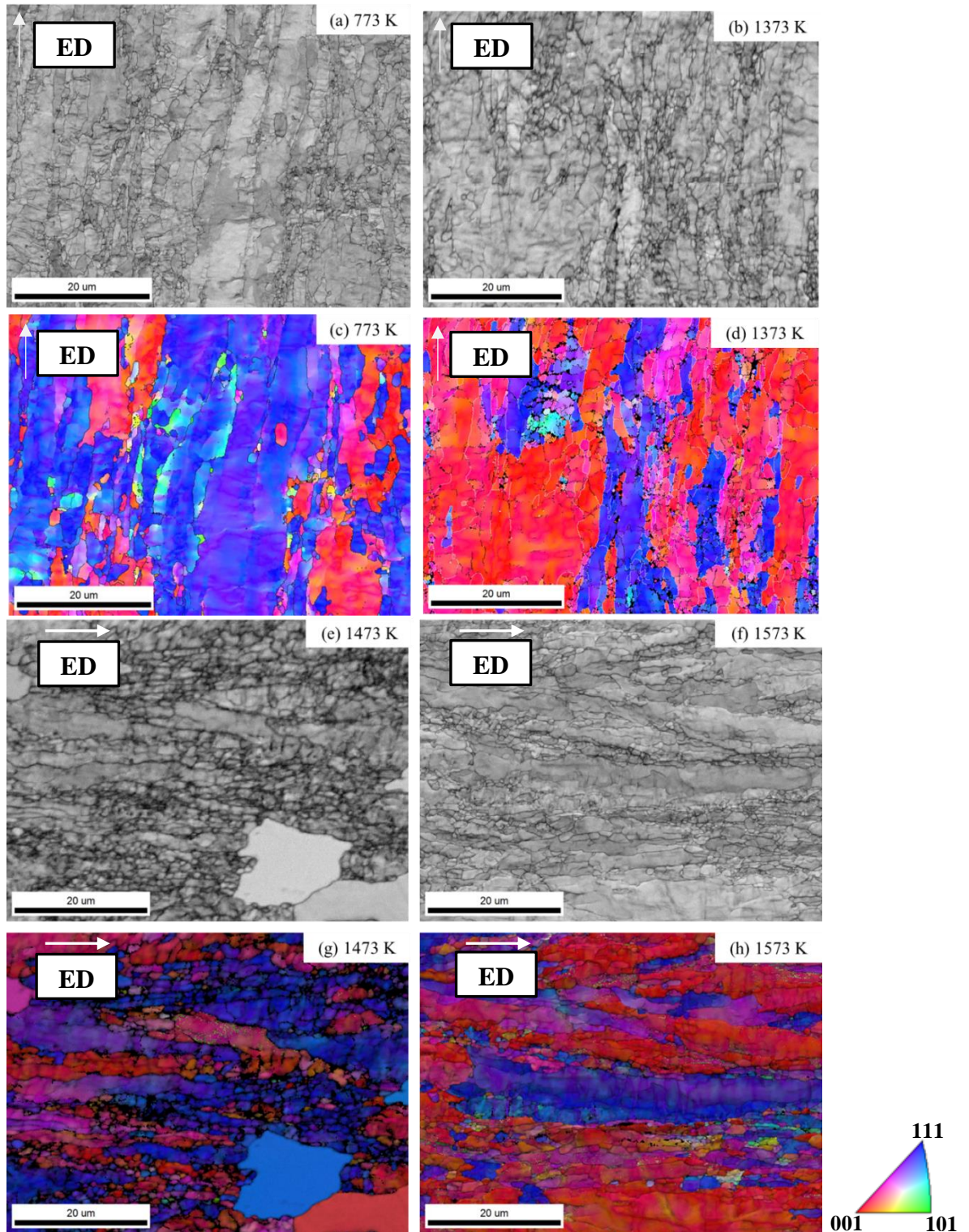


**Figure 5. 6.** Orientation image maps obtained with EBSD for the ODS 12 Cr steel after 1 h annealing at 773 K, 1373 K, 1473 K and 1573 K. (a), (b), (e) and (f) are Image Quality maps; (c), (d), (g) and (h) are Inverse Pole Figure maps.

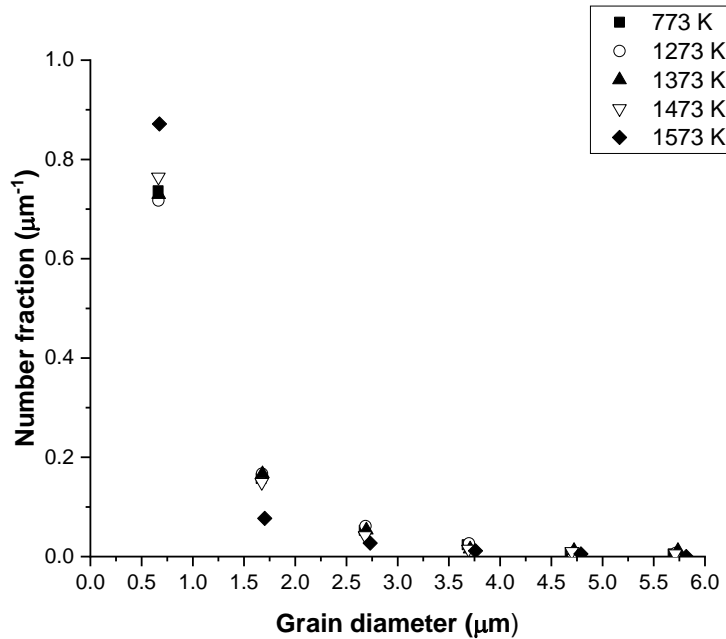


**Figure 5. 7.** Grain size distributions obtained with EBSD for the ODS 12 Cr steel annealed at different temperatures for 1 h.

Unlike the ODS Eurofer steel studied in [117], the present material does not go through any phase transformation or substantial recrystallization. Thus, the microstructures in the as-received and annealed conditions are similar, composed of grains with 4 to 30  $\mu\text{m}$  length and smaller ones with sizes of 0.2 to 4  $\mu\text{m}$ . The IPF maps in Figure 5.6 qualitatively show that, for all conditions, the grains have a preferential orientation of  $\langle 001 \rangle$  and  $\langle 111 \rangle$  directions, which is in agreement with observations made on other ODS 12 Cr ferritic steels consolidated via hot extrusion [98], [102]. In [112] the authors detected substantial recrystallization only after 24 h of annealing at 1573 K or 12 h at 1673 K. The grain size distribution of Figure 5.7 displays information with sufficient statistical significance only of grains with sizes ranging between 0.15 and 6  $\mu\text{m}$  – the number of larger grains is too small to determine the size distribution.

Figure 5.8 shows the Vickers hardness values of the ODS 12 Cr steel in all the analysed conditions, along with data obtained previously for the ODS Eurofer steel in [117]. The latter presents hardness alterations that are in accordance with the microstructural processes taking place in the material (phase transformation and recrystallization), whereas the ODS 12 Cr steel exhibits constant Vickers hardness in almost the whole temperature range, only going through a moderate decrease in hardness after annealing at 1573 K for 1 h.

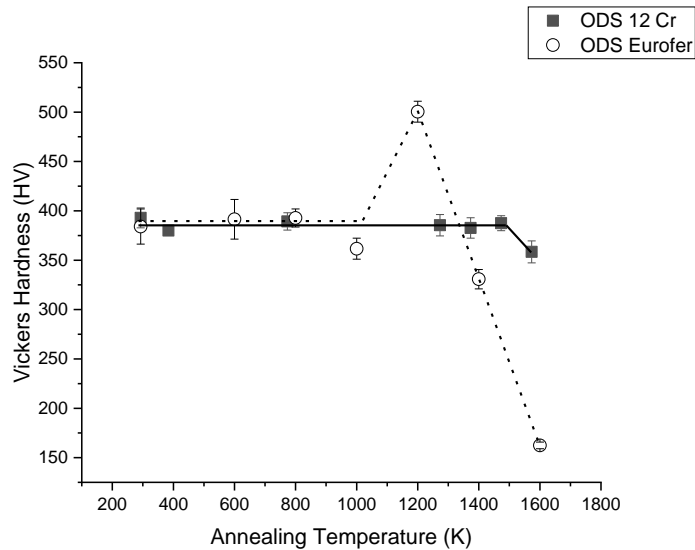


**Figure 5. 8.** Vickers hardness of the ODS 12 Cr annealed for 1 h at different temperatures, in comparison to the ODS Eurofer studied in [117].

The results given in Figures 5.6-5.8 depict the high thermal stability of the ODS 12 Cr steel, which is in great part attributed to the addition of Ti in the material, known for refining the Y-O nanoparticles [97], [109]. Thus, Y-Ti-O based nanoparticles should remain refined even at temperatures as high as 1573 K and effectively prevent grain growth, due to a strong Zener pinning effect. Yet, the moderate decrease in Vickers hardness after annealing at 1573 K signalizes the occurrence of a slight degree of softening in the material, not detectable in our microstructural analysis with SEM and EBSD. In the next section we investigate the evolution of the oxide nanoparticles with temperature in more detail.

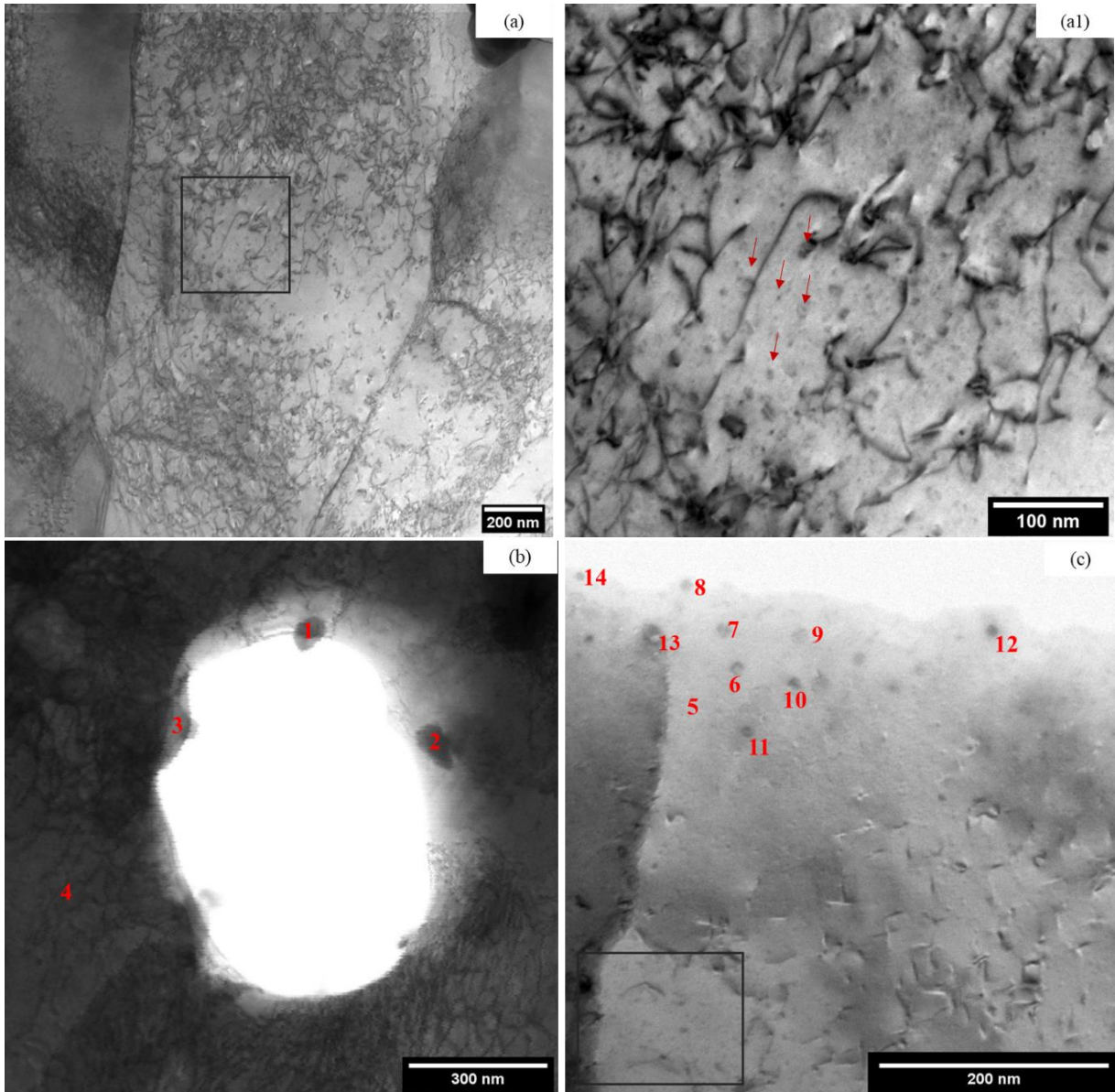
### 5.3.2. Characterization of oxide nanoparticles in the as-received condition and after annealing at 1573 K

In order to characterize the oxide nanoparticles present in the steel and investigate if they are altered after exposure to 1573 K, samples in this condition and in the as-received state were analysed with Transmission Electron Microscopy (TEM).

Figure 5.9 presents bright-field micrographs of the material in the as-received condition, obtained in the STEM mode, and results of EDS measurements made on different features of the microstructure. Qualitatively, the material presents an expected high dislocation density, common in ODS steels due to severe deformation imposed during mechanical alloying and, in the case of the ODS 12 Cr steel, hot extrusion and other mechanical post-consolidation treatments. Figure 5.9(a1) corresponds to a detail of the indicated region in Figure 5.9(a).

Nanosized particles are seen dispersed in the matrix and some of them are pinning dislocations. Figure 5.9(b) shows a pore present in the as-received microstructure, which contains particles of 70 to 200 nm located at its interface. The results of EDS measurements given in Figure 5.9(d) show that the particles identified as 1 and 2 are Y-Ti-O based and particle 3 is TiC. These results confirm the observations made with SEM presented in Figure 5.3 and discussed in section 5.3.1, of local coarsening of Y-Ti-O particles, due to enhanced diffusion at the internal surfaces and interfaces of pores. In Figure 5.9(c), with the exception of point 5 marked in the ferritic matrix of the steel, all points correspond to Y-Ti-O based nanoparticles, with an estimated average particle size of 10 nm. Additionally, in Figure 5.9(c) an outlined region containing Y-Ti-O particles with sizes ranging from 2 to 5 nm is displayed. The direct quantification of light elements like oxygen using EDS, whether in TEM or SEM, is complex. The X-Ray peaks of oxygen and other light elements are located in the low-energy range of the EDS spectrum, subjected to the interference of the background radiation and of L, M and N X-Rays emitted by heavier elements [113]. In the particular case of Cr-containing steels, the presence of Cr interferes with the detection of O, due to peaks of Cr-L $\alpha$  with energy of 0.573 keV being close to the O-K $\alpha$  0.525 keV. Oxygen was detected in the present EDS analyses, but for the mentioned reasons the O concentrations are not displayed in Figure 5.9(d).

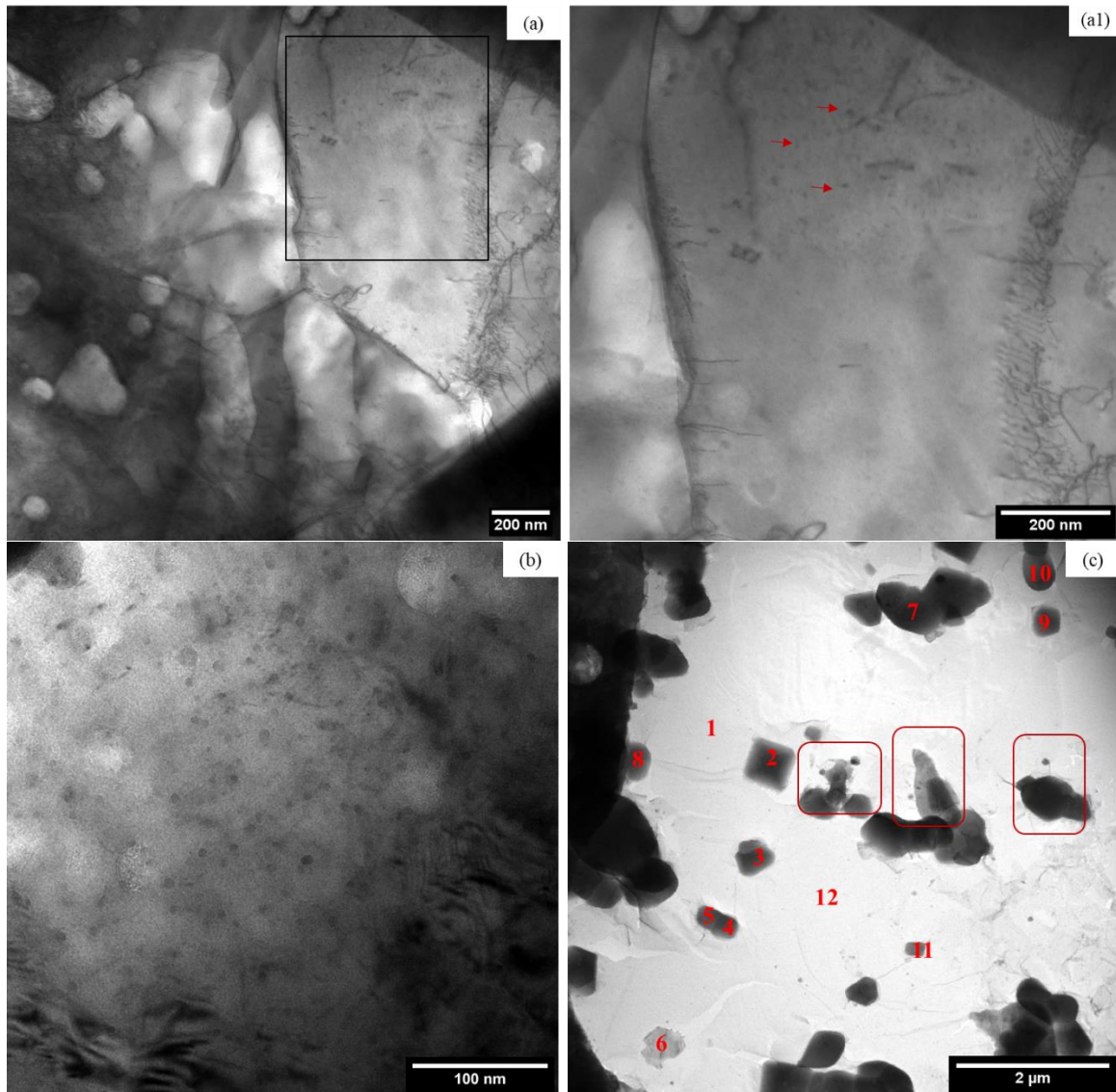
Figure 5.10 contains bright-field micrographs of the sample annealed at 1573 K for 1 h, showing Y-Ti-O nanoparticles (Figure 5.10(a) and 5.10(b)), sub-micrometric particles inside a ferrite grain (Figure 5.10(c)) and results of EDS analysis (Figure 5.10(d)). The dislocation-free ferrite grain seen in Figure 5.10(c), which contains numerous sub-micrometric particles, is an indication that partial recrystallization is taking place in the material. Thus, the overall dislocation density in the annealed sample can be expected to be slightly lower than in the as-received condition. EDS analyses of the sub-micrometric particles in Figure 5.10(c) show that most of them are Y-Ti-O based. Still in Figure 5.10(c), red squares are indicating groups of particles undergoing coarsening: larger particles are growing, likely due to dissolution of smaller ones. Some of the coarse particles had a cuboidal shape, which is the most stable geometry of particles that are incoherent with the matrix. However, it is not clear why this pronounced coarsening occurs only locally in the material. A slight degree of recrystallization, accompanied by a decrease in dislocation density and local coarsening of Y-Ti-O particles to sub-micrometric dimensions explains the moderate decrease in Vickers hardness measured after annealing at 1573 K for 1 h.



(d) Characteristics and chemical composition of point analysis indicated in (b) and (c)

Type of particle and estimated size	Main metallic elements, weight %			
	Ti	Cr	Fe	Y
1. Y-Ti-O particle, 72 nm	15.2	4.5	26.9	40.8
2. Y-Ti-O particle, 102 nm	5.0	9.9	60.5	18.8
3. TiC, 208 nm	71.2	4.3	16.2	4.4
4. Ferritic Matrix	0.1	13.7	86.0	0
5. Ferritic Matrix	0.2	14.4	78.7	0
6-14. Y-Ti-O particles, average of estimated sizes $10 \pm 3$ nm	Average weight % $\pm$ standard deviation			
	<b><math>9 \pm 4</math></b>	<b><math>9 \pm 2</math></b>	<b><math>48 \pm 15</math></b>	<b><math>29 \pm 12</math></b>

**Figure 5. 9.** (a-c) Bright-field micrographs of the ODS 12 Cr steel in the as-received condition, (d) results of chemical analysis of points indicated in (b) and (c), along with particle size estimated with *ImageJ*, considering the particle size equal to the longest distances between the particles extremities.



(d) Characteristics and chemical composition of point analysis indicated in (c)

Type of particle and estimated size	Main elements, weight %			
	Ti	Cr	Fe	Y
1. Matrix	0.9	7.5	88.9	2.4
6. Matrix	0.8	11.0	87.9	0.2
8. Particle rich in Ti and Y	35.3	5.2	33.1	26.4
12. Matrix	2.4	11.4	83.1	3.1
2-5, 7, 9-11. Y-Ti-O coarse particles, estimated average size $490 \pm 220$ nm	Average weight % $\pm$ standard deviation			
	$19.1 \pm 1.5$	$2.5 \pm 0.3$	$17.8 \pm 1.3$	$60.5 \pm 1.1$

**Figure 5.10.** (a-c) Bright-field micrographs of the ODS 12 Cr steel annealed at 1573 K for 1 h and (d) results of chemical analysis of points indicated in (c), along with particle size estimated with *ImageJ*, considering the particle size equal to the longest particle length.

Finally, the size distributions of the oxide nanoparticles present in the as-received and annealed conditions were calculated using bright-field images and the results are displayed in Figure 5.10. The sub-micrometric particles, like the ones located at pores (Figure 5.9(b)) or the

ones seen in Figure 5.10(c), were not taken into account. A total of 470 particles per condition were measured and, given that all had approximately spherical morphologies, the particle size was estimated to be the particle diameter.

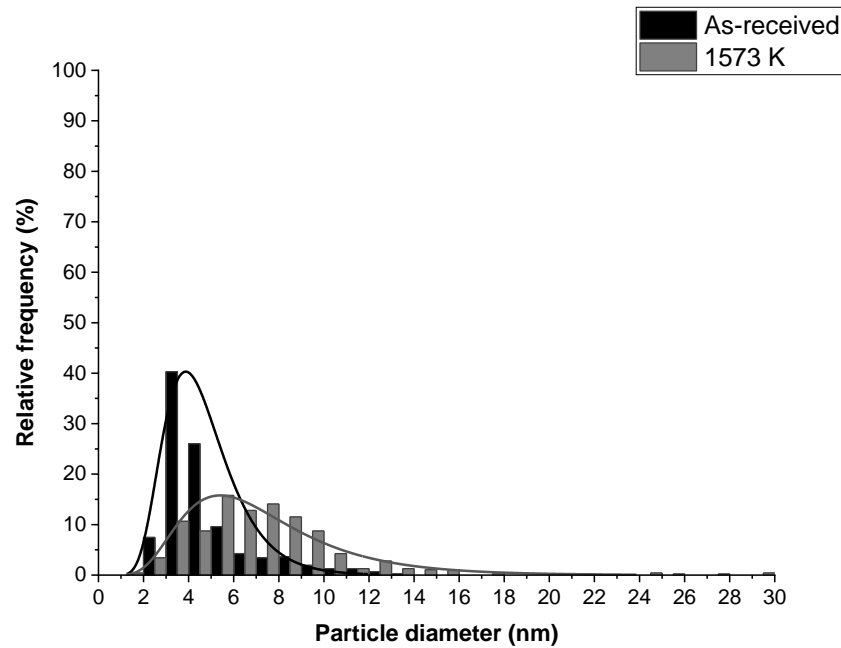


**Figure 5. 11.** Size distribution of Y-Ti-O particles present in the ODS 12 Cr steel on its as-received condition and after annealing at 1573 K for 1 h.

The size distributions in Figure 5.11 show a clear coarsening of oxide nanoparticles during annealing at 1573 K for 1 h. In the as-received condition, the average diameter of the particles is  $3.87 \pm 0.04$  nm and after the annealing treatment the size distribution has become broader, with a pronounced increase in particles with diameter ranging from 5 nm to 10 nm and an average diameter of  $6.9 \pm 0.2$  nm. The particle sizes measured in the as-received sample are in agreement with observations made on other ODS ferritic steels that did not undergo high temperature annealing [100], [102]. Other authors have also observed the coarsening of Y-Ti-O based nanoparticles after 1 h annealing at temperatures above 1500 K [118], [119], [120]. Dou et al. [100] measured the coherence of orthorhombic/hexagonal  $Y_2TiO_5$  nanoparticles in ODS ferritic steels and found that particles with a diameter smaller than 4.5 nm are coherent with the ferritic matrix, while particles with diameters between 4.5 and 10 nm are semi-coherent. Interestingly, the authors [100] also found that particles with a diameter larger than 10 nm are predominantly incoherent with the matrix. Thus, considering the tendency of Y-Ti-O nanoparticle coarsening shown in Figure 5.11, it can be assumed that the ODS 12 Cr steel annealed at 1573 K for 1 h has a higher density of semi-coherent and incoherent nanoparticles than the as-received condition.



## 5.4. Conclusions

The microstructural characterization of the ODS 12 Cr steel after 1 h annealing treatments at different temperatures allow the following conclusions:

- (i) The microstructure of the ODS 12 Cr steel is complex, formed by a variety of highly thermally stable components: a ferritic matrix composed of nanosized and micrometric grains, which has an intrinsic resistance to recrystallization due to its texture; incoherent TiC particles, even present after annealing at 1573 K for 1 h and pores containing coarse Y-Ti-O based particles, likely formed due to Ar retention during mechanical alloying;
- (ii) Only after annealing at 1573 K for 1 h a moderate decrease in Vickers hardness was observed in the ODS 12 Cr steel, from ~ 380 HV to ~ 350 HV. It was also possible to detect with TEM an increase in average diameter of Y-Ti-O nanoparticles from ~4 nm to ~7 nm, which was associated to partial recrystallization of the material and to the decrease in hardness.
- (iii) In comparison to the ODS Eurofer steel studied in Chapter 3, the microstructural stability of the ODS 12 Cr steel is highly superior, confirming the beneficial effect of Ti addition on oxide nanoparticle refinement and stability.

## **Part II**

### **Analysis of defects in ODS steels: thermal evolution and oxide nanoparticle interaction**

## 6. Thermal evolution of defects in ODS steels studied with Positron Annihilation Doppler Broadening

Chapter based on publication:

V. S. M. Pereira, H. Schut, and J. Sietsma, “A study of the microstructural stability and defect evolution in an ODS Eurofer steel by means of Electron Microscopy and Positron Annihilation Spectroscopy,” *J. Nucl. Mater.*, vol. 540, 2020, doi: 10.1016/j.jnucmat.2020.152398.

### Abstract

In this Chapter, the 0.3%  $Y_2O_3$  ODS Eurofer and ODS 12 Cr steels in the reference state and annealed at temperatures between 600 and 1600 K, characterized in Chapters 3 to 5, were analysed with Positron Annihilation Doppler Broadening (PADB). The objective was to investigate the thermal evolution of defects and their interaction with the Y-O nanoparticles. Non-ODS alloys were also measured, in order to evaluate the contribution of defects intrinsic to the microstructure (grain boundaries, interfaces of precipitates, dislocations) to the PADB results. For the 0.3%  $Y_2O_3$  ODS Eurofer steel, PADB results indicate that annealing up to 1200 K leads to an overall decrease in defect concentration, mainly due to recovery of dislocations. The ODS 12 Cr steel shows constant values of  $S$  and  $W$  up to 1473 K, suggesting that the concentration of defects is also constant. After annealing of the 0.3%  $Y_2O_3$  ODS Eurofer at 1400 K and 1600 K, the  $S$  and  $W$  values become higher than in the reference state; the ODS 12 Cr steel also exhibits an increase in  $S$  after annealing at 1573 K. The hypothesis is that, at 1400 and 1600 K, thermal vacancies are trapped by the oxide nanoparticles, accumulating at their interfaces with the matrix and being retained in the material upon cooling to room temperature.

**Keywords:** thermal-vacancy clusters, Y-Ti-O based nanoparticles, martensite, deformation state

## 6.1. Introduction

The Y-O based nanoparticles present in ODS (Oxide Dispersion Strengthened) steels potentially reduce the susceptibility of the steels to radiation-induced embrittlement, by acting as sinks to radiation-induced defects [53]. Given this ability of the Y-O nanoparticles, it is of interest to evaluate their interaction with other types of defects inherent to ODS steels, like dislocations, interfaces and vacancies introduced during deformation processes (mechanical alloying and thermomechanical treatments) and phase transformations, prior to any exposure to radiation. Positron Annihilation (PA) techniques are of fundamental importance for studying the formation and evolution of defects, exhibiting high sensitivity to open volume defects like vacancies, nanovoids, clusters of vacancies and clusters of solute atoms associated to vacancies, and, therefore, are widely used for defect analysis in nuclear materials [121]–[126].

There are multiple PAS studies conducted on non-irradiated ODS steels that aid in understanding the effect of processing on the final defect structure, which is of importance when determining the mechanisms involved in radiation damage formation, and that have contributed to understanding the mechanism of oxide nanoparticle precipitation in ODS steels. Ortega et al. [127] performed Positron Annihilation Lifetime Spectroscopy (PALS) and Coincidence Doppler Broadening (CDB) measurements on as-consolidated samples of Eurofer and Y<sub>2</sub>O<sub>3</sub>-ODS Eurofer. The authors have found that both steels absorb Ar atoms during mechanical alloying, carried out in Ar atmosphere. The residual Ar atoms would facilitate the nucleation of thermal-vacancy clusters during subsequent processing stages. In the Y<sub>2</sub>O<sub>3</sub>-ODS Eurofer steel, the oxide particles stimulate the nucleation of clusters of thermal vacancies associated to Ar atoms and keep them stable even after annealing at 1523 K [127]. The formation of stable clusters of vacancies, Ar atoms and oxide nanoparticles can have direct implication on the steel's uptake of H, He, D, T. Degmova et al. [128] used PALS and CDB, in combination to other non-destructive techniques, to study the precipitation of Cr-rich BCC phase ( $\alpha'$ ) and the dissolution and re-precipitation of Y-Al-O based nanoparticles during annealing at ~750 K (475 °C) for 750 h [128]. According to Fu et al. [129], the pre-existence of an excess of vacancies in an Fe matrix increases the solubility of O atoms, due to the very low formation energy of O-vacancy pairs. The O-vacancy pairs can behave as nucleation sites for Y-Ti-O nanoparticles, because of the high affinity of Y and Ti for oxygen [129]. Druzhkov and Perminov [121] have shown, using the Angular Correlation of Annihilation Radiation (ACAR) technique, that the main trapping sites for positrons in a 14 YWT alloy (steel alloyed with Cr, Y, W, Ti) are the fine and highly dense Y-Ti-O nanoparticles dispersed in the matrix.

In this case, the positrons annihilate at O-vacancy pairs or complexes within the Y-Ti-O nanoparticles. The authors show that vacancies are part of the constitution of Y-Ti-O nanoparticles [121], in agreement with the theoretical predictions of Fu et al. [129].

The interpretation of PAS data in non-irradiated materials can be challenging, due to the multiple types of defects present in steels and the occurrence of competing microstructural processes during thermal exposure. In the present chapter, Positron Annihilation Doppler Broadening data obtained for several ODS steels and alloys is discussed in terms of microstructural changes during annealing and processing treatments, interaction with oxide nanoparticles and Cr content.

### 6.1.1. Principles of Positron Annihilation in Crystalline Solids

Before any further discussion it is important, first, to understand the basic physical principles behind the technique. Annihilation between positrons and electrons results in photons. The most frequent type of annihilation occurring in dense materials is the process that originates 2  $\gamma$  photons [130]:



To satisfy conservation of energy and momentum during the process, i.e., guarantee that the momentum and energy of the positron-electron pair will be transferred completely when the positron and the electron are at rest, the 2  $\gamma$ 's are emitted in exact opposite directions (the angle between them is 180 °) and the energy of each photon is  $m_0c^2 = 511$  keV, where  $m_0$  is the electron mass at rest and  $c$  is the velocity of light.

Prior to annihilation, positrons interact with the solid in different ways, as schematized in Figure 6.1.

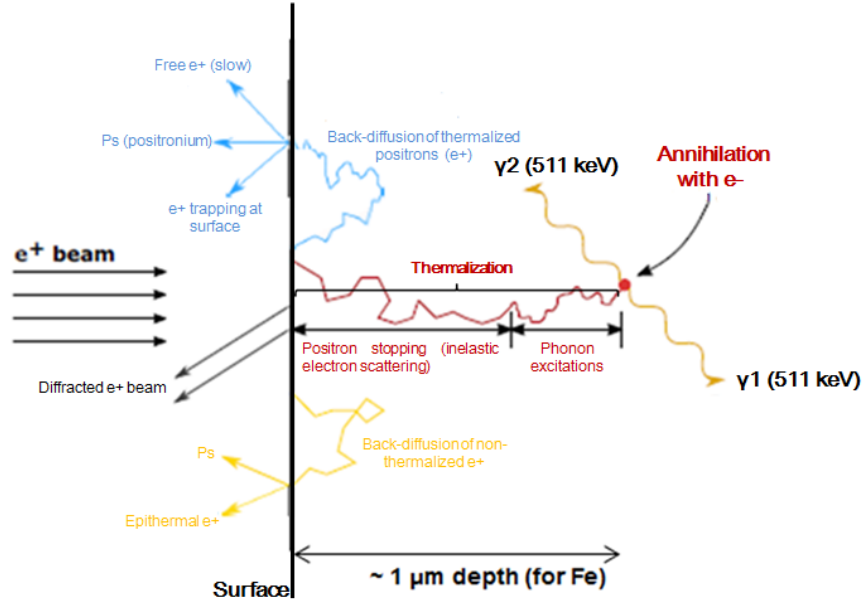


**Figure 6. 1.** Possible types of interactions between the incident positron beam and a metallic material, in this case considered to be Fe. Modified from [130], [131].

A first possible type of interaction between the incident positron beam and the crystalline material is diffraction. Part of the positron beam can be elastically scattered by the crystalline surface of the sample and part of it can enter the lattice. Once inside the lattice, different events might occur: (i) fast positrons will lose their kinetic energy until they reach thermal equilibrium with the lattice atoms, in a process called thermalization; (ii) part of the thermalized positrons can diffuse back to the surface; (iii) non-thermalized positrons can also move back to the surface (epithermal positrons); (iv) thermalized positrons can diffuse through the lattice and annihilate with an electron. The cross section of the  $2\gamma$  annihilation reaction is higher when the positrons present thermal velocity [130]:

$$\sigma_{2\gamma} = \frac{\pi r_0^2 c}{v} \quad (6.2)$$

Where  $r_0$  is the classical radius of the electron ( $2.818 \times 10^{-15}$  m) and  $v$  is the velocity of the positron [130].

Positrons become thermalized by a sequence of two main processes: first, scattering with electrons, which slows down the positrons to an energy closer to thermal levels, and phonon excitations, responsible for further energy loss to thermal levels. The whole thermalization process has a duration of approximately 10 ps [130].

When diffusing through the material lattice, positrons are affected by the charges of the ion cores (positive) and also by the electrons. In a defect free material, the positrons will diffuse through the interstices between atoms, in a delocalized Bloch state, until annihilation with a conduction or core electron [132]. Figure 6.2(a) shows the calculated Bloch state positron density in a defect-free tungsten lattice [133]. In Figure 6.2(a), the density minima correspond to the vicinity of ion cores and the maxima correspond to interstices [133]. When the lattice contains defects like vacancies, vacancy clusters, dislocations, among others, these will constitute preferential sites for positron occupation, since the charge density in these sites is lower [123], [130]. Hence, when encountering a defect the positron will be trapped, i.e. be highly localized in the defect [123], [130], [132], [133]. Figure 6.2(b) shows the calculated positron density in the vacancy-trapped state, in W [133]. The probability of annihilation with conduction electrons is higher for a positron trapped in a defect.

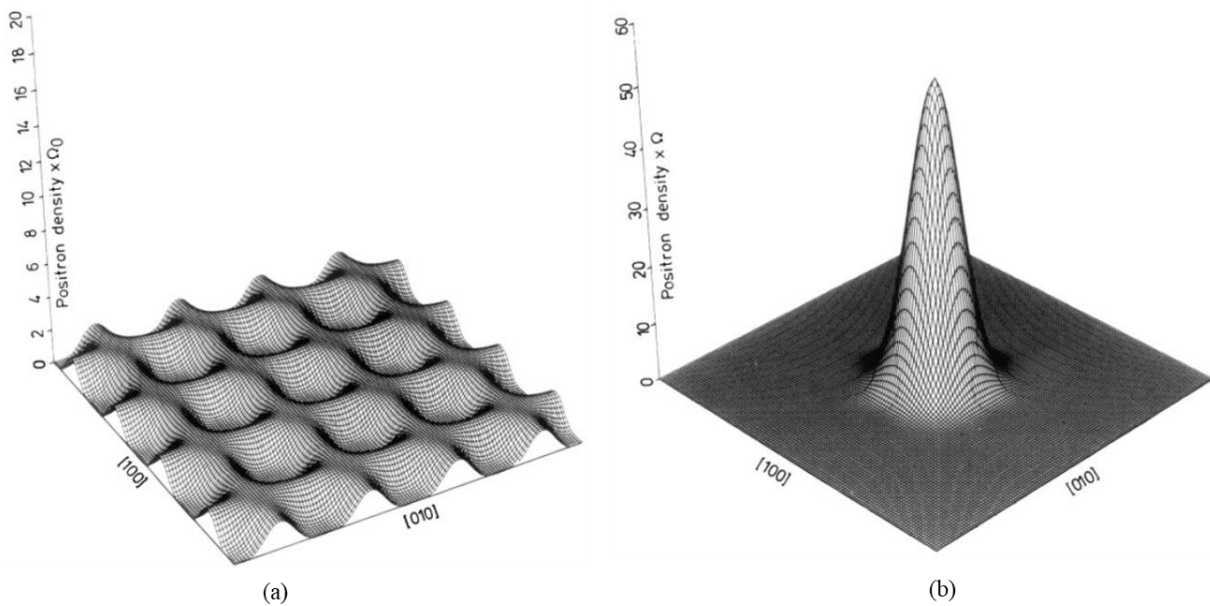


**Figure 6. 2.** Positron densities in tungsten (a) in a defect-free lattice, with positrons in a delocalized Bloch-state (density maxima correspond to interstices) and (b) vacancy-trapped state. The positrons densities are normalized by the volume of the respective supercells [133].

Because a positron is thermalized before annihilation its momentum can be neglected with respect to the momentum of the electron. In metals, the bound core electrons have higher momenta than the conduction electrons. In a solid, annihilation of a positron and an electron will result in  $\gamma$  photons emitted under an angle that deviates from  $180^\circ$  and will have energies slightly different from 511 keV. The angular deviation,  $\Delta\theta$ , and the Doppler shifted energy  $E_{DB}$  of the annihilation gammas are calculated by

$$\Delta\theta = \frac{p_p}{m_0c} \quad (6.3)$$

and

$$E_{DB} = m_0c^2 \pm \frac{p_e c}{2} \quad (6.4)$$

where  $p_p$  and  $p_e$  correspond to the electron momentum components perpendicular and parallel to the  $\gamma$  emission direction, respectively.

These principles lie behind the different Positron Annihilation techniques: angular correlation (*ACAR*), Doppler broadening (*PADB*) and lifetime (*PALS*).

In an *ACAR* measurement, the angle between pairs of emitted  $\gamma$  photons is measured by two position-sensitive detectors, one for each photon. A coincidence circuit ensures that only the angular positions from gammas from the same annihilation event are recorded. Thus, 2-dimensional information about the electron momentum distribution of metals can be provided by this technique [123]. In the lifetime technique, the time difference between the birth of a positron (moment when positron is emitted by a source) and its death (annihilation with electron) is measured. One of the most common types of positron source used in *PA* is the  $^{22}\text{Na}$  isotope and its simplified decay scheme is shown in Figure 6.3 [123], [130], [134].

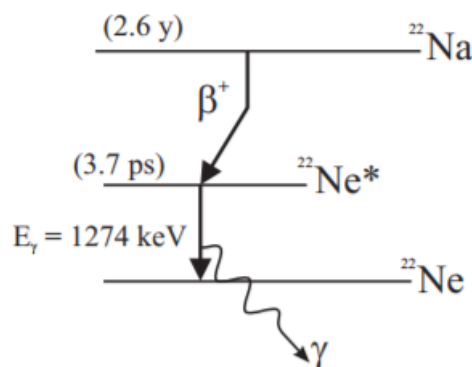


**Figure 6. 3.** Simplified scheme of the  $^{22}\text{Na}$  decay into  $^{22}\text{Ne}^*$ , emitting a  $\beta^+$  (positron); after 3.7 ps,  $^{22}\text{Ne}^*$  goes to its ground state, by the emission of a  $\gamma$  of 1.274 MeV [134].



$^{22}\text{Na}$  has a half-life of 2.6 years, which is conveniently long to do experiments, and goes through  $\beta^+$  decay forming  $^{22}\text{Ne}^*$  (isotope in the excited state). After 3.7 ps, the  $^{22}\text{Ne}^*$  emits a  $\gamma$  photon of 1.274 MeV and reaches its ground state. Given the short lifetime of the excited state, the instant of birth of the positron can be determined by the detection of the 1.274 MeV photon [123], [130], [134]. The moment of annihilation with an electron is determined by the detection of one of the 511 keV annihilation  $\gamma$ 's. The positron lifetime is related to the electron density in an annihilation site (trap or interstitial) and is the reciprocal of the annihilation rate. With the lifetime technique is possible to obtain information about the type of defect in the material and its concentration [123], [130], [134].

Finally, in the Doppler broadening technique the energy of the annihilation  $\gamma$  is measured. This is the technique used in the present thesis and is described in more detail in Section 6.2.2.

## **6.2. Experimental**

### **6.2.1. Materials**

Three types of ODS steels (ODS Eurofer, ODS 12 Cr and 14YWT) and FeCr binary alloys were analysed, produced via conventional powder metallurgy routes consisting of mechanical alloying, consolidation via hot extrusion or hot isostatic pressing and post-consolidation treatments. The martensitic ODS Eurofer and the ferritic ODS 12 Cr steel were submitted to 1 h annealing in an electric resistance furnace, under  $10^{-7}$  mbar, at temperatures varying from 573 K to 1600 K. Cooling to room temperature took place inside the furnace by switching off its power supply, as described in Chapter 3. A typical cooling curve can be seen in Figure 3.1, from which it is possible to estimate an average cooling rate of  $0.5 \text{ K}\cdot\text{s}^{-1}$  between 1050 K and 750 K, a temperature range critical for phase transformations. The ferritic 14 YWT steel, previously studied in [135], was analysed in its as-produced condition. The details of the chemical composition of the alloys, the nomenclature used, the fabrication method and additional heat treatments performed are summarized in Table 6.1.

**Table 6. 1.** Summary of materials analysed and processing conditions.

<b>Material</b>	<b>Nominal chemical composition (weight%)</b>	<b>Processing conditions (as-received state)</b>	<b>Additional heat treatment</b>
0.3% Y <sub>2</sub> O <sub>3</sub> ODS Eurofer	Fe-0.1C-9Cr-1W-0.2V-0.3Y <sub>2</sub> O <sub>3</sub>	<ul style="list-style-type: none"> <li>• Mechanical alloying (MA)</li> <li>• Consolidation by hot isostatic pressing</li> <li>• Thermomechanical treatment</li> </ul>	<ul style="list-style-type: none"> <li>• Reference State: 1253 K, 0.5 h + cooling inside furnace to room temperature + tempering 1073 K, 1.5 h + cooling inside furnace to room temperature</li> <li>• Annealing for 1 h at 600, 800, 1000, 1200, 1400 and 1600 K</li> </ul>
ODS 12 Cr	Fe-0.03C-12.3Cr-1.7W-0.3Ti-0.3Y <sub>2</sub> O <sub>3</sub>	<ul style="list-style-type: none"> <li>• MA in Ar atmosphere</li> <li>• Consolidated by hot extrusion</li> <li>• Thermomechanical treatment</li> </ul>	<ul style="list-style-type: none"> <li>• Annealing for 1 h at 773, 1273, 1373, 1473 and 1573 K</li> </ul>
FeCr binary alloys	Fe5Cr, Fe10Cr and Fe14Cr	<ul style="list-style-type: none"> <li>• MA in Ar atmosphere</li> <li>• Consolidated by hot isostatic pressing</li> <li>• Annealed at 1200 K for 1 h</li> </ul>	-
14YWT [11] and 14WT	Fe-0.1C-13.3Cr-2.7W-0.2Ti-0.3Y <sub>2</sub> O <sub>3</sub> and Fe-0.1C-13.3Cr-2.7W-0.2Ti	<ul style="list-style-type: none"> <li>• MA in Ar atmosphere</li> <li>• Consolidated by hot isostatic pressing</li> </ul>	-

### 6.2.2. Methods

Prior to the Positron Annihilation Doppler Broadening measurements sample preparation is necessary to remove any oxide layers that formed during high temperature annealing treatments and other imperfections at the surface, originated during cutting or pre-processing of the materials. All samples were prepared according to the following steps: (1) sanding with SiC paper of grits 800, 1200 and 2000 (SiC particle size of 10 µm), for approximately 30 s at each grit; (2) intermediate mechanical polishing with diamond suspensions with particle sizes 3 and 1 µm, for respectively 6 and 12 minutes and (3) final mechanical polishing with silica suspension with particle size 0.05 µm for 30 to 40 min. Step (3) is of particular importance because it removes the deformation layer introduced in the material during steps (1) and (2), to which positrons are highly sensitive.

The Positron Annihilation Doppler Broadening (PADB) measurements were conducted at the Delft Variable Energy Positron (VEP) beam, Reactor Institute Delft. At the Delft VEP facility, positrons emitted by a  $^{22}\text{Na}$  source, after moderation, can be accelerated to energy values ranging from 0.1 keV to a maximum of 25 keV and are then implanted in a sample, allowing defect analysis at different depths of material., The positron mean implantation depth is related to the implantation energy by

$$\langle z \rangle = \frac{A}{\rho} E^{1.62} \quad (6.5)$$

where  $A = 4 \times 10^4 \text{ nm.kg.m}^{-3}.\text{keV}^{-1.62}$  [136] is an empirical constant,  $\rho$  is the density of the material,  $\langle z \rangle$  is the positron mean implantation depth and  $E$  is the positron implantation energy [136]. For  $\rho$  the density of Fe ( $7800 \text{ kg.m}^{-3}$ ) is adopted.

Thermalized positrons diffuse through the material lattice and in most cases ultimately annihilate with an electron resulting in the emission of two  $\gamma$  photons. To satisfy conservation of energy and momentum during the annihilation process, for a positron-electron pair at rest the two  $\gamma$  photons are emitted in opposite directions, each carrying an energy of 511 keV. Since the positrons are thermalized before annihilation, their contribution to the momentum can be neglected in comparison to the momenta of electrons in the material. Due to the momentum of the electron, annihilation of a positron and an electron will result in  $\gamma$  photons emitted with an angle deviating from collinearity and with energies slightly different from 511 keV. The Doppler-shifted photon energy is given by Equation 6.4 (presented earlier in Section 6.1.2)

$$E_{DB} = m_0 c^2 \pm \frac{p_e c}{2} \quad (6.4)$$

where  $p_e$  corresponds to the electron momentum component parallel to the  $\gamma$  emission direction,  $m_0$  is the electron rest mass and  $c$  is the velocity of light. In metals, the core electrons have a broader momentum distribution than the conduction electrons and thus give a wider  $\gamma$ -energy spread.

PADB uses high energy resolution Ge detectors (FWHM = 1.2 keV at 511 keV) to measure the  $\gamma$  energy spectrum. Two line-shape parameters,  $S$  (sharpness) and  $W$  (wing), are used to quantify the Doppler-broadening of the 511 keV photo-peak. The  $S$ -parameter is given by the fraction of counts in a central region of the spectrum, in relation to the total counts, and the  $W$ -parameter corresponds to the fraction of counts in the extremities of the spectrum. Figure

6.4 shows a schematic of a Doppler-broadening spectrum with the  $\gamma$ -energy ranges defining the  $S$  and  $W$  parameters indicated. For the experiments, the  $S$  and  $W$  regions were determined by the momenta regions of  $|p_e| < 3.5 \times 10^{-3} m_0c$  and  $1.0 \times 10^{-2} m_0c < |p_e| < 2.6 \times 10^{-2} m_0c$ , respectively.

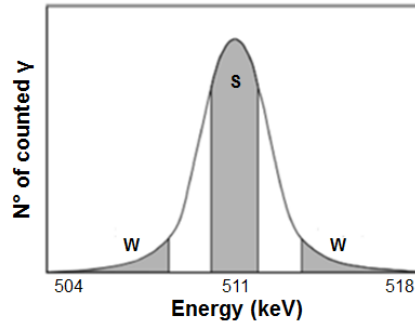


**Figure 6. 4.** Schematic of a Doppler Broadening 511 keV annihilation spectrum. The shaded  $S$  and  $W$  regions are defined such as to obtain maximum sensitivity for annihilations with electrons of low momentum ( $S$ ) or high momentum ( $W$ ).

In a defect-free material, the positrons will diffuse through the interstices between atoms until they annihilate with an electron, which can either be a conduction electron or a core electron. In a material containing open-volume defects, like vacancies, the positrons will be preferentially trapped in those defects, where the repelling Coulomb force between the positron and atom cores is at a minimum [130]. When trapped in an open-volume defect the positron has a higher probability of annihilating with a conduction electron. Annihilation with conduction electrons leads to small shifts in the  $\gamma$  energy from 511 keV and, therefore, to  $\gamma$  energies in the  $S$  range. Annihilation with more energetic core electrons results in a larger energy shift and, hence, contributes to the  $W$  range.

## 6.3. Results

### 6.3.1. Effect of sample preparation on PADB results

In order to illustrate the importance of adequately preparing metallic samples prior to positron annihilation measurements, Figure 6.4 shows PADB results for the ODS 12 Cr steel in the as-received state and prepared according to different routes. Measurements were done after completion of each preparation step described in section 6.2.2 and also on samples that, after mechanical polishing with 1  $\mu\text{m}$  diamond suspension, were electropolished in 1% oxalic acid aqueous solution, at 4 V, for 8, 12, 16 and 20 min.

The high  $S$  and low  $W$  values observed for the ground sample clearly indicate that grinding introduces a layer with a high concentration of defects (dislocations and vacancies). Further mechanical polishing with diamond suspensions of smaller particle sizes removes the deformation layer formed during grinding, as shown by the considerable decrease in  $S$ -parameter and increase in  $W$ -parameter. Nevertheless, mechanical polishing as a (less aggressive) form of abrasion still introduces defects in the material. This becomes evident after comparison with the electropolished samples. By electropolishing, layers of material are removed by a process of controlled corrosion, without the application of any mechanical load to the material surface. In Figure 6.5 it is shown that electropolishing for 8 min results in  $S$  and  $W$  values that are very similar to the ones obtained after mechanical polishing with 1  $\mu\text{m}$  diamond, hence the immersion time was not enough to completely remove the deformation layer. Electropolishing for 12 min, 16 min and 20 min leads to the same, low  $S$  values, indicating that, after 12 min, the deformation layer is removed. This allows thermalized positrons to diffuse further into the material and interact with the defects in the bulk (positrons with implantation energy above 8 keV). Observation of the electropolished samples with optical microscopy shows that after electropolishing for 16 min and 20 min a small number of corrosion pits are formed. Finally, Figure 6.5 shows that using step (3), mechanical polishing with 0.05  $\mu\text{m}$  silica for 30-40 min, proves to be equally efficient regarding the removal of the deformation layer, as it provides  $S$  and  $W$  parameters in the same range as after electropolishing for 12 min. Since the silica suspension is slightly acid, so, besides abrasion, it removes the deformation layer by etching the surface of the sample. In our experiments we chose to finalize the sample preparation with polishing with silica which, for many types of steels, can be a suitable and simpler method than electropolishing. It is important to mention that the electropolishing method used here is suitable for the ODS 12 Cr steel. In the case of the ODS Eurofer steel, for example, the optimum duration of electropolishing with the same electrolyte is 9 min and longer periods of time cause high levels of pitting.

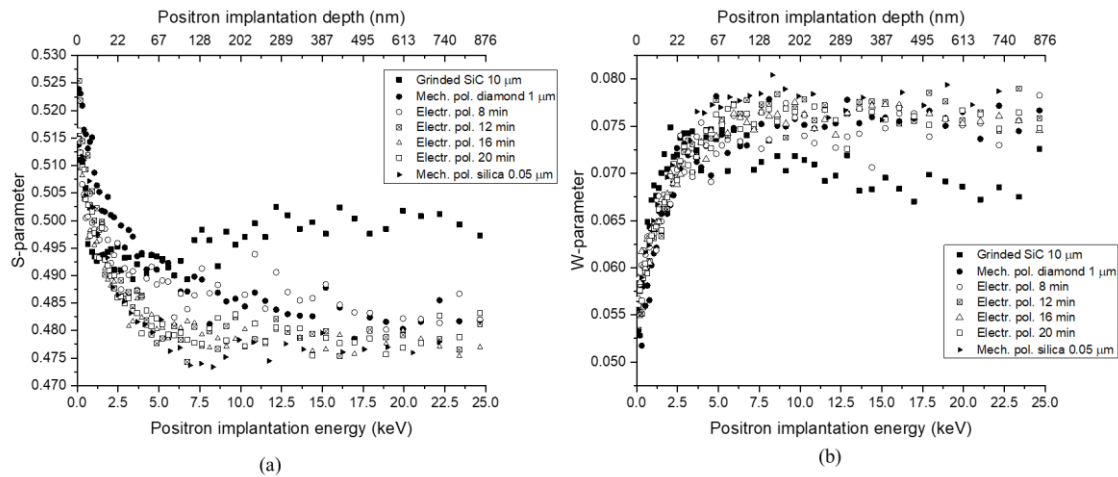


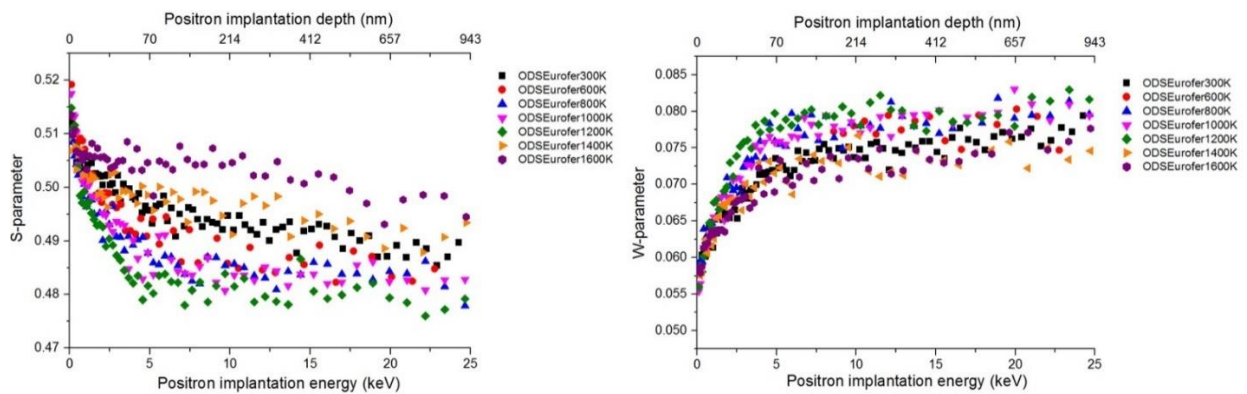
**Figure 6. 5.** (a) S-parameter and (b) W-parameter vs positron implantation energy. Results were obtained for samples in the as-received state of the ODS 12 Cr steel, prepared by different methods.

### 6.3.2. Annealing of the 0.3% $Y_2O_3$ -ODS Eurofer steel

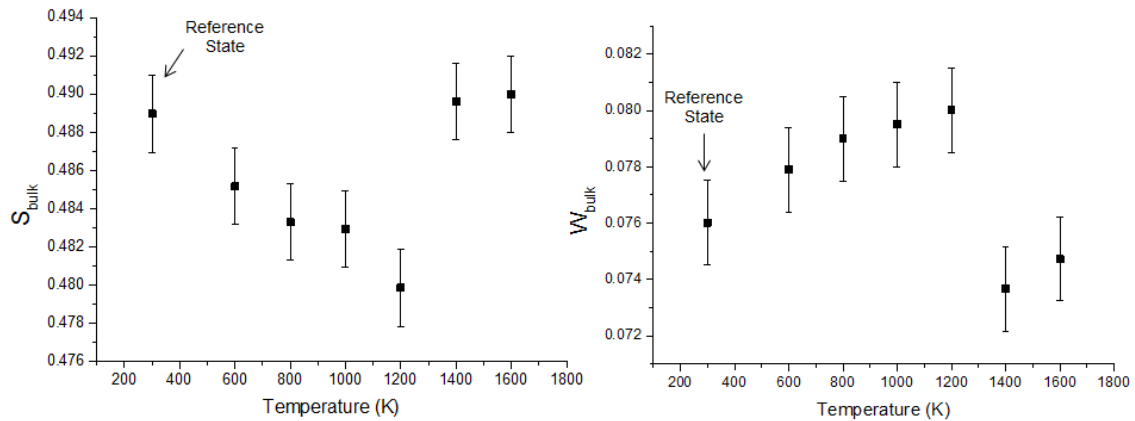
The 0.3%  $Y_2O_3$ -ODS Eurofer steel has a high concentration of defects that are intrinsic to the microstructure, like grain boundaries, interfaces of  $M_{23}C_6$  precipitates, dislocations, Y-O based nanoparticles and solute elements. With the exception of oxide nanoparticles, these defects are also present in a non-ODS Eurofer steel. The 0.3%  $Y_2O_3$ -ODS Eurofer steel was fabricated by mechanical alloying, a process that subjects the material to severe deformation. Even after consolidation and heat treatment, a considerable density of defects caused by deformation remains stored in the microstructure in the form of a high grain boundary area density (Figures 3.6 and 3.7, Chapter 3). In the Inverse Pole Figure OIM maps of Figure 3.6, Chapter 3, an orientation gradient inside many grains of almost all annealed samples has also been observed, confirming the existence of a deformed state in the material. Therefore, in addition to the cited defects which are intrinsic to the microstructure, the 0.3%  $Y_2O_3$ -ODS Eurofer steel contains defects introduced during mechanical alloying. This type of defects, referred to as carriers of deformation, are taken into account in the interpretation of the PADB results.

Figure 6.6 shows the S-parameter and W-parameter as a function of the positron implantation energy and positron mean implantation depth (top axis). Average values for S and W were calculated for each annealing condition using the data obtained at implantation energies above 10 keV, which are representative of annihilation events occurring in the bulk. The thus obtained  $S_{bulk}$  and  $W_{bulk}$  values are plotted in Figure 6.7 as a function of the annealing temperature. Figure 6.8 displays the SW map, which was obtained by plotting the  $W_{bulk}$  value of each condition vs its  $S_{bulk}$  value. Note that high S and low W values are related to a high

concentration of defects in the material. By definition a change of  $S$  is accompanied by an opposite change in  $W$ , when the positron environment does not go through chemical alterations. In other words, when only two types of non-altering positron traps are involved, the slope of the line connecting  $(S, W)$  points, given by the parameter  $R = \left| \frac{\Delta S}{\Delta W} \right|$ , should be constant. A change in slope thus indicates (additional) positron trapping at a different type of defect. If this change in slope is ascribed to  $W$ , which derives from annihilations with core electrons, it indicates a different chemical environment at the positron trapping/annihilation site [130], [137].



**Figure 6. 6.**  $S$ -parameter and  $W$ -parameter as a function of positron implantation energy and positron implantation depth, obtained for the 0.3%  $Y_2O_3$  ODS Eurofer steel, annealed for 1 h at different temperatures.



**Figure 6. 7.**  $S_{bulk}$  and  $W_{bulk}$ , calculated for the 0.3%  $Y_2O_3$  ODS Eurofer steel vs the annealing temperature.

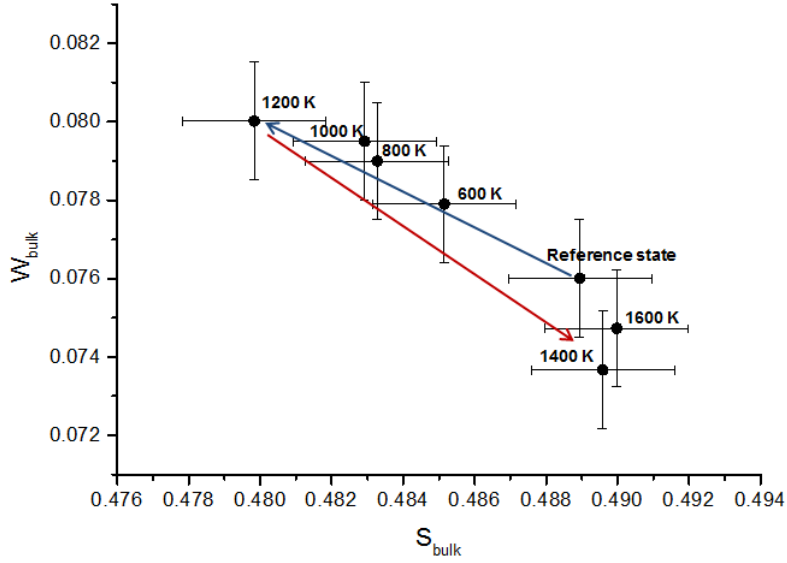


**Figure 6. 8.** *SW* map of the 0.3%  $Y_2O_3$ -ODS Eurofer steel. The blue arrow indicates the evolution of the *SW* pair from the reference state until annealing at 1200 K. The red arrow shows the change in behaviour after annealing at 1400 K.

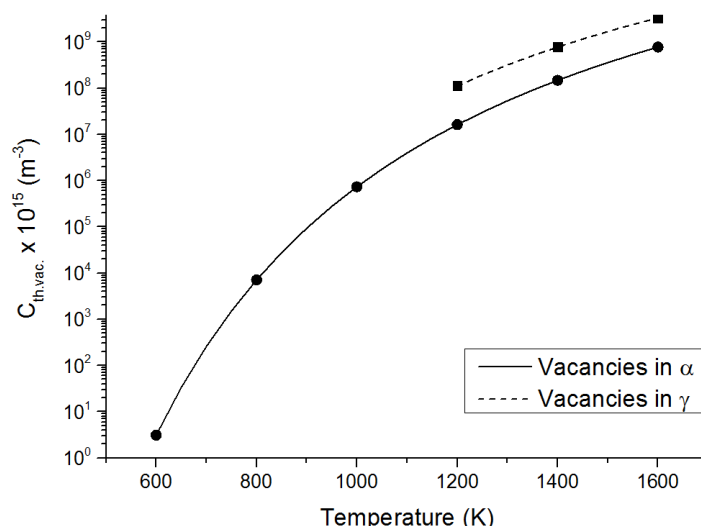
For treatments up to 1200 K, a continuous decrease in  $S$  and increase in  $W$  with annealing temperature is seen, which is indicative of a decrease in defect concentration. Then, after annealing at 1400 K and 1600 K, the  $S$ -parameter increases, reaching values higher than in the reference state. The opposite behaviour is seen for  $W$ .

Figure 6.9 shows the equilibrium density of thermal vacancies in ferrite and austenite vs temperature. The equilibrium density of thermal vacancies was calculated according to:

$$C_{th.vac.} = N_{Fe} \exp\left(\frac{-E_f}{kT}\right) \quad (6.5)$$

where  $N_{Fe}$  is the Fe atomic density ( $8.47 \times 10^{28} \text{ m}^{-3}$ ),  $E_f$  is the vacancy formation energy in the metal,  $k$  is the Boltzmann constant and  $T$  is the temperature. For ferrite, we use  $E_f = 1.6$  eV [138] and for austenite,  $E_f = 1.4$  eV [138]. In this estimated quantification, we consider only the contribution of Fe vacancies and we do not take into account the effect of Cr, or other alloying elements, on the vacancy formation energy [139].





**Figure 6. 9.** Equilibrium density of thermal vacancies in ferrite and austenite vs annealing temperature.

In Figure 6.9, when the material is above 1200 K, the equilibrium density of thermal vacancies in ferrite and austenite increases significantly, being 2 to 4 orders of magnitude higher than in ferrite at 1000 K. The density of thermal vacancies in ferrite at 1200 K and above is considered because it coexists with austenite in the material, due to the incomplete austenitization of ODS 9 Cr steels in the range 1200 K – 1400 K [36], [66] and to the entrance in the dual-phase field  $\gamma+\delta$  at 1600 K (Figure 3.2, Chapter 3). At 1400 K and 1600 K, besides the higher density of thermal vacancies, the Fe atoms also present a higher self-diffusivity, especially in ferrite [140] and, consequently, the thermal vacancies are several orders of magnitude more mobile than at 1000 K. These characteristics of Fe can explain the *SW* behaviour observed at 1400 K and 1600 K. The hypothesis is that the Y-O based nanoparticles in the steel are trapping and stabilizing thermal vacancies at all annealing temperatures. Nevertheless, at 1400 K and 1600 K, the higher density of thermal vacancies, with increased mobility, leads to the formation of larger clusters that are trapped at the Y-O nanoparticles. Upon cooling, the larger vacancy clusters are retained in the microstructure, leading to the high *S* values and change in trend for the *SW* pairs seen in Figure 6.8.

A similar annealing study was previously carried out on the non-ODS Eurofer steel [131]. In the non-ODS steel only a continuous decrease in *S* and increase in *W* with annealing up to 1600 K was observed (Figure 6.10) [131]. Thermal vacancies were also formed in the non-ODS Eurofer steel, however, because Y-O based clusters are not present, the thermal vacancies are not retained in the structure upon cooling. The trend observed in Figure 6.10 for the non-ODS Eurofer steel was associated with a general decrease in defect concentration due to events like tempering of martensite, grain growth, dissolution of carbides and martensite formation after annealing at 1200, 1400 and 1600 K [131].

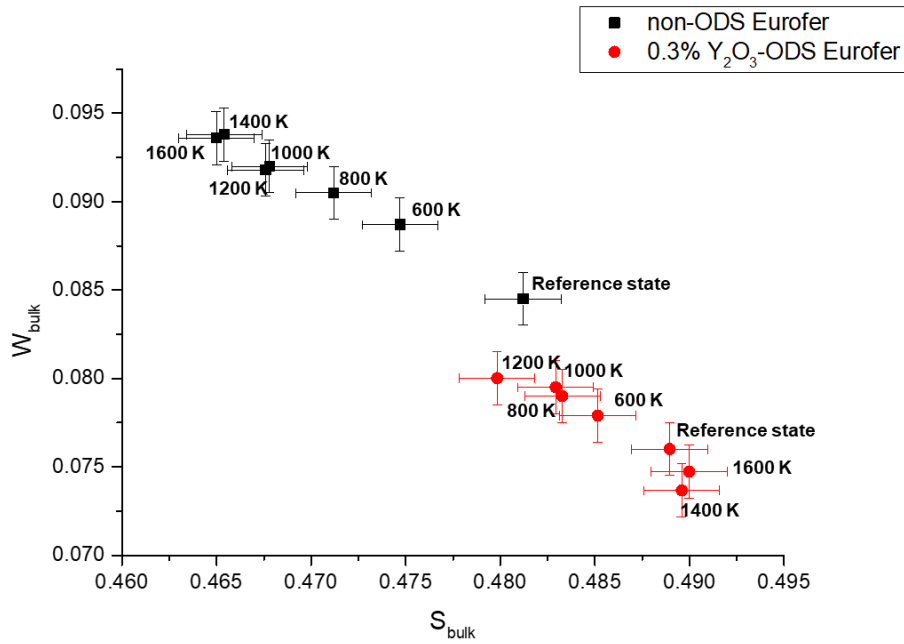


**Figure 6. 10.** *SW* map comparing the non-ODS Eurofer steel (black squares) [131] with the 0.3%- $Y_2O_3$  ODS Eurofer steel (red circles).

A consideration of the microstructural changes occurring in the non-ODS Eurofer steel was necessary to understand the defect evolution detected with positrons. For the 0.3%  $Y_2O_3$ -ODS Eurofer steel this type of analysis is more complex, since the microstructure forms and evolves differently due to the presence of Y-O based nanoparticles. In addition, the steel contains the carriers of deformation described earlier, which are responsible for the overall higher  $S$  and lower  $W$  depicted in Figure 6.10, along with Y-O based nanoparticles. In Section 6.4.1 the PADB results are discussed in relation to these aspects.

### 6.3.3. Effect of annealing treatments on the evolution of defects in the ODS 12 Cr steel

Figure 6.11 shows the  $S$ -parameter and  $W$ -parameter profiles as a function of positron implantation energy and positron implantation depth for the ODS 12 Cr steel annealed at different temperatures for 1 h. In Figure 6.12 the variation of  $S_{bulk}$  and  $W_{bulk}$  with annealing temperature is shown.

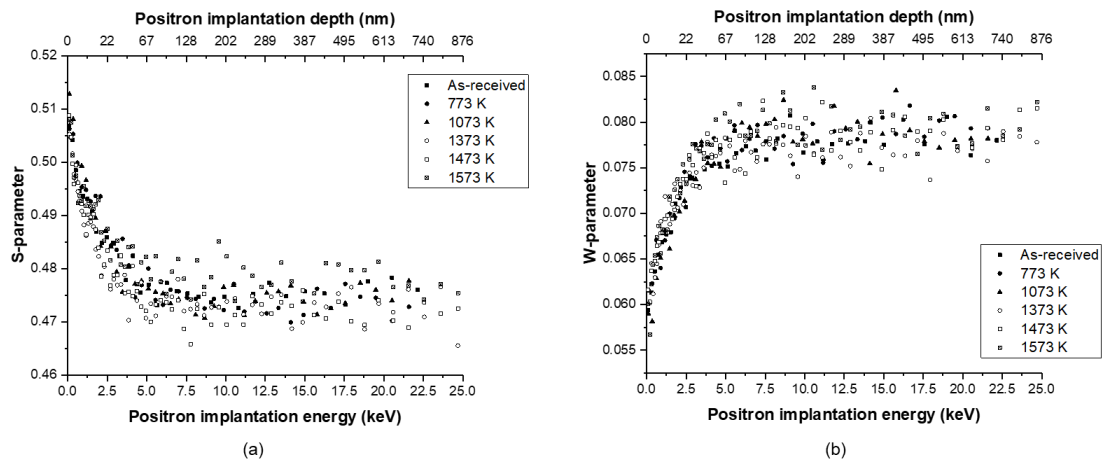


**Figure 6.11.**  $S$ -parameter and  $W$ -parameter as a function of positron implantation energy and positron implantation depth, obtained for the ODS 12 Cr steel, annealed for 1 h at different temperatures.

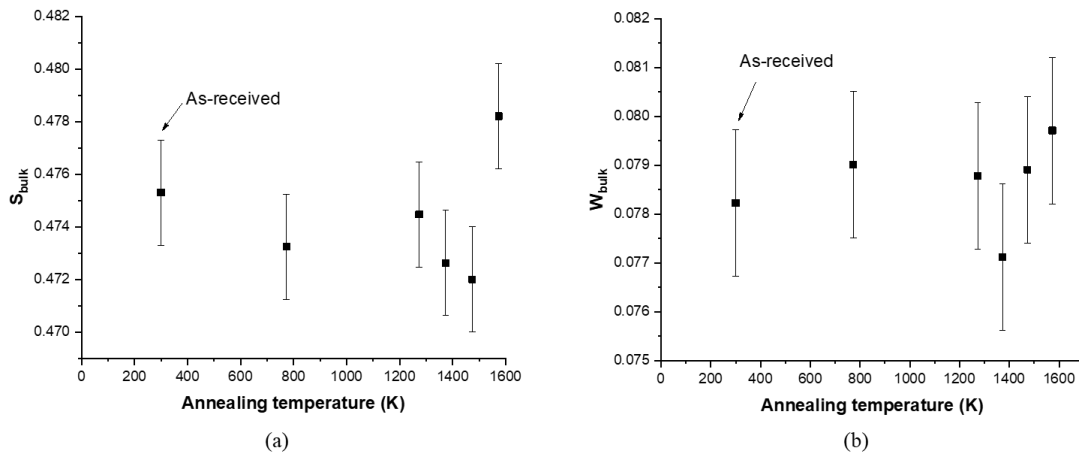


**Figure 6.12.**  $S_{bulk}$  and  $W_{bulk}$ , calculated as the average of the data obtained with positron energies above 10 keV, vs the annealing temperature.

The  $S$  and  $W$  parameters do not show any significant effect of the annealing temperature, except for an increase in  $S_{bulk}$  of the sample annealed at 1573 K, which is not accompanied by a decrease in  $W_{bulk}$ . In the  $SW$  plot of Figure 6.13, the  $SW$  pairs of the ODS 12 Cr steel are located towards the left side of the plot, in relation to the data measured for the 0.3%  $Y_2O_3$  ODS Eurofer steel. These results suggest that the main type of defect contributing to  $S$  and  $W$  in the ODS 12 Cr steel is thermally more stable and is different from the dislocations (carriers of deformation) present in the 0.3%  $Y_2O_3$  ODS Eurofer steel.

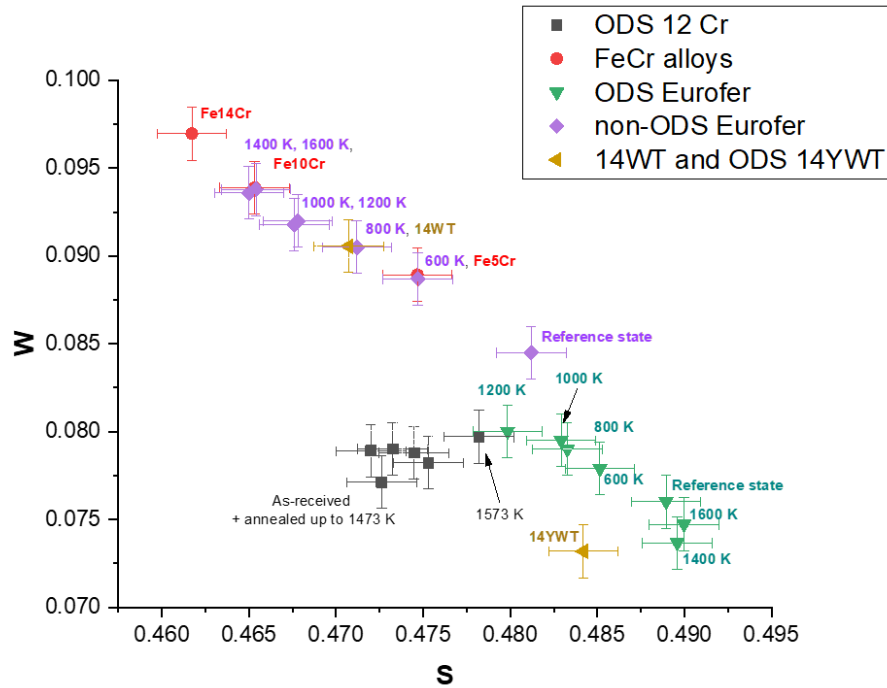


**Figure 6.13.** *SW* map comparing the ODS 12 Cr steel to the other alloys measured in the present study and the non-ODS Eurofer of [131].

The main differences between the two steels are (1) the higher Cr content (12% vs 9%) and (2) the presence of Ti in the ODS 12 Cr steel. In order to evaluate the effect of different Cr contents on the PADB parameters, FeCr binary alloys containing 5, 10 and 14 weight% Cr were measured. As it can be seen in Figure 6.13, the FeCr alloys actually have their *SW* points located along a single line, which coincides with the data of the non-ODS Eurofer steel [17]. This indicates that the types of defects detected by positrons in the FeCr alloys and non-ODS Eurofer steel are the same and are likely the dislocations, interfaces and vacancies associated to the martensitic transformation (Cr content up to 10 weight %). The second investigated aspect is related to the presence of Ti in the chemical composition of the steel. The addition of Ti in ODS steels has the purpose of forming fine and thermally stable Y-Ti-O nanoparticles. As discussed in Chapters 3 and 5, the oxide nanoparticles present in the ODS 12 Cr steel are Y-Ti-O based and the ones in the 0.3% Y<sub>2</sub>O<sub>3</sub> ODS Eurofer are Y-V-O based, with the former having a higher thermal stability. The 14 YWT ODS steel, studied by Davis et al. [135] also contains fine, Y-Ti-O based nanoparticles and, therefore, a PADB measurement was carried out in this material, on its as-produced condition. Figure 6.13 shows that the *SW* point of the 14 YWT steel is located on the side of lower *S*, in relation to the data of the 0.3% Y<sub>2</sub>O<sub>3</sub> ODS Eurofer, but with higher *S* and lower *W* than the ODS 12 Cr. This could be a suggestion that the main positron trapping sites and, thus, main contributors for the measured *S* and *W* in the

ODS 12 Cr and 14 YWT ODS steels are the Y-Ti-O based nanoparticles, but more measurements are necessary to verify this hypothesis, including measurements on pure Ti and an annealing study similar to what is here presented for ODS 12 Cr and ODS Eurofer steels. Additionally, the non-ODS 14 WT was also measured (same composition and fabrication method as the 14 YWT, but without the addition of  $Y_2O_3$ ), and its *SW* point is located along the line of the non-ODS alloys.

## **6.4. Discussion**

### **6.4.1. Thermal evolution of defects in the 0.3% $Y_2O_3$ -ODS Eurofer steel**

#### ***6.4.1.1. Samples in the reference state and annealed at 600, 800 and 1000 K***

The microstructural observations made with SEM and EBSD in Chapter 3 show that annealing at 600 K, 800 K or 1000 K does not alter the reference state microstructure significantly, except for a small shift of the grain size distribution towards larger values and a (qualitative) change in crystallographic orientation. Additionally, these annealing treatments do not have significant effect on the average Vickers hardness of the material, which presents a constant value of  $\sim 350$  HV. On the other hand, the PADB results presented in Section 6.3.2 show (1) a continuous decrease in defect concentration with annealing up to 1000 K and (2) the *SW* pairs in Figure 6.8 vary linearly, suggesting the removal of a type of defect that is common to all these conditions. Based on these observations, it is possible to conclude that the main microstructural process occurring with annealing between 600-1000 K is the recovery of the deformed state of the material, introduced during mechanical alloying. Hence, the decrease in the concentration of defects and the linear variation of *SW* are mainly due to the removal of carriers of deformation (mainly dislocations).

#### ***6.4.1.2. Sample annealed at 1200 K***

After annealing at 1200 K and upon cooling to room temperature, a martensitic structure is formed. A first expectation would be to observe an increase in defect concentration, mainly of martensite grain boundaries, dislocations and vacancies associated with this constituent, but the PADB results show exactly the opposite: the *S* parameter is the lowest after this heat treatment. To better understand this unexpected behaviour, it is necessary to discuss separately the evolution of defects intrinsic to the microstructure (carbide interfaces, grain

boundaries, dislocations associated to martensitic transformation) and of the carriers of deformation (defects introduced during mechanical alloying).

At 1200 K,  $M_{23}C_6$  carbides dissolve and, upon cooling to room temperature, the carbides do not re-precipitate. Equiaxed martensite is formed, along with new dislocations. In comparison to samples in the reference state and annealed between 600 and 1000 K, the average grain size of the equiaxed martensite is approximately equal and, therefore, its contribution to  $S$  and  $W$  values, through the grain boundary surface area of martensite, is the same. Figure 6.10 shows that the  $SW$  values of the non-ODS Eurofer annealed at 1000 K and 1200 K are the same. This indicates that tempering of martensite, grain growth and interfaces of  $M_{23}C_6$  carbides at 1000 K are in balance with  $M_{23}C_6$  dissolution and creation of new defects due to martensite formation upon cooling from 1200 K. It is important to mention that the non-ODS Eurofer was cooled under the same cooling rate as the 0.3%  $Y_2O_3$ -ODS Eurofer, at an average of  $0.5 \text{ K}\cdot\text{s}^{-1}$  between 1050 K and 750 K, sufficiently fast to form martensite in both steels. Since the cooling rate employed was the same in both steels, it is possible to conclude that a similar balance between microstructural constituents described for the non-ODS Eurofer annealed at 1000 K and 1200 K can occur in the 0.3%  $Y_2O_3$ -ODS Eurofer steel at these temperatures.

As already mentioned, the 0.3%  $Y_2O_3$ -ODS Eurofer steel has additional types of defects: oxide nanoparticles and the carriers of deformation. Up to 1200 K the microstructure of the steel remains refined and this is an indication of the stability of the oxide nanoparticles, *i.e.* they remain with the same size distribution throughout the temperature range 600-1200 K. Hence, the contribution of the oxide nanoparticles to  $S$  and  $W$  values can be considered constant as well. The further decrease in  $S$  observed after annealing at 1200 K is likely due to the continuous removal of carriers of deformation, which can be considered as a surplus of dislocations present in ODS steels. In Figure 6.8, the position of the  $SW$  pair of the sample annealed at 1200 K follows the same trend as the samples in the reference state and annealed at 600-1000 K, suggesting that the nature of detected defects is the same. Sallez et al. [60] measured the dislocation density in an ODS ferritic steel with *in-situ* X-Ray Diffraction, during annealing at  $900 \text{ }^\circ\text{C}$  (1173 K) for 3000 s. The obtained value was  $3.5 \times 10^{15} \text{ m}^{-2}$ , at least 2 orders of magnitude higher than in a non-ODS steel [60]. This supports the PADB observations of  $SW$  and hypothesis here discussed.

### 6.4.1.3. Samples annealed at 1400 K and 1600 K

In Chapters 3 and 4, related to the characterization of the microstructure and oxide nanoparticles of the 0.3%  $Y_2O_3$ -ODS Eurofer steel, it was discussed that after annealing at 1400 K and 1600 K the microstructure becomes coarser. This is related to the coarsening of oxide nanoparticles, which already occurs at 1400 K, leading to a decrease of the Zener pinning force. In order to explain the increase in  $S$  and decrease in  $W$  measured with PADB, after annealing at these two temperatures, it is here proposed that the oxide nanoparticles, although coarser than in the reference state, are trapping and stabilizing clusters of thermal vacancies.

The results obtained by Ortega et al. [127] further support the hypothesis of Y-O based nanoparticles trapping thermal vacancies. The authors have assessed the effect of annealing treatments on as-consolidated  $Y_2O_3$ -ODS Eurofer, using Positron Annihilation Lifetime Spectroscopy (PALS) and TEM [127]. After annealing at 1523 K, an increase in positron lifetime is observed, which is attributed to the stabilization of Ar-vacancy clusters by Y-O based nanoparticles. TEM images of their material, after annealing at 1523 K, show Ar-vacancy voids located at the interfaces of the Y-O based particles [127]. Residual Ar atoms can be introduced into ODS steels during mechanical alloying, since the process is normally performed under Ar atmosphere. However, given that our steel was heat treated several times after consolidation, we consider that all possible residual Ar in solid solution was removed and that the increase in  $S$  and decrease in  $SW$ , after treatment at 1400 K and 1600 K, is a result of trapping of thermal-vacancy clusters only.

Furthermore, it is important to discuss the role of vacancy mobility in our interpretation of the PADB results. Figure 6.9 shows that the density of thermal vacancies at 1200 K is of the same order of magnitude as at 1400 K. Thus, attributing the  $SW$  behaviour seen at 1400 K and 1600 K solely to the increase in density of thermal vacancies would conflict with the lowest  $S$  observed after annealing at 1200 K. The Fe self-diffusivity in austenite at 1200 K is 3 and 4 orders of magnitude lower than at 1400 K and 1600 K, respectively, and 5 orders of magnitude lower than in  $\delta$ -ferrite at 1600 K [140]. Consequently, at 1200 K, even though the density of vacancies is high, their mobility is still low, significantly delaying the formation of larger clusters.

#### 6.4.2. Thermal evolution of defects in the ODS 12 Cr steel

The microstructure of the ODS 12 Cr steel, its grain size distribution and Vickers hardness are unaltered with annealing from 773 K to 1473 K (Figures 5.6, 5.7, 5.8 in Chapter 5). The Y-Ti-O based nanoparticles present in the matrix are also highly stable and only with annealing at 1573 K undergo coarsening, with the average particle diameter increasing from ~ 3 nm (as-received) to ~ 7 nm (Figure 5.11 in Chapter 5). The increase in oxide nanoparticle size leads to partial recrystallization of the microstructure, accompanied by a moderate decrease in Vickers hardness. Therefore, the constant values of  $S$  and  $W$  measured for the ODS 12 Cr steel annealed up to 1473 K agree with the high stability of Y-Ti-O nanoparticles and overall microstructure.

The PADB data measured after annealing at 1573 K shows an increase in  $S$ , but  $W$  is equal to the prior conditions. The position of the  $SW$  pair of the sample annealed at 1573 K is shifted to higher  $S$  at almost constant  $W$  value, in relation to the  $SW$  points of the samples annealed at lower temperatures. The position of the  $S, W$  pair measured for the 14 YWT steel in its as-produced condition seems to form a line with the data measured for the ODS 12 Cr steel (up to 1473 K), with slope  $R = \left| \frac{\Delta S}{\Delta W} \right| \approx 0.88$ . As discussed previously, both steels contain fine Y-Ti-O based nanoparticles. Druzhkov and Perminov [121] showed with the angular-correlation technique (ACAR) that, in an  $SW$  map, the  $SW$  pair of a 14 YWT steel is located forming a line along with the pair measured for pure Ti. The authors also discuss that the main trapping sites for positrons in the 14 YWT are likely O-vacancies, present in the Y-Ti-O nanoparticles, with strong contribution of core electrons of Ti [121]. The results discussed by [121] reinforce the hypothesis that in both ODS 12 Cr steel and 14 YWT steel, the defects contributing the most to the values of  $S$  and  $W$  are the Y-Ti-O based nanoparticles. Additional measurements on annealed 14 YWT and on pure Ti are necessary to confirm if their  $SW$  data in the  $SW$  plot are indeed located along the same line as the data measured for the ODS 12 Cr steel. By considering this hypothesis, it is possible to propose that the change in  $S$  and  $W$ , detected after annealing of the ODS 12 Cr steel at 1573 K, could be related to the trapping of thermal vacancies by the Y-Ti-O nanoparticles, similarly to the discussion for the 0.3%  $Y_2O_3$  ODS Eurofer steel annealed at 1400 K and 1600 K. However, it is not clear why such an increase in  $S$  is not observed on the ODS 12 Cr steel after annealing at 1473 K. The different location of the  $SW$  point of ODS 12 Cr annealed at 1573 K, in relation to ODS Eurofer annealed at 1400 K and 1600 K, is likely correlated to the chemical nature of the Y-O based nanoparticles



and possibly with the role of structural O-vacancies inside the particles as positron trapping sites – detailed studies on the positron affinity to these types of sites are required. Nevertheless, in Chapter 7, the hypothesis of the trapping of thermal vacancies by the oxide particles in ODS 12 Cr steel is further discussed, based on Thermal Desorption Spectroscopy results obtained after exposure of the material to low-energy deuterium plasma, in its as-received condition and annealed at 1573 K.

In relation to the measurements performed on non-ODS materials (FeCr binary alloys, 14 WT and non-ODS Eurofer annealed at different temperatures), the initial objective was to evaluate if the shift in  $SW$  towards lower  $S$  values of the ODS 12 Cr steel was related to the higher Cr content, in comparison to the 0.3%  $Y_2O_3$  ODS Eurofer steel. However, in Figure 6.13, the  $SW$  points measured for the non-ODS alloys are all positioned along the same line ( $R = 0.93$ ), and do not show a correlation with the data measured for the ODS 12 Cr steel. It was discussed in Section 4.1.2, for the non-ODS Eurofer steel, that the observed decrease in  $S$  and increase in  $W$  as a function of annealing temperature is related to the decrease of the concentration of dislocations, interfaces and vacancies due to microstructural processes like recovery, dissolution or precipitation of carbides and formation of martensite. Hence, the same types of defects are considered to be responsible for the  $S$  and  $W$  values measured for the 14 WT steel and FeCr binary alloys. The binary FeCr alloys were produced via powder metallurgy routes and, prior to PADB measurements, were annealed at 1200 K for 1 h. The Fe5Cr alloy becomes fully austenitic when annealed at 1200 K (Figure 6.14) and, in the absence of dispersoids like the oxide nanoparticles, the austenitic grains are able to grow and carriers of deformation introduced during the fabrication process can be annealed out. Upon cooling to room temperature, martensite forms. The formation of martensite is accompanied by an increase of the concentration of dislocations, vacancies and interfaces. Figure 6.13 shows that the overall concentration of defects in the Fe5Cr alloy is equivalent to that of the non-ODS Eurofer annealed at 600 K. The Fe10Cr alloy is likely not fully austenitic during annealing at 1200 K: Figure 6.14 shows that for 10 weight% Cr, in the pure Fe-Cr system, the dual-phase field of austenite and ferrite is approached. Impurities present in the measured Fe10Cr alloy can decrease the size of the austenitic field and, hence, it is likely that a fraction of ferrite is present, leading to a microstructure composed of ferrite and martensite, at room temperature. The lower volume fraction of martensite is responsible for reducing the total concentration of defects in the material and the lower  $S$  and higher  $W$  values seen in Figure 6.13. The Fe14Cr alloy is fully ferritic at all temperature ranges, thus, annealing at 1200 K removes defects introduced during fabrication and, upon cooling, a coarse ferritic microstructure forms.

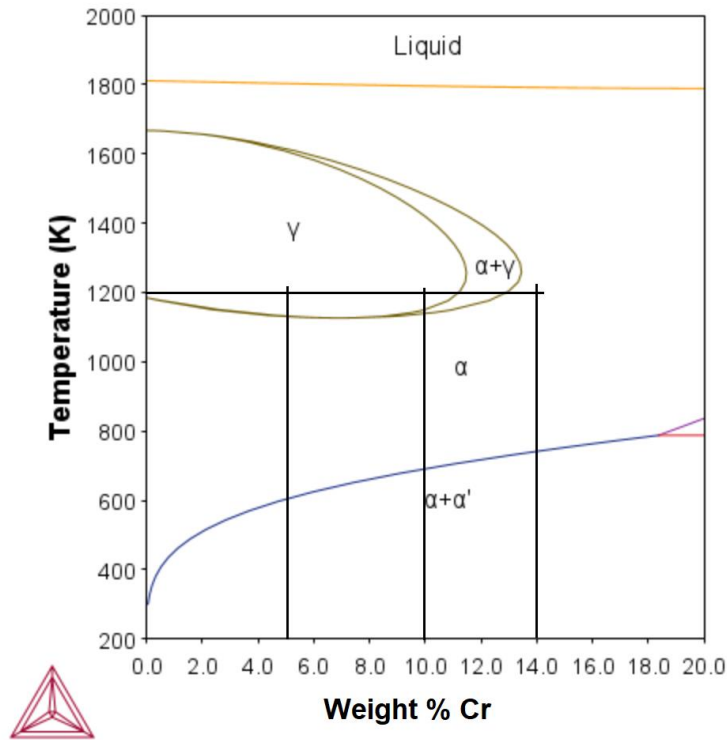


**Figure 6. 14.** Isoleths of Fe-Cr equilibrium diagram calculated with Thermo-Calc v. 2020a.

The 14 WT steel was produced according to the same route as the 14 YWT steel [135] and, because of its Cr content, it also has a ferritic matrix. Due to the presence of other alloying elements, the microstructure of the 14 WT steel is more complex than of the Fe14Cr alloy and, in addition, the former did not undergo any annealing treatment after consolidation by hot isostatic pressing. This results in a higher concentration of defects than the Fe14Cr alloy. Figure 6.13 shows that, in terms of density of defects (dislocations, vacancies associated to deformation, grain boundaries, interfaces of carbides), the 14 WT steel is equivalent to the non-ODS Eurofer steel annealed at 800 K for 1 h (microstructure composed of tempered martensite and  $M_{23}C_6$  carbides).

## 6.5. Conclusions

Different types of ODS steels and non-ODS alloys were measured with Positron Annihilation Doppler Broadening, after 1 h annealing treatments at temperatures ranging from 573 K to 1600 K. The ODS steels, namely 0.3%  $Y_2O_3$  ODS Eurofer, ODS 12 Cr and 14 YWT steels, present  $S$  and  $W$  values that show a high concentration of defects, in agreement with their complex defect structure consisting of high number density of oxide nanoparticles, high

dislocation density (mainly introduced during mechanical alloying) and grain boundary surface area.

The behaviour observed in the annealed 0.3%  $Y_2O_3$  ODS Eurofer steel was different from the ODS 12 Cr steel:

- i) In the 0.3%  $Y_2O_3$  ODS Eurofer steel, annealing up to 1200 K leads to a continuous decrease in the  $S$  value and increase in the  $W$  value, suggesting an overall decrease in defect concentration. This  $SW$  trend is attributed mainly to the recovery of dislocations, initially having a very high density due to severely deformed state introduced during mechanical alloying;
- ii) Despite recrystallization of the microstructure after annealing at 1400 K and 1600 K, PADB measurements of samples in these conditions show an increase in  $S$  and a change in slope of the  $SW$  points. This behaviour is attributed to the formation of thermal-vacancies, which are trapped and stabilized by the Y-O based nanoparticles;
- iii) On the other hand, the  $S$  and  $W$  values measured in the ODS 12 Cr steel do not change significantly with annealing temperature up to 1473 K. In the  $SW$  map, the data measured for the ODS 12 Cr steel is shifted towards lower  $S$  and  $W$  values, in relation to the 0.3%  $Y_2O_3$  ODS Eurofer steel. The 14 YWT steel, in its as-consolidated state, has an  $SW$  point located at the same region as the ODS 12 Cr steel (annealed up to 1473 K). The hypothesis is that Y-Ti-O based nanoparticles, common to both 14 YWT and ODS 12 Cr steels, are the main trapping sites for positron annihilation in the two materials;
- iv) All measurements done on non-ODS alloys show that the positrons are detecting changes in the concentration of microstructural defects like martensite laths, dislocations and vacancies associated to the martensitic transformation, interfaces of precipitates and grain boundaries. The  $SW$  points of all types of non-ODS materials are located along the same line and in a region that represents an overall lower concentration of defects, in comparison to the ODS materials.

## 7. Deuterium behaviour in the ferritic ODS 12 Cr steel

Chapter based on publication:

V.S.M. Pereira, S. Wang, T. Morgan, H. Schut, J. Sietsma. “Microstructural evolution and behaviour of deuterium in a ferritic ODS 12 Cr steel annealed at different temperatures”. *Metallurgical and Materials Transactions A*, v. 53, p. 874-892, 2022, doi: 10.1007/s11661-021-06559-0.

### Abstract

The trapping behaviour of deuterium in the steel in its as-received state and annealed at 1573 K was investigated. Samples were exposed to low-energy deuterium plasma and analysed with Thermal Desorption Spectroscopy, after waiting times of 1 day and 25 days. The samples measured 1 day after exposure released a higher total amount of deuterium than the ones measured after 25 days. The effect of waiting time is explained by the release of deuterium, at 300 K, from sites with low activation energy for detrapping,  $E_d$ . In the as-received condition, part of the deuterium detrapped at 300 K was re-trapped by high- $E_d$  sites. For the samples in the annealed condition, the redistribution of deuterium from low- $E_d$  to high- $E_d$  sites was not observed and the total amount of deuterium released was higher.

**Keywords:** modelling of TDS data, deuterium trapping behaviour, embrittlement

## 7.1. Introduction

The original concept behind the development of ODS steels was actually aimed at increasing the resistance of nuclear structural materials to He-embrittlement, while their higher creep resistance is considered an additional benefit [48], [141]. In nuclear environments, neutrons that impinge metallic structural components can react with the nuclei of lattice atoms, resulting in the transmutation of alloying elements plus formation of He or H [39], [40], [34]. The transmuted element can be radioactive and, hence, compromise the handling and recycling of the structural component at the end of its service life. However, this problem can be tackled by the use of elements in alloy design that go through faster decay of the induced-radioactivity than conventional alloying elements [142], [58]. In fusion reactors, the structural metallic components will also be exposed to D, T, He and H, since they form the plasma in which fusion takes place or are the products of fusion reactions. These elements will diffuse through the metallic structure, being able to recombine and form gas molecules and, when pressure is sufficiently high, bubbles, which are detrimental for the integrity of the component. They can also be trapped at microstructural features of the metal or alloy, such as grain boundaries, interfaces of second-phase particles, dislocations, inclusions, pores. Depending on morphological characteristics of these trapping sites and their distribution throughout the metallic matrix, they can become stress raisers when bound to these elements, leading to embrittlement and fracture during service, or they can be beneficial for increasing the resistance to damage [143]. Since it is not possible to prevent the formation of radiation-induced defects and the generation of He, H, D, T in the metallic structure, the engineering of trapping sites becomes the most suitable approach to improve the resistance to this type of damage and that is how oxide nanoparticles in ODS steels can play their role. These particles can retain the diffusible elements and make them inactive in the material, preventing their recombination or agglomeration at detrimental sites, like grain boundaries (leading to intergranular fracture), regions with microstructural banding, elongated inclusions.

However, it is still unclear how strongly the ODS particles can interact with the different diffusible elements and to what extent ODS steels perform well in nuclear environments. Malitckii et al. [144], [145] have measured with Thermal Desorption Spectroscopy significantly higher contents of H in ODS Eurofer, in comparison to Eurofer, after electrochemical hydrogen charging [22] and exposure to hydrogen plasma [23]. In [144] the authors determined H detrapping activation energies of 0.26 eV and 0.35 eV for the ODS Eurofer steel, at the respective peak temperatures of ~450 K and ~550 K, but without

identifying the type of trapping defects. In contrast, Maroef et al. [146] determined an H detrapping activation energy of 0.73 eV for the interface of  $Y_2O_3$  with ferrite, which does not coincide with detrapping activation energies measured in [144]. Regarding the isotopes of hydrogen, deuterium (D) and tritium (T), it can be considered that they behave in steels in the same way as hydrogen [147], but a more complete characterization of their trapping sites is still missing in the literature. Ogorodnikova et al. [148] measured D retention in several ODS steels and Eurofer, after exposure to  $D_2$  plasma of different energies and at different temperatures. The TDS measurements were carried out months after plasma exposure and showed that the D retention in the ODS materials was always higher than in Eurofer [148]. In a subsequent work, Ogorodnikova et al. [149] performed the same type of analysis in pre-damaged ODS steels and Eurofer, i.e. that were irradiated with 20 MeV W ions prior to exposure to  $D_2$  plasma. The authors [149] observed higher D retention in the pre-damaged samples that were exposed to  $D_2$  plasma at temperatures up to 500 K, but still no details about the sites at which D is dominantly being trapped are discussed [149].

Thus, in the present work the behaviour of deuterium in an ODS 12 Cr steel was investigated. Samples in the as-received condition and annealed at 1573 K for 1 h were exposed to low-energy  $D_2$  plasma and analysed with Thermal Desorption Spectroscopy, in order to study the trapping behaviour of D and its interaction with Y-Ti-O nanoparticles.

## 7.2. Experimental

Samples of the ODS 12 Cr steel in the as-received state and annealed at 1573 K for 1 h were exposed to low-energy deuterium plasma in the Nano-PSI facility, at the Dutch Institute for Fundamental Energy Research (DIFFER), Eindhoven, The Netherlands. The exposure was made in 2 batches; for each batch, a total of four samples with dimensions of  $15 \times 15 \times 1 \text{ mm}^3$  were simultaneously exposed for 2 h to the  $D_2$  plasma with energy of 60 eV. The plasma energy derived almost entirely from a bias voltage of 60 V applied to the substrate holder. The plasma was mainly composed of  $D_3^+$  ions, hence, each D atom impinging the samples had an energy of 20 eV. To minimize back-diffusion of D atoms from the sample, the backside of the samples was kept at room temperature during exposure. Figure 7.1(a) shows the spatial distribution of the ion flux and the electron temperature along a line through the centre of the sample holder. Figure 7.1(b) is a schematic representation of the holder containing the four ODS 12 Cr samples during exposure to the  $D_2$  plasma. The ion flux at the centre of the holder (maximum in Figure

7.1(a)) was approximately  $2.5 \times 10^{20} \text{ m}^{-2}\text{s}^{-1}$  resulting into a maximum ion fluence of  $2.1 \times 10^{24} \text{ m}^{-2}$ .

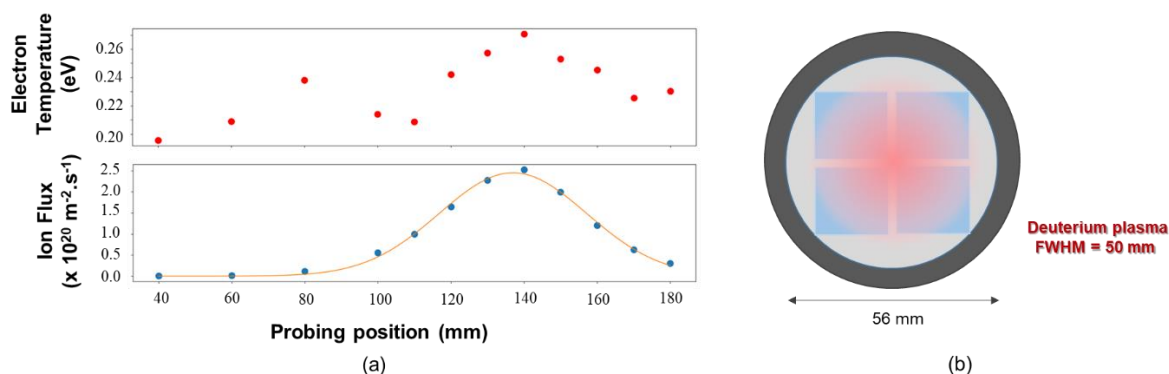


**Figure 7. 1.** (a) Parameters of  $\text{D}_2$  plasma produced in the Nano-PSI at 2 SLM of the gas flow. (b) Schematic representation of the samples in the holder, exposed to  $\text{D}_2$  plasma. The centre of the holder receives the highest flux, the decrease in colour intensity represents the radial gradient of plasma fluence.

After exposure, the samples were submitted to Thermal Desorption Spectroscopy (TDS), in order to determine the content of D retained in the steel and its trapping characteristics. One batch of samples was stored for 1 day at room temperature in a desiccator prior to the TDS measurement, another batch was stored for 25 days. In the TDS measurement, the samples were heated at a rate of  $2 \text{ K}\cdot\text{s}^{-1}$  from room temperature to 1200 K, which is the maximum temperature reached by the TDS. The initial pressure inside the TDS sample chamber was  $3 \times 10^{-7}$  mbar, however, when the system was at 1200 K, the pressure had increased to  $10^{-5}$  mbar. The sample temperature was measured with a thermocouple welded to its surface and, to improve the thermal contact, graphite foils were inserted between the sample and the holder.

### 7.3. Analysis and Modelling of Thermal Desorption Spectroscopy Data

The D atoms introduced in the metallic structure during exposure to  $\text{D}_2$  plasma can occupy normal lattice sites (interstitial positions), or trapping sites (defects). When located in a normal lattice site, the potential of the D atom is higher than at a trapping site and, hence, the latter forms a preferential site for D occupation. Both diffusion of D through the lattice and detrapping from a site require thermal activation. The activation energy for D diffusion through interstitial sites in  $\alpha$ -Fe has been experimentally determined by Hagi and Hayashi [150] at  $9 \text{ kJ}\cdot\text{mol}^{-1}$  (0.09 eV), very similar to the activation energy for hydrogen diffusion ( $8 \text{ kJ}\cdot\text{mol}^{-1}$ ,

0.08 eV), and is considerably lower than the detrapping activation energy from trapping sites like dislocations, which has been determined by different authors to be 27 kJ.mol<sup>-1</sup> (0.28 eV) [150], [151].

During a Thermal Desorption Spectroscopy measurement, the heating of a sample at a constant rate gradually provides the required thermal energy for the release of D atoms from the different sites. Each peak of maximum desorption rate in a TDS spectrum can be correlated with the release of D atoms from specific trapping sites in the material, however [151], [152], however, such a correlation is not straightforward, since the peak position depends on experimental parameters like the heating rate. Several models have been developed to describe the diffusion and trapping behaviour of hydrogen in metals [153], [154], [155], which can be used to analyse TDS spectra and calculate kinetic parameters involved in hydrogen and deuterium evolution, especially when diffusion is the rate controlling process. For cases in which detrapping is the rate controlling process, the Kissinger theory of reaction kinetics [156], [157] can be applied to TDS data, as first proposed by Choo and Lee [151] and later by Wei et al. [152], [158], [159]. Wei et al. [152], [158], [159] have shown that it is possible to obtain the activation energy for detrapping  $E_d$  by performing a numerical fit of the different maxima in a single TDS curve, using the Kissinger reaction rate equation

$$\frac{dX}{dt} = A(1 - X)^n \exp\left\{\frac{-E_d}{RT}\right\} \quad (7.1)$$

Here  $\frac{dX}{dt}$  is the release rate,  $A$  is a constant,  $X$  is the fraction of atoms released,  $n$  is the empirical reaction order,  $R$  is the gas constant and  $T$  is the temperature. Originally, the constant  $A$  is known as the frequency factor and represents the probability of a molecule to participate in a chemical reaction [157]. When describing the detrapping-controlled desorption of hydrogen, Wei et al. [159] suggested that  $A$  approaches the pre-exponential factor  $p^0$  in the McNabb and Foster theory [153], [159]).

In the present work, an approach similar to the one of Wei et al. is used to estimate  $E_d$  of the different trapping sites present in the ODS 12 Cr steel. The fitting of the data is based on considering the experimentally measured TDS spectra to be the sum of several individual peaks. Each peak was modelled using a slightly modified version of Equation 7.1, with  $n = 1$  (i.e. retrapping and diffusion are not considered [152], [158], [159]), given by



$$\frac{dN}{dt} = AN \exp \left\{ \frac{-E_d}{kT} \right\} \quad (7.2)$$

where  $\frac{dN}{dt}$  is the deuterium release rate in atoms.s<sup>-1</sup> and  $N$  is the number of D atoms in the trapping site. Since we report  $E_d$  in the unit eV, the Boltzmann constant  $k$  is used. The amount of D released in a time interval  $\Delta t$  is obtained by iteratively solving Equation 7.2 with the initial condition  $N(t=0) = N_0$  and

$$N(t + \Delta t) - N(t) = \Delta t \left( \frac{dN}{dt} \right) \quad (7.3)$$

The initial value  $N_0$  is treated as a fitting parameter.

The experimental heating rate of 2 K.s<sup>-1</sup> was introduced in the model by taking a temperature step of 0.2 K for every sufficiently small time step of 0.1 s.

#### 7.4. Results and Discussion

The conditions selected for exposure of the ODS 12 Cr steel to low-energy D<sub>2</sub> plasma and subsequent Thermal Desorption Spectroscopy were the as-received condition and annealed at 1573 K for 1 h. The main objective was to investigate the trapping behaviour of deuterium in the material, particularly after the 1573 K annealing treatment, during which the coarsening of Y-Ti-O nanoparticles has occurred (Chapter 5). In Chapter 6, the thermal evolution of defects in the ODS 12 Cr and the 0.3% Y<sub>2</sub>O<sub>3</sub> ODS Eurofer steel was studied with Positron Annihilation Doppler Broadening. The results suggest that, during annealing at temperatures between 1400 K and 1600 K, thermal vacancies become trapped at the interfaces of Y-O based nanoparticles and, thus, are retained in the microstructure upon cooling to room temperature. This hypothesis is further explored in the present Chapter.

Figure 7.2 presents the spectra of deuterium desorption rate *vs* temperature, obtained 1 day and 25 days after exposure to 60 eV D<sub>2</sub> plasma. The batch of samples measured 1 day after plasma exposure are named here as “AS-1 and 1573 K-1” and the batch measured 25 days after plasma exposure is referred to as “AS-25 and 1573 K-25”. Table 7.1 summarizes the total amount of deuterium atoms released per sample, calculated by integrating the desorption curves.

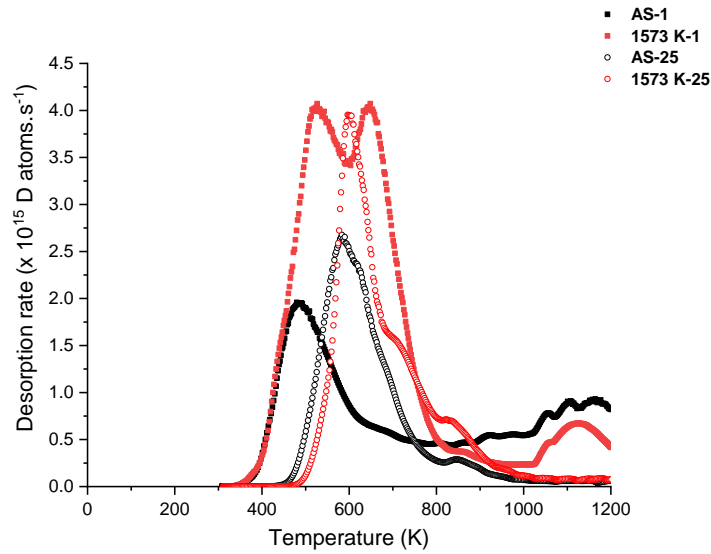


**Figure 7. 2.** TDS spectra measured on ODS 12 Cr steel samples in the as-received and annealed at 1573 K conditions. The samples were measured with TDS 1 day and 25 days after exposure to 60 eV D<sub>2</sub> plasma.

**Table 7. 1.** Total amount of deuterium atoms released from ODS 12 Cr steel samples at different conditions, 1 day and 25 days after exposure to D<sub>2</sub> plasma.

	AS-1	1573 K-1	AS-25	1573 K-25
Deuterium atoms released	$3.17 \times 10^{17}$	$6.35 \times 10^{17}$	$2.25 \times 10^{17}$	$2.97 \times 10^{17}$

The data presented in Figure 7.2 and Table 7.1 show that the samples annealed at 1573 K released more D than the samples in the as-received condition, by a factor of 2.0 after 1 day and a factor of 1.3 after 25 days. Additionally, an effect of the waiting time prior to TDS can be seen, as samples measured 1 day after plasma exposure also released a higher number of D atoms than the ones measured 25 days after exposure, by a factor of 1.4 for the as-received condition and a factor of 2.1 for the annealed condition. First, the effect of waiting time will be explored.

### 7.4.1. The effect of waiting time

It is possible to estimate the time for D atoms to diffuse out of the samples, using the expression of diffusion length

$$x = \sqrt{2Dt} \quad (7.4)$$

where  $x$  is the diffusion length, which is taken here as the half-thickness of the sample ( $x = 0.75$  mm),  $D$  is the diffusion coefficient of D in the material and  $t$  is the time for D atoms to diffuse to the exit surface of the sample.

The D atoms have to diffuse through a structure with a high density of defects (grain boundaries, dislocations, TiC, Y-Ti-O nanoparticles) thus, the value for  $D$  actually corresponds to an effective diffusion coefficient,  $D_{eff}$ . Esteban et al. [147], using the gas permeation method, obtained the Arrhenius parameters for the effective diffusion of H in ODS Eurofer:  $D_0 = 1.33 \times 10^{-6} \text{ m}^2 \cdot \text{s}^{-1}$  and  $E_{dif} = 30.4 \text{ kJ} \cdot \text{mol}^{-1}$  (activation energy for diffusion). Since ODS 12 Cr and ODS Eurofer steels have a similar defect density and, as discussed previously, it is considered that H and D have the same behaviour in steels, we used the parameters determined by [147] to calculate  $D_{eff}$  for D in the ODS 12 Cr steel at different temperatures. Finally, the  $D_{eff}$  values were used in Equation 7.4 and the time for D atoms to diffuse out of the samples was obtained as a function of temperature. At room temperature (300 K),  $D_{eff} = 6.8 \times 10^{-12} \text{ m}^2 \cdot \text{s}^{-1}$  and  $t = 41500$  s, or 11.5 h; at higher temperatures  $t$  is reduced to tens of seconds, for example, at 600 K  $t$  is 93 s and at 800 K  $t$  is 20 s. Hence, even after 1 day the samples may have already lost a fraction of mobile D prior to the TDS measurement, just by being kept at room temperature, confirming the release of D during the waiting time of 25 days. This confirms the observed loss of D during the waiting time of 25 days.

In order to investigate in more details the release of D at 300 K, it is necessary to determine the activation energies for detrapping,  $E_d$ , associated to the desorption peaks.

Figures 7.3(a) and 7.3(b) show the modelling of TDS spectra of the samples AS-1 and AS-25, done with the use of Equation 7.2. As stated before, Equation 7.2 does not consider re-trapping and assumes that diffusion of D is fast in comparison to the de-trapping rate. In addition, when at the maximum of the desorption peak, the number of atoms of D still residing at the specific trapping site corresponds to 40 % of its initial concentration  $N_0$  ( $0.4N_0$ ). Thus, by integration of Equation 7.2, at a constant temperature, the time for reaching the state  $N = 0.4N_0$  is given by

$$t_{40\%,300K} = \frac{-\ln(0.4)}{A \exp\left(\frac{-E_d}{kT}\right)} \quad (7.5)$$

The values of  $A$ ,  $E_d$ ,  $N_0$  and  $t_{40\%,300K}$  are given in Table 7.2.

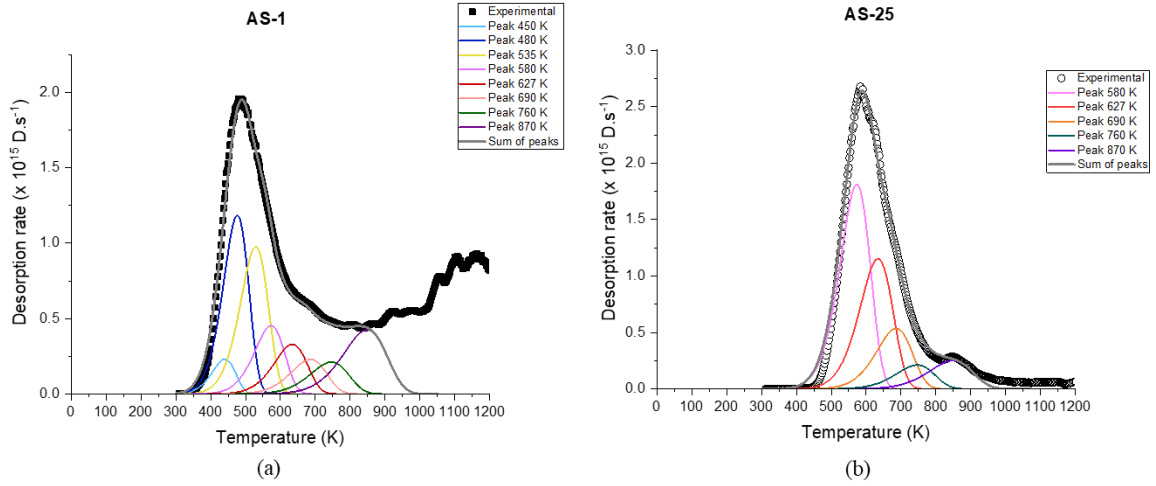


**Figure 7.3.** Modelling of TDS spectra obtained for ODS 12 Cr steel samples (a) AS-1, measured 1 day after  $D_2$  exposure and (b) AS-25, measured 25 days after exposure.

**Table 7.2.** Parameters used in the modified Kissinger equation (Equation 7.2) for modelling TDS spectra of ODS 12 Cr steel in the as-received condition and the estimated time for depletion of trapping sites at 300 K.

Peak Temperature (K)	$E_d$ (eV)	$A$ ( $10^4$ s $^{-1}$ )	AS-1	AS-25	$t_{40\%, 300 K}$ (days)
			$N_0$ ( $10^{16}$ D atoms)	$N_0$ ( $10^{16}$ D atoms)	
450	0.50	2.5	1.0	0	0.1
480	0.50	1	5.5	0	0.3
535	0.56	1	5.0	0	3
580	0.61	1	2.5	10.0	19
627	0.68	1	2.0	7.0	282
690	0.74	1	1.7	3.5	$2.9 \times 10^3$
760	0.81	1	1.5	1.5	$43 \times 10^3$
870	0.93	1	3.5	2.0	$4.5 \times 10^6$

The types of trapping sites present in samples AS-1 and AS-25 are expected to be the same, since the only difference between the two samples is the waiting time, at room temperature, to the TDS measurement. Therefore, the  $E_d$  values used in the modelling are equal for both samples. The amount of D atoms  $N_0$  initially trapped at each type of defect is different and only for the modelled peak at 450 K the constant  $A = 2.5 \times 10^4$  s $^{-1}$ ; for the others,  $A = 10^4$  s $^{-1}$ .

In Figure 7.3(a), the experimental spectrum AS-1 has a dominant desorption peak at 480 K, which cannot be modelled with a single spectrum. In order to reproduce its slope and overall shape, it is necessary to adopt an approach of multiple traps. The experimental peak at 480 K is, then, considered to be the result of desorption from different trapping sites with  $E_d$  0.50 eV and 0.56 eV and peaks at 450 K, 480 K and 535 K. The  $E_d$  and  $A$  values of the modelled peaks at 450 K and 480 K suggests that these two peaks occur because of the release of D from the same type of defect, but in a first stage at 450 K desorption could be easier [158]. This choice of  $E_d$  and  $A$  for modelling the peaks at 450 K and 480 K is based on the number of defects detected during microstructural characterization: we aimed at consistency between modelling of TDS data and the microstructural observations. The only peak that was adequately modelled by a single spectrum was the one at 870 K in AS-25.

In Figure 7.3(b), the first desorption peak in the experimental spectrum of AS-25 is around 580 K, and the lower temperature peaks at 450 K, 480 K and 535 K are absent, suggesting the depletion of these traps. The values of  $t_{40\%,300\text{ K}}$  displayed in Table 7.2 confirm this suggestion, as these lower temperature peaks are the only ones that can become fully depleted after 25 days at 300 K. Thus, in the modelling of AS-25,  $N_0$  for these trapping sites is zero. Additionally, the modelling of AS-25 shows the increase of  $N_0$  for trapping sites with  $E_d = 0.61$  eV, 0.68 eV and 0.74 eV, suggesting the redistribution of D from lower to higher  $E_d$  sites.

The desorption peaks at temperatures above 900 K in the AS-1 and 1573 K-1 experimental spectra were not modelled, as they are believed to be caused by an increase in background pressure.

The same analysis was made for the samples 1573 K-1 and 1573 K-25 and the results are given in Figure 7.4 and Table 7.3.

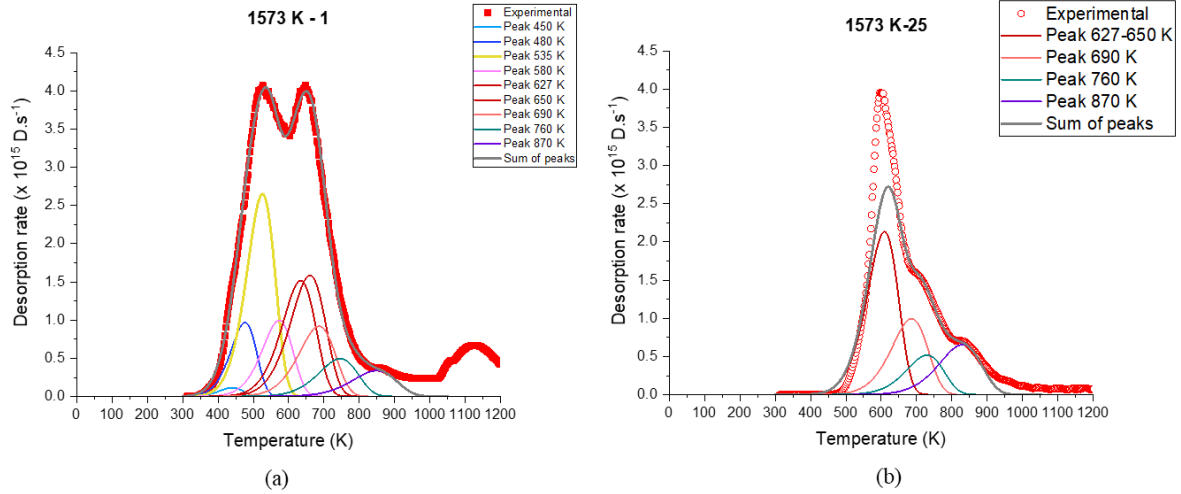


**Figure 7. 4.** Fitting of TDS spectra obtained for ODS 12 Cr steel samples (a) 1573 K-1, measured 1 day after  $D_2$  exposure and (b) 1573 K-25, measured 25 days after exposure.

**Table 7. 3.** Parameters used in the modified Kissinger equation (Equation 7.2) for fitting TDS spectra of the ODS 12 Cr steel in the condition annealed at 1573 K, measured 1 day (1573 K-1) and 25 days (1573 K-25) after exposure to  $D_2$  plasma.

1573 K-1				1573 K-25			
Peak Temperature (K)	$A$ ( $10^4 s^{-1}$ )	$E_d$ (eV)	$N_0$ ( $10^{16}$ D atoms)	Peak Temperature (K)	$A$ ( $10^4 s^{-1}$ )	$E_d$ (eV)	$N_0$ ( $10^{16}$ D atoms)
450	2.5	0.50	0.5	450	2.5	0.50	0
480	1	0.50	4.5	480	1	0.50	0
535	1	0.56	13.3	535	1	0.56	0
580	1	0.61	5.5	580	Not fitted	Not fitted	Not fitted
627	1	0.68	9.2	627-650	1.8	0.68	12.0
650	0.6	0.68	10.0				
690	1	0.74	6.0	690	1	0.74	6.5
760	1	0.81	3.5	760	1	0.81	3.5
870	1	0.93	2.7	870	1.4	0.93	5.0

The same modelling parameters used in AS-1 and AS-25 were applied to 1573 K-1, with the addition of an extra peak at 650 K, present in its experimental spectrum (Figure 7.4(a)). The peak at 650 K can be modelled with the combination of  $E_d = 0.68$  eV and  $A = 0.6 \times 10^{-4} s^{-1}$ . This choice suggests that the modelled peaks at 627 K and 650 K belong to the same type of defect, but with desorption occurring in two stages, similarly to the proposed for the modelled peaks at 450 K and 480 K in AS-1 and 1573 K-1 [158].

In Figure 7.4(b), the peaks associated to lower- $E_d$  sites are again not present because of their depletion after the 25 days waiting time. Nevertheless, the D desorption behaviour in sample 1573 K-25 is more complex and could not be modelled completely. The peak at 580 K in AS-25 is shifted to 600 K in 1573 K-25, and cannot be modelled with Equation 7.2. The remaining high temperature peaks are also shifted in comparison to 1573 K-1, AS-1 and AS-

25, but it was possible to model these by using the same  $E_d$  values as for the other conditions and altering the value of  $A$ . In order to estimate  $N_0$  of the peak at 580-600 K in 1573 K-25, the area of the modelled peaks was subtracted from the experimental 1573 K-25 spectrum. The result is  $N_0 = 4 \times 10^{16}$  atoms, a value similar to the one in 1573 K-1, and an indication that redistribution of D from shallower traps to deeper ones does not occur. The  $N_0$  value of the peak at 627-650 K is also considerably lower in 1573 K-25, corresponding to 63% of  $N_0$  of the same peaks in 1573 K-1.

#### **7.4.2. Effect of annealing at 1573 K**

It is clear that the annealing treatment at 1573 K for 1 h has an effect on the trapping and desorption behaviour of D in the ODS 12 Cr steel, seen in Table 7.1 as the higher amount of D atoms released, the extra desorption peak at 650 K in 1573 K-1 and the change in the constant  $A$  used to partially model the 1573 K-25 spectrum. The Electron Microscopy analyses of the microstructure and of Y-Ti-O nanoparticles discussed in Chapter 5 show that the ODS 12 Cr steel contains many different defects: ferrite grain boundaries, dislocations, micrometric TiC, coherent Y-Ti-O nanoparticles (particle size smaller than 4.5 nm), semi-coherent Y-Ti-O nanoparticles (particle size between 4.5 and 10 nm), incoherent Y-Ti-O nanoparticles (particle size higher than 10 nm), coarse Y-Ti-O based particles (located at pores and with average size ranging from ~200 nm to 1  $\mu$ m) and pores. The as-received microstructure is only altered after annealing at the high temperature 1573 K, when an increase in the average Y-Ti-O particle size to ~ 7 nm and partial recrystallization are observed. These microstructural alterations would imply an overall lower density of defects, but, nevertheless, the deuterium intake was higher.

Possible explanations for the higher deuterium intake by the samples in the annealed condition are: (1) the more abundant semi-coherent and incoherent Y-Ti-O nanoparticles are able to trap more D atoms and (2) the annealing treatment at 1573 K leads to the trapping of thermal vacancies at the interfaces of Y-Ti-O nanoparticles and the coarse Y-Ti-O particles, thereby increasing the content of trapped D.

Hypothesis (1) could explain the broad peak at 650 K in the TDS curve of 1573 K-1. As discussed in 7.4.1. this peak was modelled by a multiple trap approach, in which the peaks at 627 K and 650 K, both, have  $E_d = 0.68$  eV. The  $N_0$  value of these two peaks corresponds to  $2 \times 10^{17}$  atoms (Table 7.3), one order of magnitude higher than the  $N_0$  of the modelled peak at 627 K in AS-1 (Table 7.2), and thus could be associated with the higher fraction of semi-coherent/incoherent Y-Ti-O nanoparticles. However, hypothesis (1) cannot explain the

experimental TDS spectrum of 1573 K-25. If hypothesis (1) was indeed valid, it would be possible to model all other high temperature peaks in 1573 K-25 with the same  $E_d$  and  $A$  parameters used in the other conditions, only changing their respective  $N_0$  values. Instead, the required different  $A$  values in the modelling of 1573 K-25 signalizes modifications of the other high energy sites and likely a change in the desorption mode of D. Hence, hypothesis (2) could be the reason for this observed behaviour. After exposure to plasma, D atoms could be initially trapped both at the interface of the oxide/vacancy clusters and inside the vacancy clusters. When the size of the vacancy cluster is large enough, the trapped D atoms can form  $D_2$  molecules, which will have a desorption mechanism different from the  $D^+$  state. After the 25 days waiting time, most part of D would be trapped in the form of  $D_2$ , leading to the observed different desorption kinetics. According to [107], first-principles studies have shown that oxygen-vacancies complexes in Y-Ti-O nanoclusters are not able to trap a high number of hydrogen atoms, because the oxygen atoms absorb most of the charge density supplied by surrounding iron atoms [107]. This could also explain why the D redistribution described for AS-1 and AS-25 does not occur in 1573 K-1 and 1573 K-25. In case hypothesis (2) is confirmed, the complexes of thermal vacancies and Y-Ti-O nanoparticles are able to trap more D than the particles alone, but they could have become saturated during exposure.

Because of the complexity of the microstructure, its high thermal stability (heat treatments do not lead to easily detectable microstructural alterations) and a limited TDS data set, it is not possible to reliably determine to which type of defect each modelled desorption peak in Figures 7.3 and 7.4 correspond to, although, there is a correspondence between the number of identified defects and the number of peaks necessary to model the experimental TDS spectra.

Additional TDS measurements done at different heating rates and first-principles calculations are necessary to further explore hypothesis (2), related to the behaviour of D in the ODS 12 Cr steel annealed at 1573 K, and to characterize completely the trapping sites present in the material.



### 7.4.3. Evaluation of the modified Kissinger method for modelling TDS data

Finally, we used TMAP7 simulations [160], [161] to evaluate the use of Equation 7.2 and, particularly, the choice of  $A$  values for modelling the experimental TDS data. In the original Kissinger's theory the constant  $A$  represents the probability of a molecule to participate in a chemical reaction [157]. Hence, in a desorption experiment the constant  $A$  can be seen as the probability of a deuterium atom to be desorbed from a trapping site. For a desorption process governed by detrapping,  $A$  approaches the pre-exponential factor  $p^0$  [159] in the probability  $p$  of release from a trapping site to a lattice site [153], [159]. In TMAP7,  $p^0$  is determined as the Debye frequency  $\nu_0$  ( $\sim 10^{13} \text{ s}^{-1}$ ).

In case we take  $A = \nu_0$  in Equation 7.2, for modelling the peak at 450 K, for example, the corresponding  $E_d$  becomes 1.3 eV. A good mathematical correspondence with TMAP7 is obtained when we take  $E_d = 1.3 \text{ eV}$  and the diffusion parameters  $D_0$  and  $E_{dif}$  as, respectively,  $2.1 \text{ m}^2 \cdot \text{s}^{-1}$  and 0.1 eV. These values of  $D_0$  and  $E_{dif}$  again represent a first order, detrapping-controlled desorption reaction. However, the very high value of  $E_d$  strongly disagrees with the disappearance after 25 days of the low temperature desorption peaks observed in samples AS-25 and 1573 K-25. To investigate the effect of diffusion on the position of the desorption peaks, TMAP7 simulations were carried out using the lattice diffusion parameters of D in pure  $\alpha$ -Fe [150] ( $D_0 = 2 \times 10^{-7} \text{ m}^2 \cdot \text{s}^{-1}$  and  $E_{dif} = 0.1 \text{ eV}$ ), the assumption of  $A = \nu_0$ ,  $E_d = 1.3 \text{ eV}$  and lower  $E_d$  values listed in Table 7.2, in order to reproduce AS-1. For  $E_d = 1.3 \text{ eV}$ , the result is a peak at 850 K; for the lower  $E_d$  values, a peak with the same shape and slope as the experimental AS-1 is obtained, but shifted to 380 K.

Nevertheless, the TMAP7 simulations performed with different diffusivities show that Equation 7.2 and our choice of  $A$  values much lower than the Debye frequency are appropriate to model the TDS experimental data obtained for the ODS 12 Cr steel. A possible underlying physical reason for  $A$  being smaller than  $\nu_0$  is the effect of the entropy in the activation free energy. However, within the framework of the present study it is not possible to quantify this effect.

## 7.5. Conclusions

The subsequent exposure to low-energy D<sub>2</sub> plasma of samples in the as-received and annealed at 1573 K conditions, followed by TDS measurements show the following behaviour of deuterium:

- i) During the waiting time of 25 days, at 300 K, D atoms initially trapped at low energy sites ( $E_d = 0.50, 0.56$  and  $0.61$  eV) are detrapped. It was observed in the as-received condition that part of the detrapped D is released from the material and part of it is redistributed to higher energy trapping sites. For the annealed condition, we only find evidence of release of the detrapped D atoms, without occurrence of redistribution to higher energy trapping sites.
- ii) Prior annealing at 1573 K for 1 h increases the D uptake during exposure to low-energy D<sub>2</sub> plasma. The reason for this behaviour is still not completely clear, but the hypothesis is that, during annealing, thermal vacancies are trapped by the Y-Ti-O particles (nanoparticles and even the coarser ones). The complexes of thermal vacancies and Y-Ti-O based particles are able to trap a higher number of D atoms, which can form D<sub>2</sub> molecules inside the vacancies. The fact that no redistribution of D during the waiting time is observed for the annealed condition implies that the complexes of thermal vacancies + Y-Ti-O particles become saturated with D after plasma exposure.
- iii) Additional TDS measurements at different heating rates and the use of first-principle calculations are necessary to properly characterize the trapping sites in the ODS 12 Cr steel and to further understand the D behaviour in the annealed condition.

## 8. General conclusions and recommendations

### 8.1. General conclusions

The research presented in this PhD thesis has a fundamental character, aiming to generate knowledge of the relationship between annealing conditions, microstructure, phase transformations and oxide nanoparticles, and also to better understand how defects intrinsic to ODS steels and defects created during high temperature treatments and during exposure to low-energy deuterium plasma interact with the oxide nanoparticles. These aspects are investigated with the use of different, yet complementary techniques, able to evaluate materials in different scales. Vickers hardness, here in a level closer to the macroscopic because of the magnitude of load used, gives information about strengthening mechanisms in the steels and aids in the investigation of phase transformations. SEM and EBSD are able to give information at the mesoscale level about the microstructure, allowing the determination of grain size distributions, characterization of micrometric constituents present in the steels, investigation of phase transformations, recovery (EBSD) and occurrence of recrystallization. TEM and APT have the resolution necessary for observation of the Y-O based nanoparticles and determination of their chemical compositions. PADB, sensitive to defects in the nanometre and atomic scales, is able to further inform on microstructural processes of the material, on the thermal evolution of defects and their interaction with Y-O based nanoparticles. TDS is able to inform on the behaviour of deuterium in ODS steels and to support PADB observations related to the interaction of Y-O based nanoparticles with defects.

The thermal stability of two different ODS steels is analysed: 0.3%  $Y_2O_3$  ODS Eurofer and ODS 12 Cr. Both steels contain 0.3 weight%  $Y_2O_3$ , but their chemical compositions and consolidation methods used during their fabrication were different. The nominal composition of the 0.3%  $Y_2O_3$  ODS Eurofer steel is Fe-0.1C-9Cr-1W-0.2V-0.18Y (in weight %), its consolidation method was hot isostatic pressing. The composition of the ODS 12 Cr is Fe-0.03C-12Cr-1.7W-0.3Ti-0.14Y (in weight %) and its consolidation method was hot extrusion. These differences in alloy design and fabrication method are responsible for the different types of microstructures that have formed, final chemical composition of oxide nanoparticles and, consequently, for the different high-temperature behaviour of the materials.

The 0.3%  $Y_2O_3$  ODS Eurofer steel has, in its reference state, an isotropic microstructure, composed of tempered martensite, residual ferrite and  $M_{23}C_6$  carbides. The ODS 12 Cr steel does not form austenite at high temperatures and, therefore, its matrix is

always ferritic, with TiC carbides forming along grain boundaries. Because of consolidation by hot extrusion, the ferritic grains in the ODS 12 Cr steel are elongated and present  $\langle 110 \rangle \alpha$ -fibre texture.

In the 0.3%  $Y_2O_3$  ODS Eurofer steel, the oxide nanoparticles are composed of Y, V and O; in the ODS 12 Cr steel, nanoparticles are Y, Ti, O based. The addition of Ti is known to reduce the final oxide nanoparticle size and confers higher thermal stability to the particles. When the oxide nanoparticles remain refined at high temperatures, the Zener pinning force exerted by them also remains strong and the overall microstructure does not become coarser during exposure to elevated temperatures. These effects have been shown in Chapters 3, 4 and 5. The Y-V-O based nanoparticles in the 0.3%  $Y_2O_3$  ODS Eurofer steel undergo coarsening during annealing at 1400 K, which leads to the formation of a coarser microstructure upon cooling to room temperature and reduction of the Vickers hardness. In the ODS 12 Cr steel, a fraction of the Y-Ti-O nanoparticles become coarser only after 1 h annealing at 1573 K, which leads to a moderate degree of softening of the material. It is worth mentioning that the resistance to recrystallization of the ODS 12 Cr steel is partly due to the formation of the  $\langle 110 \rangle \alpha$ -fibre texture, which causes an intrinsically low driving force for recrystallization.

For the abovementioned reasons, the overall thermal stability of the ODS 12 Cr steel is superior to that of the 0.3%  $Y_2O_3$  Eurofer steel, but its strong grain elongation also leads to anisotropy of mechanical properties. The addition of Ti as alloying element is of great importance for the increase in thermal stability, but the use of hot extrusion as consolidation method, especially in the case of a ferritic matrix, is not beneficial. ODS steels have a great potential for high-temperature application, but their fabrication method needs to be optimized in order to allow their commercial availability.

In Chapter 6, Positron Annihilation Doppler Broadening (PADB) analyses have shown that ODS steels contain an overall high density of defects. The concentration of defects remains higher than in non-ODS materials even after annealing at temperatures above 1200 K. This aspect is due to the high deformation state of ODS steels, caused by mechanical alloying, and due to the presence of a high number density of oxide nanoparticles. The latter, besides providing their interfaces with the Fe-matrix and structural vacancies as trapping sites for positrons, also pin dislocations, making recovery more difficult than in non-ODS alloys.

PADB results suggest that the oxide nanoparticles are able to trap thermal vacancies, formed in high concentrations during annealing at temperatures of 1400 K and above. The excess of thermal vacancies, trapped by the oxide nanoparticles, is retained in the microstructure upon cooling to room temperature. The Thermal Desorption Spectroscopy

(TDS) results discussed in Chapter 7 support this hypothesis. The ODS 12 Cr steel, in its as-received condition and after annealing at 1573 K for 1 h, was submitted to low-energy deuterium plasma and then measured with TDS. The deuterium uptake in the annealed condition was higher than that in the as-received state. This could be related to the prior trapping of thermal vacancies by oxide nanoparticles, which would be able to accommodate more deuterium atoms. Still, more experiments are needed in order to confirm this effect. The ability of accommodating more deuterium atoms (or hydrogen, or helium, or other radiation-induced defects) could have positive effects on the performance of the steel during service, but mechanical testing and further investigations are necessary.

## **8.2. Recommendations for future research**

The hypothesis of oxide nanoparticles trapping thermal vacancies, formed in high concentration during high-temperature annealing, which resulted from the PADB (Positron Annihilation Doppler Broadening) and TDS (Thermal Desorption Spectroscopy) studies performed in the 0.3%  $Y_2O_3$  ODS Eurofer and ODS 12 Cr steels can be of technological interest. By associating thermal vacancies to their interfaces, the oxide nanoparticles are able to accommodate more radiation-induced defects, preventing their deleterious effects on mechanical properties. However, first it is necessary to generate additional confirmation for this hypothesis. In order to do so, the following experiments are suggested for future research:

- 1) Positron Annihilation Lifetime Spectroscopy (PALS) analysis of both ODS steels, annealed at temperatures in the range of 600 K to 1600 K. The Lifetime technique is essential to complement the results obtained with PABD, as it determines the lifetimes of positrons trapped at different defects and is able to provide information about their structures and sizes.
- 2) Annealing treatments of a non-ODS 12 Cr steel, with the same microstructure as the ODS 12 Cr steel, but without the presence of oxide nanoparticles. Subsequently, using Thermal Desorption Spectroscopy, investigation of the deuterium uptake by the non-ODS 12 Cr steel in the different annealed conditions. In this way, the role of other microstructural features, like TiC carbides, on the trapping of deuterium atoms can be evaluated.

- 3) Exposure of the ODS 12 Cr steel to high-energy deuterium plasma, before and after high-temperature treatments. Exposure to high-energy plasma will lead to the formation of vacancies and self-interstitials, besides introducing deuterium in the material. Subsequent analysis of the defects formed can be performed with PALS, PADB and TDS.
- 4) First principles studies (*ab initio*, DFT calculations) can be carried out in order to understand how deuterium (or hydrogen, or helium) bind to oxide nanoparticles.
- 5) Mechanical testing of ODS steels, in annealed and as-received conditions, prior and after exposure to deuterium plasma. In this way, it will be possible to evaluate the effect of higher deuterium uptake on the mechanical properties (use of miniature specimens, small punch testing, hardness measurements).
- 6) It is of fundamental interest to understand the coarsening mechanism of oxide nanoparticles, however, such investigation is complex. A highly refined characterization of the core-shell structure of oxide nanoparticles, before and after high-temperature annealing treatments, can give insight into the diffusion of elemental components that drive coarsening. Atom Probe Tomography and advanced techniques of Transmission Electron Microscopy can be used. The 0.3% Y<sub>2</sub>O<sub>3</sub> ODS Eurofer steel studied in the present thesis presents lower thermal stability than other ODS Eurofer steels reported in the literature. The early coarsening of its Y-V-O nanoparticles could be related to the lack of tantalum in the material and, hence, the effect on tantalum should also be investigated.



- 225–234, 2017, doi: 10.1016/j.rser.2016.09.031.
- [13] B. Yu, L. Xu, and Z. Yang, “Ecological compensation for inundated habitats in hydropower developments based on carbon stock balance,” *J. Clean. Prod.*, vol. 114, pp. 334–342, 2016, doi: 10.1016/j.jclepro.2015.07.071.
- [14] N. Y. Amponsah, M. Trolborg, B. Kington, I. Aalders, and R. L. Hough, “Greenhouse gas emissions from renewable energy sources: A review of lifecycle considerations,” *Renew. Sustain. Energy Rev.*, vol. 39, pp. 461–475, 2014, doi: 10.1016/j.rser.2014.07.087.
- [15] R. Turconi, A. Boldrin, and T. Astrup, “Life cycle assessment (LCA) of electricity generation technologies: Overview, comparability and limitations,” *Renew. Sustain. Energy Rev.*, vol. 28, pp. 555–565, 2013, doi: 10.1016/j.rser.2013.08.013.
- [16] K. Li, H. Bian, C. Liu, D. Zhang, and Y. Yang, “Comparison of geothermal with solar and wind power generation systems,” *Renew. Sustain. Energy Rev.*, vol. 42, pp. 1464–1474, 2015, doi: 10.1016/j.rser.2014.10.049.
- [17] O. Ellabban, H. Abu-Rub, and F. Blaabjerg, “Renewable energy resources: Current status, future prospects and their enabling technology,” *Renew. Sustain. Energy Rev.*, vol. 39, pp. 748–764, 2014, doi: 10.1016/j.rser.2014.07.113.
- [18] V. V. Tyagi, N. A. A. Rahim, N. A. Rahim, and J. A. L. Selvaraj, “Progress in solar PV technology: Research and achievement,” *Renew. Sustain. Energy Rev.*, vol. 20, pp. 443–461, 2013, doi: 10.1016/j.rser.2012.09.028.
- [19] S. V. Vassilev, C. G. Vassileva, and V. S. Vassilev, “Advantages and disadvantages of composition and properties of biomass in comparison with coal: An overview,” *Fuel*, vol. 158, pp. 330–350, 2015, doi: 10.1016/j.fuel.2015.05.050.
- [20] B. Taebi and M. Mayer, “By accident or by design? Pushing global governance of nuclear safety,” *Prog. Nucl. Energy*, vol. 99, pp. 19–25, 2017, doi: 10.1016/j.pnucene.2017.04.014.
- [21] M. Berthelemy and S. Bilbao y Leon, “Nuclear Power - Tracking Report,” *International Energy Agency*, 2020. <https://www.iea.org/reports/nuclear-power>.
- [22] M. S. L. Jordan *et al.*, “Determining the electrical and thermal resistivities of radiolytically-oxidised nuclear graphite by small sample characterisation,” *J. Nucl. Mater.*, vol. 507, pp. 68–77, 2018, doi: 10.1016/j.jnucmat.2018.04.022.
- [23] F. Naziris *et al.*, “Mechanical properties and microstructure of VVER 440 RPV steels irradiated to extremely high fluences and the effect of recovery annealing,” *J. Nucl. Mater.*, vol. 551, p. 152951, 2021, doi: 10.1016/j.jnucmat.2021.152951.



- [24] K. L. Murty and I. Charit, “Structural materials for Gen-IV nuclear reactors: Challenges and opportunities,” *J. Nucl. Mater.*, vol. 383, no. 1–2, pp. 189–195, 2008, doi: 10.1016/j.jnucmat.2008.08.044.
- [25] S. Mallapati, “China Prepares To Test Thorium-Fuelled Nuclear Reactor,” *Nature*, vol. 597, pp. 311–312, 2021.
- [26] U. E. Humphrey and M. U. Khandaker, “Viability of thorium-based nuclear fuel cycle for the next generation nuclear reactor: Issues and prospects,” *Renew. Sustain. Energy Rev.*, vol. 97, no. January, pp. 259–275, 2018, doi: 10.1016/j.rser.2018.08.019.
- [27] J. Wu, J. Chen, C. Zou, C. Yu, X. Cai, and Y. Zhang, “Transition to thorium fuel cycle on a heavy water moderated molten salt reactor by using low enrichment uranium,” *Ann. Nucl. Energy*, vol. 165, p. 108638, 2022, doi: 10.1016/j.anucene.2021.108638.
- [28] “ITER,” 2021. <https://www.iter.org/>.
- [29] B. Viswanathan, “Nuclear Fission,” in *Energy Sources: Fundamentals of Chemical Conversion Processes and Applications*, Elsevier, 2017, pp. 113–126.
- [30] B. W. Brook, A. Alonso, D. A. Meneley, J. Misak, T. Blee, and J. B. van Erp, “Why nuclear energy is sustainable and has to be part of the energy mix,” *Sustain. Mater. Technol.*, vol. 1, pp. 8–16, 2014, doi: 10.1016/j.susmat.2014.11.001.
- [31] I. L. Piro, *Introduction: Generation IV international forum*. Woodhead Publishing Limited, 2016.
- [32] “Fast neutron reactors,” 2021. <https://world-nuclear.org/information-library/current-and-future-generation/fast-neutron-reactors.aspx> (accessed Oct. 31, 2021).
- [33] S. J. Zinkle and J. T. Busby, “Structural materials for fission & fusion energy,” *Mater. Today*, vol. 12, no. 11, pp. 12–19, 2009, doi: 10.1016/S1369-7021(09)70294-9.
- [34] J. Knaster, A. Moeslang, and T. Muroga, “Materials research for fusion,” *Nat. Phys.*, vol. 12, no. 5, pp. 424–434, 2016, doi: 10.1038/NPHYS3735.
- [35] R. Lindau *et al.*, “Present development status of EUROFER and ODS-EUROFER for application in blanket concepts,” *Fusion Eng. Des.*, vol. 75–79, no. SUPPL., pp. 989–996, 2005, doi: 10.1016/j.fusengdes.2005.06.186.
- [36] C. Cayron, E. Rath, I. Chu, and S. Launois, “Microstructural evolution of Y2O3 and MgAl 2O4 ODS EUROFER steels during their elaboration by mechanical milling and hot isostatic pressing,” *J. Nucl. Mater.*, vol. 335, no. 1, pp. 83–102, 2004, doi: 10.1016/j.jnucmat.2004.06.010.
- [37] I. Hilger *et al.*, “Fabrication and characterization of oxide dispersion strengthened (ODS) 14Cr steels consolidated by means of hot isostatic pressing, hot extrusion and

- spark plasma sintering,” *J. Nucl. Mater.*, vol. 472, pp. 206–214, 2016, doi: 10.1016/j.jnucmat.2015.09.036.
- [38] T. Okuda and M. Fujiwara, “Dispersion behaviour of oxide particles in mechanically alloyed ODS steel,” *J. Mater. Sci. Lett.*, vol. 14, no. 22, pp. 1600–1603, 1995, doi: 10.1007/BF00455428.
- [39] S. J. Zinkle and G. S. Was, “Materials challenges in nuclear energy,” *Acta Mater.*, vol. 61, no. 3, pp. 735–758, 2013, doi: 10.1016/j.actamat.2012.11.004.
- [40] G. S. Was, *Fundamentals of radiation materials science: Metals and alloys*. 2007.
- [41] B. Beeler, M. Asta, P. Hosemann, and N. Grønbech-Jensen, “Effect of strain and temperature on the threshold displacement energy in body-centered cubic iron,” *J. Nucl. Mater.*, vol. 474, pp. 113–119, 2016, doi: 10.1016/j.jnucmat.2016.03.017.
- [42] M. J. Banisalman, S. Park, and T. Oda, “Evaluation of the threshold displacement energy in tungsten by molecular dynamics calculations,” *J. Nucl. Mater.*, vol. 495, pp. 277–284, 2017, doi: 10.1016/j.jnucmat.2017.08.019.
- [43] D. Mason, X. Yi, M. Kirk, and S. Dudarev, “Elastic trapping of dislocation loops in cascades in ion-irradiated tungsten foils,” *J. Phys. Condens. Matter*, vol. 26, no. 37, 2014.
- [44] O. V. Ogorodnikova, V. V. Gann, M. S. Zibrov, and Y. M. Gasparyan, “Comparison of Deuterium Retention in Tungsten Pre-damaged with Energetic Electrons, Self-ions and Neutrons,” *Phys. Procedia*, vol. 71, pp. 41–46, 2015, doi: 10.1016/j.phpro.2015.08.309.
- [45] G. S. Was *et al.*, “Assessment of radiation-induced segregation mechanisms in austenitic and ferritic-martensitic alloys,” *J. Nucl. Mater.*, vol. 411, no. 1–3, pp. 41–50, 2011, doi: 10.1016/j.jnucmat.2011.01.031.
- [46] R. Bullough and M. H. Wood, “Mechanisms of radiation induced creep and growth,” *J. Nucl. Mater.*, vol. 90, pp. 1–21, 1980.
- [47] H. Trinkaus and B. N. Singh, “Helium accumulation in metals during irradiation - Where do we stand?,” *J. Nucl. Mater.*, vol. 323, no. 2–3, pp. 229–242, 2003, doi: 10.1016/j.jnucmat.2003.09.001.
- [48] A. De Bremaecker, “Past research and fabrication conducted at SCK•CEN on ferritic ODS alloys used as cladding for FBR’s fuel pins,” *J. Nucl. Mater.*, vol. 428, no. 1–3, pp. 13–30, 2012, doi: 10.1016/j.jnucmat.2011.11.060.
- [49] H. Springer *et al.*, “Efficient additive manufacturing production of oxide- and nitride-dispersion-strengthened materials through atmospheric reactions in liquid metal deposition,” *Mater. Des.*, vol. 111, no. December, pp. 60–69, 2016, doi:

- 10.1016/j.matdes.2016.08.084.
- [50] S. Ukai and M. Fujiwara, “Perspective of ODS alloys application in nuclear environments,” *J. Nucl. Mater.*, vol. 307–311, no. 1 SUPPL., pp. 749–757, 2002, doi: 10.1016/S0022-3115(02)01043-7.
- [51] S. Ukai *et al.*, “Tube manufacturing and mechanical properties of oxide dispersion strengthened ferritic steel,” *J. Nucl. Mater.*, vol. 204, no. C, pp. 74–80, 1993, doi: 10.1016/0022-3115(93)90201-9.
- [52] J. Fu, J. C. Brouwer, I. M. Richardson, and M. J. M. Hermans, “Effect of mechanical alloying and spark plasma sintering on the microstructure and mechanical properties of ODS Eurofer,” *Mater. Des.*, vol. 177, no. May, 2019, doi: 10.1016/j.matdes.2019.107849.
- [53] G. R. Odette, “Recent Progress in Developing and Qualifying Nanostructured Ferritic Alloys for Advanced Fission and Fusion Applications,” *Jom*, vol. 66, no. 12, pp. 2427–2441, 2014, doi: 10.1007/s11837-014-1207-5.
- [54] M. E. Kassner, “Creep Behaviour of Particle-Strengthened Alloys,” in *Fundamentals of Creep*, Elsevier, 2009, p. 20.
- [55] G. Yu, N. Nita, and N. Baluc, “Thermal creep behaviour of the EUROFER 97 RAFM steel and two European ODS EUROFER 97 steels,” *Fusion Eng. Des.*, vol. 75–79, no. SUPPL., pp. 1037–1041, 2005, doi: 10.1016/j.fusengdes.2005.06.311.
- [56] A. Kimura, “Current status of reduced-activation ferritic/martensitic steels R&D for fusion energy,” *Mater. Trans.*, vol. 46, no. 3, pp. 394–404, 2005, doi: 10.2320/matertrans.46.394.
- [57] S. J. Zinkle *et al.*, “Development of next generation tempered and ODS reduced activation ferritic/martensitic steels for fusion energy applications,” *Nucl. Fusion*, vol. 57, no. 9, 2017, doi: 10.1088/1741-4326/57/9/092005.
- [58] R. L. Klueh, D. S. Gelles, and M. Okada, *Reduced Activation Materials for Fusion Reactors*. 1990.
- [59] W. R. Corwin, “U.S. Generation IV Reactor Integrated Materials Technology Program,” *Nucl. Eng. Technol.*, vol. 38, no. 7, pp. 591–618, 2006.
- [60] N. Sallez *et al.*, “In situ characterization of microstructural instabilities: Recovery, recrystallization and abnormal growth in nanoreinforced steel powder,” *Acta Mater.*, vol. 87, pp. 377–389, 2015, doi: 10.1016/j.actamat.2014.11.051.
- [61] C. Suryanarayana, “Mechanical alloying and milling,” *Mech. Alloy. Milling*, vol. 46, pp. 1–472, 2004, doi: 10.4150/kpmi.2006.13.5.371.

- [62] A. García-Junceda, M. Campos, N. García-Rodríguez, and J. M. Torralba, “On the Role of Alloy Composition and Sintering Parameters in the Bimodal Grain Size Distribution and Mechanical Properties of ODS Ferritic Steels,” *Metall. Mater. Trans. A Phys. Metall. Mater. Sci.*, vol. 47, no. 11, pp. 5325–5333, 2016, doi: 10.1007/s11661-016-3538-z.
- [63] Y. Kimura, S. Takaki, S. Suejima, R. Uemori, and H. Tamehiro, “Ultra Grain Refining and Decomposition of Oxide during Super-heavy Deformation in Oxide Dispersion Ferritic Stainless Steel Powder,” *ISIJ Int.*, vol. 39, no. 1–2, pp. 176–182, 1999, doi: 10.2355/isijinternational.39.176.
- [64] M. Brocq, B. Radiguet, S. Poissonnet, F. Cuvilly, P. Pareige, and F. Legendre, “Nanoscale characterization and formation mechanism of nanoclusters in an ODS steel elaborated by reactive-inspired ball-milling and annealing,” *J. Nucl. Mater.*, vol. 409, no. 2, pp. 80–85, 2011, doi: 10.1016/j.jnucmat.2010.09.011.
- [65] N. Sallez *et al.*, “On ball-milled ODS ferritic steel recrystallization: From as-milled powder particles to consolidated state,” *J. Mater. Sci.*, vol. 50, no. 5, pp. 2202–2217, 2015, doi: 10.1007/s10853-014-8783-1.
- [66] M. Yamamoto, S. Ukai, S. Hayashi, T. Kaito, and S. Ohtsuka, “Formation of residual ferrite in 9Cr-ODS ferritic steels,” *Mater. Sci. Eng. A*, vol. 527, no. 16–17, pp. 4418–4423, 2010, doi: 10.1016/j.msea.2010.03.079.
- [67] F. J. Humphreys and M. Hatherly, *Recrystallization and related annealing phenomena*, 2nd ed. Elsevier, 2004.
- [68] K. D. Zilnyk, V. B. Oliveira, H. R. Z. Sandim, A. Möslang, and D. Raabe, “Martensitic transformation in Eurofer-97 and ODS-Eurofer steels: A comparative study,” *J. Nucl. Mater.*, vol. 462, pp. 360–367, 2015, doi: 10.1016/j.jnucmat.2014.12.112.
- [69] M. Kolluri, P. D. Edmondson, N. V. Luzginova, and F. A. V. D. Berg, “A structure-property correlation study of neutron irradiation induced damage in EU batch of ODS Eurofer97 steel,” *Mater. Sci. Eng. A*, vol. 597, pp. 111–116, 2014, doi: 10.1016/j.msea.2013.12.074.
- [70] E1245-03, “Standard Practice for Determining the Inclusion or Second-Phase Constituent Content of Metals by Automatic Image Analysis,” *Annu. B. ASTM Stand.*, vol. 3.02, no. April, pp. 1–8, 2008, doi: 10.1520/E1245-03R08.2.
- [71] S. Zhu, M. Yang, X. L. Song, S. Tang, and Z. D. Xiang, “Characterisation of Laves phase precipitation and its correlation to creep rupture strength of ferritic steels,” *Mater. Charact.*, vol. 98, pp. 60–65, 2014, doi: 10.1016/j.matchar.2014.10.004.

- [72] J. S. Lee, H. Ghassemi Armaki, K. Maruyama, T. Muraki, and H. Asahi, “Causes of breakdown of creep strength in 9Cr-1.8W-0.5Mo-VNb steel,” *Mater. Sci. Eng. A*, vol. 428, no. 1–2, pp. 270–275, 2006, doi: 10.1016/j.msea.2006.05.010.
- [73] Q. Li, “Precipitation of Fe<sub>2</sub>W laves phase and modeling of its direct influence on the strength of a 12Cr-2W steel,” *Metall. Mater. Trans. A Phys. Metall. Mater. Sci.*, vol. 37, no. 1, pp. 89–97, 2006, doi: 10.1007/s11661-006-0155-2.
- [74] M. K. Miller, J. M. Hyde, M. G. Hetherington, A. Cerezo, G. D. W. Smith, and C. M. Elliot, “Spinodal decomposition in Fe-Cr alloys: experimental study at the atomic level and comparison with computer models - I. Introduction and Methodology,” *Acta Mater.*, vol. 43, no. 9, pp. 3385–3401, 1995.
- [75] J. I. Goldstein, D. E. Newbury, J. R. Michael, N. W. M. Ritchie, J. H. J. Scott, and D. C. Joy, *Scanning Electron Microscopy and X-Ray Microanalysis*. Springer, 2018.
- [76] S. Ukai, S. Mizuta, M. Fujiwara, T. Okuda, and T. Kobayashi, “Development of 9cr-ods martensitic steel claddings for fuel pins by means of ferrite to austenite phase transformation,” *J. Nucl. Sci. Technol.*, vol. 39, no. 7, pp. 778–788, 2002, doi: 10.1080/18811248.2002.9715260.
- [77] M. J. R. Sandim, I. R. Souza Filho, E. H. Bredda, A. Kostka, D. Raabe, and H. R. Z. Sandim, “Coarsening of Y-rich oxide particles in 9%Cr-ODS Eurofer steel annealed at 1350 °C,” *J. Nucl. Mater.*, vol. 484, pp. 283–287, 2017, doi: 10.1016/j.jnucmat.2016.12.025.
- [78] T. P. Davis, “Review of the iron-based materials applicable for the fuel and core of future Sodium Fast Reactors,” 2018.
- [79] A. Hirata, T. Fujita, Y. R. Wen, J. H. Schneibel, C. T. Liu, and M. W. Chen, “Atomic structure of nanoclusters in oxide-dispersion-strengthened steels,” *Nat. Mater.*, vol. 10, no. 12, pp. 922–926, 2011, doi: 10.1038/nmat3150.
- [80] K. D. Zilnyk, K. G. Pradeep, P. Choi, H. R. Z. Sandim, and D. Raabe, “Long-term thermal stability of nanoclusters in ODS-Eurofer steel: An atom probe tomography study,” *J. Nucl. Mater.*, vol. 492, pp. 142–147, 2017, doi: 10.1016/j.jnucmat.2017.05.027.
- [81] R. A. Renzetti, H. R. Z. Sandim, M. J. R. Sandim, A. D. Santos, A. Möslang, and D. Raabe, “Annealing effects on microstructure and coercive field of ferritic-martensitic ODS Eurofer steel,” *Mater. Sci. Eng. A*, vol. 528, no. 3, pp. 1442–1447, 2011, doi: 10.1016/j.msea.2010.10.051.
- [82] M. A. Moghadasi, M. Nili-Ahmadabadi, F. Forghani, and H. S. Kim, “Development of

- an oxide-dispersion-strengthened steel by introducing oxygen carrier compound into the melt aided by a general thermodynamic model,” *Sci. Rep.*, vol. 6, no. November, pp. 1–10, 2016, doi: 10.1038/srep38621.
- [83] T. L. Martin *et al.*, “Comparing the Consistency of Atom Probe Tomography Measurements of Small-Scale Segregation and Clustering between the LEAP 3000 and LEAP 5000 Instruments,” *Microsc. Microanal.*, vol. 23, no. 2, pp. 227–237, 2017, doi: 10.1017/S1431927617000356.
- [84] T. P. Davis *et al.*, “Electron microscopy and atom probe tomography of nanoindentation deformation in oxide dispersion strengthened steels,” *Mater. Charact.*, vol. 167, no. April, p. 110477, 2020, doi: 10.1016/j.matchar.2020.110477.
- [85] M. Yamamoto, S. Ukai, S. Hayashi, T. Kaito, and S. Ohtsuka, “Reverse phase transformation from  $\alpha$  to  $\gamma$  in 9Cr-ODS ferritic steels,” *J. Nucl. Mater.*, vol. 417, no. 1–3, pp. 237–240, 2011, doi: 10.1016/j.jnucmat.2010.12.250.
- [86] A. Durand *et al.*, “Characterization of untransformed ferrite in 10Cr and 12Cr ODS steels,” *Materialia*, vol. 16, p. 101066, 2021, doi: 10.1016/j.mtla.2021.101066.
- [87] D. J. Larson, B. Gault, B. P. Geiser, F. De Geuser, and F. Vurpillot, “Atom probe tomography spatial reconstruction: Status and directions,” *Curr. Opin. Solid State Mater. Sci.*, vol. 17, no. 5, pp. 236–247, 2013, doi: 10.1016/j.cossms.2013.09.002.
- [88] T. P. Davis *et al.*, “Materialia Atom probe characterisation of segregation driven Cu and Mn – Ni – Si co-precipitation in neutron irradiated T91 tempered-martensitic steel,” *Materialia*, vol. 14, no. October, 2020, doi: 10.1016/j.mtla.2020.100946.
- [89] C. A. Williams, E. A. Marquis, A. Cerezo, and G. D. W. Smith, “Nanoscale characterisation of ODS-Eurofer 97 steel: An atom-probe tomography study,” *J. Nucl. Mater.*, vol. 400, no. 1, pp. 37–45, 2010, doi: 10.1016/j.jnucmat.2010.02.007.
- [90] S. Dhara, R. K. W. Marceau, K. Wood, and T. Dorin, “Data in Brief Atom probe tomography data analysis procedure for precipitate and cluster identification in a Ti-Mo steel,” *Data Br.*, vol. 18, pp. 968–982, 2018, doi: 10.1016/j.dib.2018.03.094.
- [91] A. J. London *et al.*, “Comparison of atom probe tomography and transmission electron microscopy analysis of oxide dispersion strengthened steels,” *J. Phys. Conf. Ser.*, vol. 522, no. 1, 2014, doi: 10.1088/1742-6596/522/1/012028.
- [92] J. Fu, T. P. Davis, A. Kumar, I. M. Richardson, and M. J. M. Hermans, “Characterisation of the influence of vanadium and tantalum on yttrium-based nano-oxides in ODS Eurofer steel,” *Mater. Charact.*, vol. 175, no. April, 2021, doi: 10.1016/j.matchar.2021.111072.

- [93] V. De Castro, E. A. Marquis, S. Lozano-Perez, R. Pareja, and M. L. Jenkins, “Stability of nanoscale secondary phases in an oxide dispersion strengthened Fe-12Cr alloy,” *Acta Mater.*, vol. 59, no. 10, pp. 3927–3936, 2011, doi: 10.1016/j.actamat.2011.03.017.
- [94] T. Nishizawa, I. Ohnuma, and K. Ishida, “Examination of the Zener relationship between grain size and particle dispersion,” *Mater. Trans. JIM*, vol. 38, no. 11, pp. 950–956, 1997.
- [95] T. Nagano and M. Enomoto, “Calculation of the interfacial energies between  $\alpha$  and  $\gamma$  iron and equilibrium particle shape,” *Metall. Mater. Trans. A*, vol. 37, no. 3, pp. 929–937, 2006, doi: 10.1007/s11661-006-0066-2.
- [96] V. K. Devra and J. Maity, “Solute drag effect on austenite grain growth in hypoeutectoid steel,” *Philos. Mag. Lett.*, vol. 100, no. 6, pp. 245–259, 2020, doi: 10.1080/09500839.2020.1750723.
- [97] S. Ukai *et al.*, “Alloying design of oxide dispersion strengthened ferritic steel for long life FBRs core materials,” *J. Nucl. Mater.*, vol. 204, no. C, pp. 65–73, 1993, doi: 10.1016/0022-3115(93)90200-I.
- [98] T. Narita, S. Ukai, B. Leng, S. Ohtsuka, and T. Kaito, “Characterization of recrystallization of 12Cr and 15Cr ODS ferritic steels,” *J. Nucl. Sci. Technol.*, vol. 50, no. 3, pp. 314–320, 2013, doi: 10.1080/00223131.2013.772446.
- [99] M. Praud *et al.*, “Study of the deformation mechanisms in a Fe-14% Cr ODS alloy,” *J. Nucl. Mater.*, vol. 428, no. 1–3, pp. 90–97, 2012, doi: 10.1016/j.jnucmat.2011.10.046.
- [100] P. Dou *et al.*, “Effects of titanium concentration and tungsten addition on the nano-mesoscopic structure of high-Cr oxide dispersion strengthened (ODS) ferritic steels,” *J. Nucl. Mater.*, vol. 442, no. 1-3 SUPPL.1, pp. S95–S100, 2013, doi: 10.1016/j.jnucmat.2013.04.090.
- [101] E. Gil, N. Ordás, C. García-Rosales, and I. Iturriza, “Microstructural characterization of ODS ferritic steels at different processing stages,” *Fusion Eng. Des.*, vol. 98–99, pp. 1973–1977, 2015, doi: 10.1016/j.fusengdes.2015.06.010.
- [102] Y. Li *et al.*, “Effects of fabrication processing on the microstructure and mechanical properties of oxide dispersion strengthening steels,” *Mater. Sci. Eng. A*, vol. 654, pp. 203–212, 2016, doi: 10.1016/j.msea.2015.12.032.
- [103] J. Shen *et al.*, “Microstructural characterization and strengthening mechanisms of a 12Cr-ODS steel,” *Mater. Sci. Eng. A*, vol. 673, pp. 624–632, 2016, doi: 10.1016/j.msea.2016.07.030.
- [104] D. Kumar, U. Prakash, V. V. Dabhade, K. Laha, and T. Sakthivel, “Development of

- Oxide Dispersion Strengthened (ODS) Ferritic Steel Through Powder Forging,” *J. Mater. Eng. Perform.*, vol. 26, no. 4, pp. 1817–1824, 2017, doi: 10.1007/s11665-017-2573-2.
- [105] S. Seils, A. Kauffmann, F. Hinrichs, D. Schliephake, T. Boll, and M. Heilmaier, “Temperature dependent strengthening contributions in austenitic and ferritic ODS steels,” *Mater. Sci. Eng. A*, vol. 786, no. January, p. 139452, 2020, doi: 10.1016/j.msea.2020.139452.
- [106] T. Narita, S. Ukai, S. Ohtsuka, and M. Inoue, “Effect of tungsten addition on microstructure and high temperature strength of 9CrODS ferritic steel,” *J. Nucl. Mater.*, vol. 417, no. 1–3, pp. 158–161, 2011, doi: 10.1016/j.jnucmat.2011.01.060.
- [107] W. Xing *et al.*, “First-principles studies of hydrogen behavior interacting with oxygen-enriched nanostructured particles in the ODS steels,” *Int. J. Hydrogen Energy*, vol. 39, no. 32, pp. 18506–18519, 2014, doi: 10.1016/j.ijhydene.2014.09.036.
- [108] J. Ribis, M. L. Lescoat, S. Y. Zhong, M. H. Mathon, and Y. De Carlan, “Influence of the low interfacial density energy on the coarsening resistivity of the nano-oxide particles in Ti-added ODS material,” *J. Nucl. Mater.*, vol. 442, no. 1-3 SUPPL.1, pp. S101–S105, 2013, doi: 10.1016/j.jnucmat.2012.10.051.
- [109] T. Muroga *et al.*, “Fabrication and characterization of reference 9Cr and 12Cr-ODS low activation ferritic/martensitic steels,” *Fusion Eng. Des.*, vol. 89, no. 7–8, pp. 1717–1722, 2014, doi: 10.1016/j.fusengdes.2014.01.010.
- [110] O. Prat, J. Garcia, D. Rojas, G. Sauthoff, and G. Inden, “The role of Laves phase on microstructure evolution and creep strength of novel 9%Cr heat resistant steels,” *Intermetallics*, vol. 32, pp. 362–372, 2013, doi: 10.1016/j.intermet.2012.08.016.
- [111] N. Baluc *et al.*, “Review on the EFDA work programme on nano-structured ODS RAF steels,” *J. Nucl. Mater.*, vol. 417, no. 1–3, pp. 149–153, 2011, doi: 10.1016/j.jnucmat.2010.12.065.
- [112] J. Shen *et al.*, “Microstructural stability of an as-fabricated 12Cr-ODS steel under elevated-temperature annealing,” *J. Alloys Compd.*, vol. 695, pp. 1946–1955, 2017, doi: 10.1016/j.jallcom.2016.11.029.
- [113] D. E. Newbury and N. W. M. Ritchie, “Performing elemental microanalysis with high accuracy and high precision by scanning electron microscopy/silicon drift detector energy-dispersive X-ray spectrometry (SEM/SDD-EDS),” *J. Mater. Sci.*, vol. 50, no. 2, pp. 493–518, 2014, doi: 10.1007/s10853-014-8685-2.
- [114] M. Klimiankou, R. Lindau, and A. Möslang, “Energy-filtered TEM imaging and EELS



- study of ODS particles and Argon-filled cavities in ferritic-martensitic steels,” *Micron*, vol. 36, no. 1, pp. 1–8, 2005, doi: 10.1016/j.micron.2004.08.001.
- [115] Y. Ortega, M. A. Monge, V. de Castro, A. Muñoz, T. Leguey, and R. Pareja, “Void formation in ODS EUROFER produced by hot isostatic pressing,” *J. Nucl. Mater.*, vol. 386–388, no. C, pp. 462–465, 2009, doi: 10.1016/j.jnucmat.2008.12.145.
- [116] Y. L. Chen, A. R. Jones, and U. Miller, “Origin of porosity in oxide-dispersion-strengthened alloys produced by mechanical alloying,” *Metall. Mater. Trans. A Phys. Metall. Mater. Sci.*, vol. 33, no. 8, pp. 2713–2718, 2002, doi: 10.1007/s11661-002-0393-x.
- [117] V. S. M. Pereira, H. Schut, and J. Sietsma, “A study of the microstructural stability and defect evolution in an ODS Eurofer steel by means of Electron Microscopy and Positron Annihilation Spectroscopy,” *J. Nucl. Mater.*, vol. 540, 2020, doi: 10.1016/j.jnucmat.2020.152398.
- [118] K. Dawson and G. J. Tatlock, “Characterisation of nanosized oxides in ODM401 oxide dispersion strengthened steel,” *J. Nucl. Mater.*, vol. 444, no. 1–3, pp. 252–260, 2014, doi: 10.1016/j.jnucmat.2013.10.003.
- [119] J. Ribis and Y. De Carlan, “Interfacial strained structure and orientation relationships of the nanosized oxide particles deduced from elasticity-driven morphology in oxide dispersion strengthened materials,” *Acta Mater.*, vol. 60, no. 1, pp. 238–252, 2012, doi: 10.1016/j.actamat.2011.09.042.
- [120] M. Dade, J. Malaplate, J. Garnier, F. De Geuser, N. Lochet, and A. Deschamps, “Influence of consolidation methods on the recrystallization kinetics of a Fe-14Cr based ODS steel,” *J. Nucl. Mater.*, vol. 472, pp. 143–152, 2016, doi: 10.1016/j.jnucmat.2016.01.019.
- [121] A. P. Druzhkov and D. A. Perminov, “Characterisation of atomic-scale defects in ODS ferritic alloys by positron annihilation,” *Philos. Mag.*, vol. 99, no. 7, pp. 887–904, 2019, doi: 10.1080/14786435.2018.1563309.
- [122] R. Domínguez-Reyes, M. A. Auger, M. A. Monge, and R. Pareja, “Positron annihilation study of the vacancy clusters in ODS Fe–14Cr alloys,” *Philos. Mag.*, vol. 97, no. 11, pp. 833–850, 2017, doi: 10.1080/14786435.2017.1280621.
- [123] F. A. Selim, “Positron annihilation spectroscopy of defects in nuclear and irradiated materials- a review,” *Mater. Charact.*, vol. 174, p. 110952, 2021, doi: 10.1016/j.matchar.2021.110952.
- [124] R. Rajaraman, G. Amarendra, and C. S. Sundar, “Defect evolution in steels: Insights

- from positron studies,” *Phys. Status Solidi Curr. Top. Solid State Phys.*, vol. 6, no. 11, pp. 2285–2290, 2009, doi: 10.1002/pssc.200982112.
- [125] C. W. He, M. F. Barthe, P. Desgardin, S. Akhmadaliev, M. Behar, and F. Jomard, “Positron studies of interaction between yttrium atoms and vacancies in bcc iron with relevance for ODS nanoparticles formation,” *J. Nucl. Mater.*, vol. 455, no. 1–3, pp. 398–401, 2014, doi: 10.1016/j.jnucmat.2014.07.027.
- [126] M. Lambrecht and L. Malerba, “Positron annihilation spectroscopy on binary Fe-Cr alloys and ferritic/martensitic steels after neutron irradiation,” *Acta Mater.*, vol. 59, no. 17, pp. 6547–6555, 2011, doi: 10.1016/j.actamat.2011.06.046.
- [127] Y. Ortega, V. de Castro, M. A. Monge, A. Muñoz, T. Leguey, and R. Pareja, “Positron annihilation characteristics of ODS and non-ODS EUROFER isochronally annealed,” *J. Nucl. Mater.*, vol. 376, no. 2, pp. 222–228, 2008, doi: 10.1016/j.jnucmat.2008.03.005.
- [128] J. Degmová *et al.*, “NDT study of precipitation processes in thermally aged Fe-20Cr alloy,” *J. Nucl. Mater.*, vol. 547, 2021, doi: 10.1016/j.jnucmat.2021.152799.
- [129] C. L. Fu, M. Krčmar, G. S. Painter, and X. Q. Chen, “Vacancy mechanism of high oxygen solubility and nucleation of stable oxygen-enriched clusters in Fe,” *Phys. Rev. Lett.*, vol. 99, no. 22, pp. 1–4, 2007, doi: 10.1103/PhysRevLett.99.225502.
- [130] H. Schut, “A variable energy positron beam facility with applications in materials science,” Delft University of Technology, 1990.
- [131] I. Carvalho, “Steels for Nuclear Reactors: Eurofer 97,” Delft University of Technology, 2016.
- [132] M. Eldrup, “Positron methods for the study of defects in bulk materials,” *J. Phys. IV JP*, vol. 5, no. C8, pp. 93–109, 1995, doi: 10.1051/jp4:1995111.
- [133] R. P. Gupta and R. W. Siegel, “Positron trapping and annihilation at vacancies in BCC refractory metals,” *J. Phys. F Met. Phys.*, vol. 10, no. 1, 1980, doi: 10.1088/0305-4608/10/1/002.
- [134] C. Andres, “Some effects on polymers of low-energy implanted positrons,” Ghent University, 2008.
- [135] T. P. Davis *et al.*, “Electron microscopy and atom probe tomography of nanoindentation deformation in oxide dispersion strengthened steels,” *Mater. Charact.*, vol. 167, no. June, p. 110477, 2020, doi: 10.1016/j.matchar.2020.110477.
- [136] I. Carvalho, H. Schut, A. Fedorov, N. Luzginova, and J. Sietsma, “Characterization of helium ion implanted reduced activation ferritic / martensitic steel with positron annihilation and helium thermal desorption methods,” *J. Nucl. Mater.*, vol. 442, no. 1–

- 3, pp. S48–S51, 2013, doi: 10.1016/j.jnucmat.2013.03.029.
- [137] S. Mantl and W. Triftshäuser, “Defect annealing studies on metals by positron annihilation and electrical resistivity measurements,” *Phys. Rev. B*, vol. 17, no. 4, pp. 1645–1652, 1978, doi: 10.1103/PhysRevB.17.1645.
- [138] H. Matter, J. Winter, and W. Triftshäuser, “Phase transformations and vacancy formation energies of transition metals by positron annihilation,” *Appl. Phys.*, vol. 20, no. 2, pp. 135–140, 1979, doi: 10.1007/BF00885934.
- [139] E. Del Rio *et al.*, “Formation energy of vacancies in FeCr alloys: Dependence on Cr concentration,” *J. Nucl. Mater.*, vol. 408, no. 1, pp. 18–24, 2011, doi: 10.1016/j.jnucmat.2010.10.021.
- [140] B. Zhang, “Calculation of self-diffusion coefficients in iron,” *AIP Adv.*, vol. 4, no. 1, 2014, doi: 10.1063/1.4863462.
- [141] J.-J. HUET, “POSSIBLE FAST-REACTOR CANNING MATERIAL STRENGTHENED AND STABILIZED BY DISPERSION,” *Powder Metall.*, vol. 10, no. 20, pp. 208–215, Sep. 1967, doi: 10.1179/pom.1967.10.20.010.
- [142] A. Möslang *et al.*, “Towards reduced activation structural materials data for fusion DEMO reactors,” *Nucl. Fusion*, vol. 45, no. 7, pp. 649–655, 2005, doi: 10.1088/0029-5515/45/7/013.
- [143] F. Wei and K. Tsuzaki, “Hydrogen trapping phenomena in martensitic steels 13,” in *Gaseous Hydrogen Embrittlement of Materials in Energy Technologies*, 1st ed., R. P. Gangloff and B. P. Somerday, Eds. Woodhead Publishing Limited, 2012.
- [144] E. Malitckii, Y. Yagodzinskyy, M. Ganchenkova, S. Binyukova, and H. Hänninen, “Comparative study of hydrogen uptake and diffusion in ODS steels,” *Fusion Eng. Des.*, vol. 88, no. 9–10, pp. 2607–2610, 2013, doi: 10.1016/j.fusengdes.2013.04.050.
- [145] E. Malitckii, Y. Yagodzinskyy, and H. Hänninen, “Hydrogen uptake from plasma and its effect on EUROFER 97 and ODS-EUROFER steels at elevated temperatures,” *Fusion Eng. Des.*, vol. 98–99, pp. 2025–2029, 2015, doi: 10.1016/j.fusengdes.2015.05.049.
- [146] I. Maroef, D. L. Olson, M. Eberhart, and G. R. Edwards, “Hydrogen trapping in ferritic steel weld metal,” *Int. Mater. Rev.*, vol. 47, no. 4, pp. 191–223, 2002, doi: 10.1179/095066002225006548.
- [147] G. A. Esteban, A. Peña, F. Legarda, and R. Lindau, “Hydrogen transport and trapping in ODS-EUROFER,” *Fusion Eng. Des.*, vol. 82, no. 15–24, pp. 2634–2640, 2007, doi: 10.1016/j.fusengdes.2007.02.002.

- [148] O. V. Ogorodnikova, Z. Zhou, K. Sugiyama, M. Balden, Y. Gasparyan, and V. Efimov, “Surface modification and deuterium retention in reduced-activation steels under low-energy deuterium plasma exposure. Part I: Undamaged steels,” *Nucl. Fusion*, vol. 57, no. 3, 2017, doi: 10.1088/1741-4326/57/3/036010.
- [149] O. V. Ogorodnikova *et al.*, “Surface modification and deuterium retention in reduced-activation steels under low-energy deuterium plasma exposure. Part II: Steels pre-damaged with 20 MeV W ions and high heat flux,” *Nucl. Fusion*, vol. 57, no. 3, 2017, doi: 10.1088/1741-4326/57/3/036011.
- [150] H. Hagi and Y. Hayashi, “Effect of Dislocation Trapping on Hydrogen and Deuterium Diffusion in Iron,” *Trans. Japan Inst. Met.*, vol. 28, no. 5, pp. 368–374, 1987, doi: 10.2320/matertrans1960.28.368.
- [151] W. Y. Choo and J. Y. Lee, “Thermal Analysis of Trapped Hydrogen in Pure Iron,” *Metall. Mater. Trans. A Phys. Metall. Mater. Sci.*, vol. 13, no. January, pp. 135–140, 1982.
- [152] F. G. Wei, T. Hara, and K. Tsuzaki, “Precise Determination of the Activation Energy for Desorption of Hydrogen in Two Ti-Added Steels by a Single Thermal-Desorption Spectrum,” *Metall. Mater. Trans. B*, vol. 35, no. June, pp. 587–597, 2004.
- [153] A. McNabb and P. Foster, “A new analysis of diffusion of hydrogen in iron and ferritic steels,” *Trans. Metall. Soc. AIME*, vol. 227, pp. 618–627, 1963.
- [154] R. A. Oriani, “The diffusion and trapping of hydrogen in steel,” *Acta Metall.*, vol. 18, no. 1, pp. 147–157, 1970, doi: 10.1016/0001-6160(70)90078-7.
- [155] K. Ono and M. Meshii, “Hydrogen detrapping from grain boundaries and dislocations in high purity iron,” *Acta Metall. Mater.*, vol. 40, no. 6, pp. 1357–1364, 1992, doi: 10.1016/0956-7151(92)90436-I.
- [156] H. E. Kissinger, “Reaction Kinetics in Differential Thermal Analysis,” *Anal. Chem.*, vol. 29, no. 11, pp. 1702–1706, 1957, doi: 10.1021/ac60131a045.
- [157] H. E. Kissinger, “Variation of Peak Temperature With Heating Rate In Differential Thermal Analysis,” *J. Res. Natl. Bur. Stand. (1934).*, vol. 57, no. 4, pp. 217–221, 1956.
- [158] F. G. Wei and K. Tsuzaki, “Quantitative Analysis on Hydrogen Trapping of TiC Particles in Steel,” *Metall. Mater. Trans. A Phys. Metall. Mater. Sci.*, vol. 37, no. February, pp. 331–353, 2006.
- [159] F. Wei, M. Enomoto, and K. Tsuzaki, “Applicability of the Kissinger ’ s formula and comparison with the McNabb – Foster model in simulation of thermal desorption spectrum,” *Comput. Mater. Sci.*, vol. 51, no. 1, pp. 322–330, 2012, doi:

- 10.1016/j.commat.2011.07.009.
- [160] G. R. Longhurst, “TMAP7 User Manual,” 2008. doi: 10.2172/952013.
- [161] G. M. Wright, M. Mayer, K. Ertl, G. De Saint-Aubin, and J. Rapp, “TMAP7 simulations of deuterium trapping in pre-irradiated tungsten exposed to high-flux plasma,” *J. Nucl. Mater.*, vol. 415, no. 1 SUPPL, pp. S636–S640, 2011, doi: 10.1016/j.jnucmat.2011.01.011.

## Summary

An approach to improve the performance of steels for fusion and fission reactors is to reinforce them with oxide nanoparticles. These can hinder dislocation and grain boundary movement and trap radiation-induced defects, thus increasing creep and radiation damage resistance. Steels containing these oxide particles are called ODS steels (Oxide Dispersion Strengthened). In the present thesis, two ODS steels containing 0.3 weight % of  $Y_2O_3$  were studied: the 0.3%  $Y_2O_3$  ODS Eurofer and the ODS 12 Cr steel. The main objectives of the work developed during these four years were: (i) evaluation of the thermal stability of the microstructure and of the oxide nanoparticles present in the steels; (ii) investigation of the effect of oxide nanoparticles on phase transformations and other microstructural processes, such as recovery and recrystallization; (iii) investigation of the interaction of oxide nanoparticles with defects intrinsic to the microstructure and (iv) development of the fundamental understanding of the behaviour of the steels prior to exposure to radiation.

The systematic characterization of microstructure of the two ODS steels was made, in their reference state and after 1 h annealing treatments at temperatures ranging from 573 K to 1600 K. The techniques used were Scanning Electron Microscopy (SEM), Electron Backscatter Diffraction (EBSD) and Vickers hardness testing. The oxide nanoparticles present in the 0.3%  $Y_2O_3$  ODS Eurofer steel were observed using Transmission Electron Microscopy (TEM) and Atom Probe Tomography (APT); the oxide nanoparticles in the ODS 12 Cr steel were analysed with TEM. The 0.3%  $Y_2O_3$  ODS Eurofer steel has, in its reference state, an isotropic microstructure, without significant texture, composed of tempered martensite, residual ferrite and  $M_{23}C_6$  carbides. The ODS 12 Cr steel does not form austenite at high temperatures and, therefore, its matrix is always ferritic, with TiC carbides located along grain boundaries. Because of consolidation by hot extrusion, the ferritic grains in the ODS 12 Cr steel are elongated and present  $\langle 110 \rangle_\alpha$ -fibre texture. In the 0.3%  $Y_2O_3$  ODS Eurofer steel the oxide nanoparticles are composed of Y, V and O; in the ODS 12 Cr steel, the nanoparticles are Y, Ti and O based. The addition of Ti is known for reducing the final oxide nanoparticle size and for conferring higher thermal stability to the particles. When the oxide nanoparticles remain refined at high temperatures, the Zener pinning force exerted by them also remains strong and the overall microstructure does not become coarser during exposure to elevated temperatures. The Y-V-O based nanoparticles in the 0.3%  $Y_2O_3$  ODS Eurofer steel go through coarsening during annealing at 1400 K, which leads to the formation of a coarser microstructure upon

cooling to room temperature and reduction in the Vickers hardness. In the ODS 12 Cr steel, a fraction of the Y-Ti-O nanoparticles becomes coarser only after 1 h annealing at 1573 K, which leads to a moderate degree of softening of the material.

Positron Annihilation Doppler Broadening (PADB) was used to investigate the thermal evolution of defects present in different ODS steels and their interaction with oxide nanoparticles. PADB results suggest that the oxide nanoparticles are able to trap thermal vacancies, formed in high concentrations during annealing at temperatures of 1400 K and above. The excess of thermal vacancies, trapped by the oxide nanoparticles, is retained in the microstructure upon cooling to room temperature. To further investigate this hypothesis, Thermal Desorption Spectroscopy (TDS) measurements were carried out in the ODS 12 Cr steel, in its as-received condition and after annealing at 1573 K for 1 h, after exposure to low-energy deuterium plasma. The deuterium uptake in the annealed condition was higher than that in the as-received state, and it could be related to the prior-trapping of thermal vacancies by oxide nanoparticles, which would be able, then, to accommodate more deuterium atoms. The ability to accommodate more deuterium atoms (or hydrogen, or helium, or other radiation-induced interstitials) could have positive effects on the performance of the steel during service, but mechanical testing is necessary to verify this influence.

## Samenvatting

Een benadering om de prestaties van staal voor kernsplijting en fusiereactoren te verbeteren, is om ze te versterken met oxide-nanodeeltjes. Deze kunnen beweging van dislocaties en korrelgrenzen belemmeren en stralingsgeïnduceerde defecten binden, waardoor de weerstand tegen kruip en stralingsschade toeneemt. Staalsoorten die deze oxidedeeltjes bevatten worden ODS-stalen genoemd, *Oxide Dispersion Strengthened*. In dit proefschrift zijn twee ODS-staalsoorten met 0,3 gew.%  $Y_2O_3$  bestudeerd: 0,3%  $Y_2O_3$  ODS Eurofer en ODS 12 Cr staal. De belangrijkste doelstellingen van het werk dat gedurende deze vier jaar werd ontwikkeld, waren: (i) het evalueren van de thermische stabiliteit van de microstructuur en van de oxide-nanodeeltjes die aanwezig zijn in het staal; (ii) het effect van oxide-nanodeeltjes op de kinetiek van faseformaties en andere microstructurele processen (herstel, rekristallisatie) onderzoeken; (iii) de mogelijke interactie van oxide-nanodeeltjes met defecten die inherent zijn aan de microstructuur onderzoeken en (iv) een meer fundamenteel begrip ontwikkelen van het gedrag van de staalsoorten voorafgaand aan blootstelling aan straling.

De systematische karakterisering van de microstructuur van de twee ODS-staalsoorten werd gedaan in de referentietoestand en na gloeibehandelingen van 1 uur bij temperaturen van 573 K tot 1600 K. De gebruikte technieken waren Scanning Electron Microscopy (SEM), Electron Backscatter Diffraction (EBSD) en Vickers-hardheidmetingen. De oxide-nanodeeltjes die aanwezig zijn in het 0,3%  $Y_2O_3$  ODS Eurofer-staal werden waargenomen met behulp van Transmission Electron Microscopy (TEM) en Atom Probe Tomography (APT); de oxide-nanodeeltjes in het ODS 12 Cr-staal werden geanalyseerd met TEM. Het 0,3%  $Y_2O_3$  ODS Eurofer-staal heeft in de referentietoestand een isotrope microstructuur, zonder significante textuur, en is samengesteld uit ontlaten martensiet, restferriet en  $M_{23}C_6$ -carbiden. Het ODS 12 Cr-staal vormt geen austeniet bij hoge temperaturen en daarom is de matrix altijd ferritisch, met TiC-carbiden langs korrelgrenzen. Vanwege consolidatie door extrusie op hoge temperatuur zijn de ferrietkorrels in het ODS 12 Cr-staal langwerpig en hebben een  $\langle 110 \rangle_\alpha$ -vezeltextuur. In het 0,3%  $Y_2O_3$  ODS Eurofer-staal zijn de oxide-nanodeeltjes samengesteld uit Y, V en O; in het ODS 12 Cr-staal zijn de nanodeeltjes gebaseerd op Y, Ti, O. Het is bekend dat de toevoeging van Ti leidt tot het verminderen van de uiteindelijke grootte van de oxide-nanodeeltjes en tot een hogere thermische stabiliteit van de deeltjes. Wanneer de oxide-nanodeeltjes bij hoge temperaturen fijn verdeeld blijven, blijft de Zener-pinkracht die ze uitoefenen ook sterk en wordt de algehele microstructuur niet grover tijdens blootstelling aan



hoge temperaturen. De op Y-V-O gebaseerde nanodeeltjes in het 0,3%  $Y_2O_3$  ODS Eurofer-staal worden grover tijdens het gloeien bij 1400 K, hetgeen leidt tot de vorming van een grovere microstructuur bij afkoeling tot kamertemperatuur en vermindering van de Vickers-hardheid. In het ODS 12 Cr-staal wordt een fractie van de Y-Ti-O-nanodeeltjes pas grover na 1 uur gloeien bij 1573 K, hetgeen leidt tot enige verzwakking van het materiaal.

Positron Annihilation Doppler Broadening (PADB) werd gebruikt om de thermische ontwikkeling van defecten in verschillende ODS-staalsoorten en hun interactie met oxide-nanodeeltjes te onderzoeken. PADB-resultaten suggereren dat de oxide-nanodeeltjes in staat zijn om thermische vacatures te binden, gevormd in hoge concentraties tijdens uitgloeien bij temperaturen van 1400 K en hoger. De overmaat aan thermische vacatures, gebonden door de oxide-nanodeeltjes, wordt bij afkoeling tot kamertemperatuur in de microstructuur vastgehouden. Om deze hypothese verder te onderzoeken werden thermische desorptiespectroscopiemetingen (TDS) uitgevoerd in het ODS 12 Cr-staal, in de uitgangstoestand en na 1 uur gloeien bij 1573 K, na blootstelling aan een laag-energetisch deuteriumplasma. De opname van deuterium in de gegloeide toestand was hoger dan die in de uitgangstoestand, hetgeen verband zou kunnen houden met het eerder optredende insluiten van thermische vacatures door oxide-nanodeeltjes, die dan in staat zouden zijn om meer deuteriumatomen te accommoderen. Toch zijn er meer experimenten nodig om dit effect te bevestigen. Het vermogen om meer deuteriumatomen (of waterstof, helium of andere door straling veroorzaakte interstitiëlen) op te nemen, zou positieve effecten kunnen hebben op de prestaties van het staal tijdens gebruik, maar mechanische tests zijn noodzakelijk om dit vast te stellen.

## Acknowledgements

5<sup>th</sup> of February of 2017; the date in which I arrived in The Netherlands, to start my PhD at TU Delft. I was so happy to be in The Netherlands, starting this new and exciting chapter of my life! Even though I was getting lost in Delft all the time, facing windstorms and heavy winter (in my “newly-arrived from Brazil” perspective), away from family and friends, getting used to the bicycles everywhere and to the dutch names of streets and places that I couldn’t pronounce, I always had a smile on my face. And it was a genuine smile of happiness, that stayed with me during all these 5 years (and it is still here!), independent of eventual difficulties and challenges. The PhD opportunity was not only important for my academic life and career, but for my life in general and I am immensely grateful for it. And, of course, I would not be here and with a doctoral thesis written if it weren’t for many important people.

First of all I would like to thank Jilt Sietsma and Henk Schut for accepting me as their student, for the supervision and guidance during these years. I have learnt a lot from you and I appreciated every meeting, every discussion we had. Jilt, thank you for your insightful comments and observations in all aspects of the work we developed, for your detailed revision of papers, for always being so welcoming and open. Henk, thank you for the amazing lectures about positrons, thermal desorption and physics in general; for working together in the experimental hall, for our sessions analysing data and your great sense of humour that made work in complicated topics lighter.

I would like to thank M2i, NWO and NRG for the funding of the project. I would like to further thank M2i for providing this rich scientific network, which allows the execution of so many interesting projects.

I would like to thank the committee members that evaluated this thesis, for their contributions and valuable discussions: Catherine Pappas, Marie-France Barthe, Marco de Baar, Tjark van Staveren, Roumen Petrov and Leo Kestens.

I would like to thank DIFFER for the administration of the project and DIFFER colleagues for help in many aspects: Marco de Baar for his role as project leader, always approachable and helpful; to Shih-Chi Wang and Thomas Morgan for the collaboration and excellent discussions related to experiments in the Nano-PSI and thermal desorption spectroscopy; to Ans van den Heuvel-Vermeer for the endless patience to explain and help with financial matters; to Bebe van der Vlis and Jolanda van Achthoven for the aid with organization and human resources.

Part of the experiments described in this thesis were performed at Ghent University and I would like to express my gratitude once more to Roumen Petrov. I appreciated a lot all of our discussions during the PhD years, your lectures on EBSD, help with performing EBSD measurements and for being so friendly and approachable. I would like also to thank Vitaliy Bliznuk for the TEM analyses performed.

I would like to thank Thomas Davis, from Oxford University, Mercedes Hernandez Mayoral, from CIEMAT, and Ankit Kumar, from TU Delft/ASML, for our fruitful collaboration. Tom, thanks for the APT measurements, discussions and very nice reception in Oxford and, of course, for showing us where we can find the best falafel in the city! Mercedes, thank you so much for the TEM analyses and all our discussions. I am happy we can still collaborate and hope we can meet in person at some point. Ankit, I thank you a lot for the FIB preparation of APT samples, for our scientific discussions and, of course, for the friendship at TU Delft.

I would like also thank the Reactor Institute Delft and the amazing people I have met there: Catherine Pappas, Wim Bouwman and Lambert van Eijck; Martijn de Boer, Chris Duif and Juke Heringa, for being such great office companions; Anton Lefering, Evgenii Velichko and Steven Parnell for all the nice talks and coffee breaks at RID; Ilse van der Kraaij-Quick and Nicole Banga for all the help with administrative matters and always friendly attitude.

I would like to express great gratitude to the wonderful colleagues from the Materials Science and Engineering department. I have spent most of my time there and, oh, how good it was to meet and work with you all! Thank you so much dear Prisca Koelman, for all your help, since the beginning. From finding a Duwo apartment to all other administrative matters and for always receiving me (and the other students and employees) with a welcoming smile. Thanks to Maria Santofimia, Erik Offerman, Jan van Turnhout for all the discussions during meetings and conversations during coffee breaks/lunch. Sander van Asperen, thank you so much for all the help in the metallography lab, for breaking so many bakelites for me (hahahahaha!!) and for our talks about cats and heavy metal. Remko Seijffers, Elise Reinton, Agnieszka Kooijman, Ton Riemslog, Hans Brouwman, Hans Hofman, Nico Geerlofs, Ruud Hendrikx: thank you for the help with diverse experiments. A special thanks to Kees Kwakernaak for his infinite patience when I was learning how to operate the SEM and for always being helpful. Another special thanks to Richard Huizenga, for his help with Thermo-Calc, XRD and nice discussions.

I want to thank my dear dear friends from 3mE, with whom I had so many fun moments, during lunch, coffee breaks and going out in Delft and a special to this wonderful group: Sudhee, Alfonso, Javi, Chyrza, Casper, Wei, Carola, Bij-Na, Artemis, Vagelis, Tim, Marilia,

Behnam, Vitoria, Jithin, Daniel, Giovanni, Jhon, Li, Virginia. Thank you so much for everything! A special thanks to my dear friend Jia Fu, for being a great project companion, for working together, travelling and sharing life stories.

Now, a very special thanks to these three (in alphabetical order): Arthur, Konstantina and Martina. Life in The Netherlands would not be the same without you. In dutch there is the term *gezin*, which I translate as being the close family. You are my *gezin* here in The Netherlands. Thank you for everything!!

I am lucky enough, tough, to have another family here in The Netherlands, a Brazilian one: Maria, Thaine, Luquinhas, Cris, Camis, Alessandra. Thank you thank you thank you for always being supportive, for all the moments together. A very special thanks to Ana Clara, who was my first contact in Delft and who immediately became a best friend. Our friendship remains as strong as always, doesn't matter the country we are living in. Thank you for all the laughs, for your endless support!! Another very very special thanks to my dear Rania, whom I've met unexpectedly here in Delft and who immediately became a sister. Thank you so much for being part of my life, for your trust and love.

I am indeed very very lucky because I have also the most amazing friends in Brazil, friends that I know for 10+ years and that, despite the long distances, are so close to my heart: Beatriz, Ricardo, Guilherme, Giovanna, Rafael, Isaac, Renata, Leticia, Gustavo, Dielly, Cah, Lu, Fe, Erika, Samara, Bog. I am constantly grateful for having you in my life. Bia, thank you thank you thank you for the cover of my thesis. I couldn't have trusted it to anyone else.

Last, but definitely not least, I want to thank my parents, Isabel and Xerxes, I owe to you everything that I am today. Thank you for your endless love and support, and for growing with me during this life transition. My brothers, Alexandre and Leo, thank you for everything. My aunt Nadia, for her friendship and love, that I cherish so much. My grandma Lourdes, grandpa Nicola, grandma Nadima, uncles Artenes and Alberto, thank you. Obrigada familia querida. Sou eternamente grata por tudo!!

Alkmaar, 11<sup>th</sup> of April 2022.

## Curriculum Vitae

### Viviam Serra Marques Pereira

Born on the 23<sup>rd</sup> of January 1989, Sao Paulo, SP, Brazil

#### Education

**2009 – 2014:** Bachelor of Science in Materials Engineering (*Awarded:* 2014 CREA-SP Award of Professional Formation)

Universidade Federal do ABC (UFABC)

**2014 – 2017:** Master of Science in Metallurgical and Materials Science and Engineering

Universidade de Sao Paulo (USP)

**2017 – 2021:** PhD Materials Science and Engineering

Delft University of Technology

*Thesis:* ODS steels for nuclear applications - a study of the thermal stability of the microstructure and of the evolution of defects

#### Professional Experience

**2006 – 2008:** Chemistry technician (apprenticeship) in the Laboratory of Phase Transformations EPUSP, Sao Paulo, Brazil

**2013 – 2014:** Supply Chain Management Intern at Novelis, Santo Andre, Brazil

**2016 – 2017:** (Freelance) Technical Translator at S+F Editora, Sao Paulo, Brazil

**2017 – 2022:** PhD Researcher at DIFFER and TU Delft, The Netherlands

**2021 – Present:** Lead Materials Scientist at NRG, Petten, The Netherlands

## List of Publications

V.S.M. Pereira, T. P. Davis, M. H. Mayoral, A. Kumar, H. Schut, J. Sietsma. “Investigation of coarsening of oxide nanoparticles at 1400 K and its effect on the microstructure formation of an ODS Eurofer steel”. *Materials Characterization*, v. 185, 2022.

DOI: 10.1016/j.matchar.2022.111723

V.S.M. Pereira, S. Wang, T. Morgan, H. Schut, J. Sietsma. “Microstructural evolution and behaviour of deuterium in a ferritic ODS 12 Cr steel annealed at different temperatures”. *Metallurgical and Materials Transactions A*, v. 53, p. 874-892, 2022.

DOI: 10.1007/s11661-021-06559-0.

V.S.M. Pereira, H. Schut, J. Sietsma. “A study of the microstructural stability and defect evolution in an ODS Eurofer steel by means of Electron Microscopy and Positron Annihilation Spectroscopy”. *Journal of Nuclear Materials*, vol. 540, 2020.

DOI: 10.1016/j.jnucmat.2020.152398.

V.S.M. Pereira, D. Hincapie, L.P. Nishikawa, H. Goldenstein. “Effect of Microstructure on Hydrogen Diffusivity, Trapping and HIC Resistance in Two API X65 Steels”. *Conference paper OTC Brazil*, 2017.

DOI: 10.4043/28154-MS